Università degli Studi di Udine

Dottorato di Ricerca in
Scienze dell'Ingegneria Energetica e Ambientale
XXXI Ciclo - 2019

Dynamics of flexible fibers in turbulent channel flow

Dr. Diego Dotto

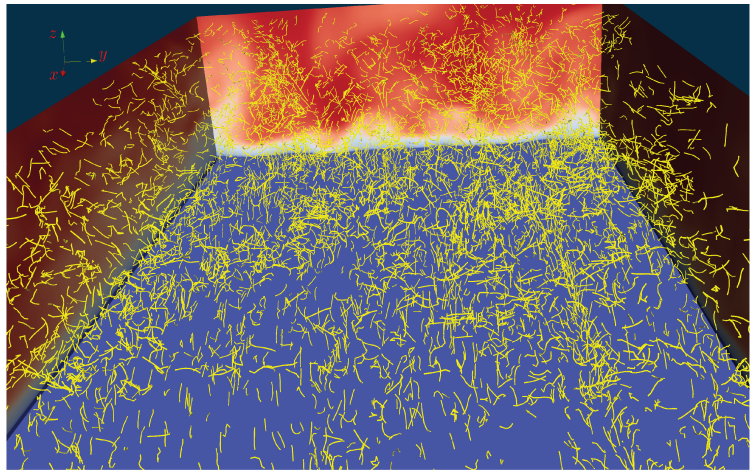

BOARD MEMBERS

Prof. Laurence BERGOUGNOUX	Reviewer
Prof. Srdjan SASIC	Reviewer
Prof. HELGE I. ANDERSSON	Committee member
Prof. MAURO DE MARCHIS	Committee member
Prof. ALFREDO SOLDATI	Committee member
Prof. Cristian MARCHIOLI	Supervisor
Prof. Alessandro TROVARELLI	Doctorate Chair

Author's e-mail:
dotto.diego@spes.uniud.it

Author's address:
Dipartimento Politecnico di Ingegneria e Architettura
Università degli Studi di Udine
Via delle Scienze, 206
33100 Udine – Italia
mobile: +39 347 0548612
office: +39 0432 558031
web: www2.diegm.uniud.it/diegm/

Cover picture:
DNS of turbulent channel flow laden with flexible fibers
(Ref. case: $St_r = 5$ and $\lambda_r = 5$).

Last update:
Udine, February 5, 2019

Ringraziamenti

Vorrei ringraziare le moltissime persone che mi sono state vicine e che mi hanno dato supporto nella realizzazione di questo lavoro: anche se alcune di esse non se ne sono rese conto, una mano me l'hanno data.
Ringrazio in particolar modo il prof. Cristian Marchioli ed il prof. Alfredo Soldati, per l'opportunità che mi hanno dato e per la disponibilità e pazienza nell'insegnarmi le cose: sarò loro grato per sempre.
Vorrei ringraziare inoltre il laboratorio di fluidodinamica: Francesco, Marina, Marco, Alessio, Giovanni, Harshit, Arash e Mobin per il continuo supporto e per le utili discussioni.
Ringrazio la mia famiglia: i miei genitori che con il loro amore e l'impegno quotidiano mi hanno sempre spronato ad andare avanti anche nei momenti di difficoltà. Un grazie a mio padre Livio e a mia madre Daniela per l'esempio di forza, di amore e di perseveranza; un grazie poi a mia sorella Valentina, che spero realizzi tutti i suoi sogni: questa tesi è dedicata a loro.
Volevo poi ringraziare poi nonno "Angin" e Tommaso, che anche se forse non se ne sono resi conto, mi hanno aiutato molto.
Un grazie a tutti gli amici e a tutte le amiche, soprattutto quelli che ho colpevolmente trascurato. Infine un pensiero a Riccardo che ci ha lasciati mentre scrivevo questa tesi: spero che possa trovare qualcuno con cui giocare anche adesso.

Abstract

In this thesis, we investigate the dynamics of dilute and semi-dilute suspensions of flexible fibers in turbulent channel flow. Fibers are longer than the Kolmogorov length scale of the carrier flow, and their velocity relative to the surrounding fluid is non negligible. Our first aim is to examine the effect of local shear and turbulence anisotropy on the translational and rotational behaviour of the fibers in a dilute regime, considering different elongation (parameterized by the aspect ratio, λ) and inertia (parameterized by the Stokes number, St). We use a Eulerian-Lagrangian approach based on direct numerical simulation of turbulence. Fibers are modelled as chains of sub-Kolmogorov rods (referred to as elements hereinafter) connected through ball-and-socket joints that enable bending and twisting under the action of the local fluid velocity gradients. Velocity, orientation and concentration statistics, extracted from simulations at shear Reynolds number $Re_\tau = 300$ (based on the channel height) are presented to give insights into the complex fiber-turbulence interactions that arise when non-sphericity and deformability add to inertial bias. These statistical observables are examined at varying aspect ratio (namely $\lambda_r = l_r/a = 2$ and 5, with l_r the length of each rod-like element r composing the fiber and a its cross-sectional diameter) and varying fiber inertia (considering values of the element Stokes number, $St_r = 1; 5; 30$). To highlight the effect of flexibility, statistics are compared with those obtained for fibers of equal mass that translate and rotate as rigid bodies relative to the surrounding fluid.
Flexible fibers exhibit a stronger tendency to accumulate in the very-near-wall region, where they appear to be trapped by the same inertia-driven mechanisms that govern preferential concentration of spherical particles and rigid fibers in bounded flows. In such region, bending of flexible fibers with small inertia (resp. large) inertia is enhanced (resp. reduced) by mean shear and turbulent Reynolds stresses. Preferential segregation into low-speed streaks and preferential orientation in the mean flow direction is also observed.

Another objective of the present work is to examine the behaviour of a semi-dilute suspension in the same flow configuration in order to highlight the effect of considering higher volume and mass fractions. To do so, we add a term in the Navier-Stokes equations, to represent the feedback force applied by the fibers on the surrounding fluid ($two-way$ coupling). The statistics examined refer to fluid velocity and its RMS are extracted from simulations at shear Reynolds number $Re_\tau = 300$ for fibers $\lambda_r = 2; 5$ and and $St_r = 30$. To highlight $two-way$ coupling effects, statistics are com-

pared with those obtained for fibers in the dilute regime.
The first and the second-order moments of the fluid velocity field are not modified substantially, whereas some quantitative change is observed in the statistics of wall-concentration and segregation: Fibers in the semi-dilute regime concentrate less in the near-wall region.
Some effect is observed also in the near-wall region, where bending of flexible fibers found to be slightly higher in the dilute regime. As could be expected, no significant $two - way$ coupling effect is observed in the center of the channel.

Contents

List of Figures

1

Introduction

"God could cause us considerable embarrassment by revealing all the secrets of nature to us: we should not know what to do for sheer apathy and boredom."

- Johann Wolfgang Goethe,

The motion of non-spherical particles in turbulent flow is a complex problem that has received a growing attention in the last decade. Complexity arises primarily from the multiscale nature of turbulence and from the coupling between the translational and rotational dynamics of the particles, which are governed by forces and torques that depend on particle shape and orientation (Voth and Soldati, 2017). The interest in tackling such a challenging problem comes from its many applications in both industry (e.g. pulp and and paper making (Dong et al. (2003); Lundell et al. (2011); Stockie and Green (1998)), post-combustion soot emission (Moffet and Prater, 2009), food or pharmaceutical processing (Boer et al., 2018)) and environment (e.g. atmospheric dispersion of pollen (Sabban and van Hout, 2011), plankton dynamics in water bodies Lillo et al. (2014); Lovecchio et al. (2017) or ice crystal formation in clouds (Gustavsson et al., 2017)).

From a numerical point of view, several models are available to describe translation and rotation of non-Brownian non-spherical particles in fluid flows (see Voth and Soldati (2017) for a review). The most natural approach to investigate particle-turbulence interaction at the particle scale relies on the Eulerian description of turbulence and on the Lagrangian description of particle trajectories (Toschi and Bodenschatz, 2009). Within this approach, the simplest model is based on the assumption that particles behave as perfect flow tracers: In this limit, namely when the particle Reynolds number is much smaller than unity (or equal to zero, ideally), exact equations for the time evolution of particle orientation are available for both axisymmetric (Jeffery, 1922) and non-axisymmetric particles (Hich and Leal, 1979). This approach has proven useful to study the motion of elongated micro-swimmers and non-motile plankton cells in turbulence

(Ardekani et al. (2017b); Lovecchio et al. (2017, 2013); Zhan et al. (2014)).

When the particle Reynolds number is small but the translational and rotational slip between the particle and fluid cannot be neglected, dynamical equations of rigid body motion can be used in which expressions for forces and torques acting on the particle are available for simple shapes, in particular, prolate and oblate spheroids, (Brenner and Cox (1963); Brenner (1964); Gallily and Cohen (1979); Voth and Soldati (2017)). This approach has been used to study the motion of rigid ellipsoids and disks in viscous and turbulent flow (Challabotla et al. (2015); Marchioli and Soldati (2013); Marchioli et al. (2010); Shams et al. (2001); Yuan et al. (2017); Zhao et al. (2017, 2013); Zhao and Wachem (2015)). If the particle Reynolds number becomes order unity or larger, then the combined effect of fluid and particle inertia should be taken into account (Lopez and Guazzelli, 2017). This effect has been examined for many different shapes in steady simple shear flow or isotropic turbulence (Byron et al. (2015); Lopez and Guazzelli (2017); Rosén et al. (2015); Subramanian and Koch (2005)) but remains largely unexplored in unsteady anisotropic flows. Empirical correlations are available, yet not applicable across the full range of spheroidal shapes (Voth and Soldati, 2017).

When particles have at least one dimension larger than the Kolmogorov scale but are not in the slender body limit, fully-resolved simulations have become feasible (see Maxey (2017) for a review) in view of the exponential increase of computational resources, which allows accurate tracking of the particles upon integration of fluid forces on the particle surface. As far as non-spherical particles in turbulence are concerned, however, studies based on fully-resolved simulations have focused primarily on spherical particles, with only few applications to elongated (and rigid) particles in channel flow: Do-Quang et al. (2014) simulated $\mathcal{O}(10^4)$ cylindrical fibers with size equivalent to a few grid cells up to 0.4% volume fraction; Ardekani et al. (2017a) performed DNS of suspensions of oblate spheroids using the Immersed Boundary Method; which was also employed by Eshghinejadfard et al. (2017) to examine spheroids with aspect ratio up to 4 and solid-phase volume fractions between 0.75% and 1.5%. These studies provide insights into the mechanisms that govern particle-induced turbulence modulation, revealing drag reduction in flows laden with oblate spheroids (Ardekani et al., 2017a) and drag increase in flows laden with prolate spheroids (Eshghinejadfard et al., 2017). A rather large body of literature is available for studies dealing with the analysis of fluid-structure interactions in the presence of flexible filaments (see Huang et al. (2007); Pei et al. (2018); Tang et al. (2018); Zhu and Peskin (2007) among others), but analysis of this problem is beyond the scope of the present thesis.

Most of the numerical studies in which the above-mentioned models have

been applied to non-spherical particles in turbulence focus on the case of rigid, non-deformable spheroids. The Jeffery equation (Jeffery, 1922), which describes exactly the periodical motion of an isolated prolate spheroid in simple shear flow, and its extensions to arbitrary flow fields (Brenner and Cox (1963); Brenner (1964) and to non-axisymmetric ellipsoids (Hich and Leal, 1979), have been the foundation to study the motion of rigid inertialess fibers. However, the Jeffery equations cannot be used to describe bending and twisting of long flexible fibers: Such fibers may execute a Jeffrey orbit in the initial stages of motion but this orbit is not stable one and will eventually drift through orbital constants (Joung et al., 2001). As far as inertial (rigid and elongated) particles in turbulence are concerned, their translational and rotational dynamics has been often investigated using a micro-hydrodynamic approach combining a large number of particles into a multi-rigid-body system. In this case, the physical problem investigated involved the dispersion of fibers and disks with length much smaller that the flow domain in fully-developed turbulence (Andrić et al., 2013). For such problem, the adoption of a micro-hydrodynamic approach based on accurate direct numerical simulation of the flow, combined with recent experimental measurements (Sabban et al., 2017), has led to a fairly good understanding of shape and size effects on macroscopic phenomena such as preferential concentration and wall accumulation in dilute suspensions (see Voth and Soldati (2017) for a review).

Besides particle shape and size, however, one additional feature that is relevant to applications and still to be grounded in fundamental physics is particle deformability, namely the tendency of very elongated (high aspect ratio) particles, referred to as fibers hereinafter, to flexure under the action of the underlying flow field. We can anticipate that the behaviour of the flexible fibers is different from the behaviour of an equivalent rigid fibers (where equivalent means that the rigid fiber has the same shape and mass of the fully streched flexible fiber). In fact if we consider the motion of a flexible fiber in a vortical flow field, and an equivalent rigid fiber with the center of mass in the same position as in Fig.[1.1]: We see that the rigid fiber samples just one value of fluid vorticity in its position, while the flexible fiber samples one value of fluid vorticity for each one of its elements (in Fig.[1.1] we use $\mathcal{N} = 7$ elements).

Flexible fibers are commonly found both in low-Reynolds-number flows for example polymers, proteins or other biological systems (López et al. (2015); Slowicka et al. (2015); Zhu and Peskin (2007)) and in high-Reynolds-number flows for example in the processing of fiber-reinforced composite materials (Zhang and Smith, 2016), in pulp and paper making (Lundell et al. (2011); Vakil and Green (2011)) or hydro-entanglement processes (Xiang and Kuznetsov, 2008). Clearly, these fibers introduce an additional geometrical complexity associated with their irregular shape, which has im-

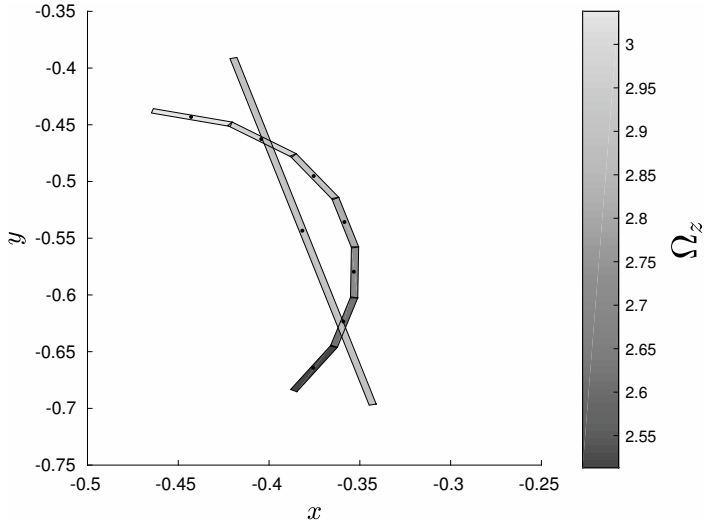

FIGURE 1.1 – Comparison between the vorticity applied on a rigid fiber and on an equivalent flexible fiber

portant consequences on the rheological properties and microstructure of the suspension (Wu and Aidun, 2010). While the interaction of flexible fibers with fluid flow at low Reynolds number has been examined in several theoretical and numerical works (Quennouz et al. (2015); Slowicka et al. (2015); SwitzerIII and Klingenberg (2003); Wang et al. (2006)), aimed at understanding buckling instabilities, topological changes in fiber shape and bending mode transition criteria; the effect of flexibility on turbulent suspensions at high Reynolds number has been poorly investigated. Recently, a series of experiments have been performed by Brouzet et al. (2014); Verhille and Bartoli (2016) to understand the importance of fiber deformation on its transport in homogeneous isotropic turbulence: In these experiments, fibers with length up to the integral time scale of the flow were considered and a critical length (the elastic length) was identified, above which flexibility cannot be neglected.

To the best of our knowledge, however, there are very few numerical simulations dealing with flexible fibers in a fully-developed, three-dimensional and time-dependent turbulent flow. Andrić et al. (2013) studied the translation and re-orientation of fibers in turbulent channel flow, and found that fibers exhibit complex geometrical configurations during their motion, similar to conformations of polymer strands subject to thermal fluctuations. More recently, Kunhappan et al. (2017) examined the motion of flexible fibers in bot homogeneous isotropic turbulence, considering flow conditions and fiber parameters similar to those of Verhille and Bartoli (2016), and channel

flow turbulence, considering a 1% concentration fiber suspension with fixed fiber-to-fluid density ratio. For the purposes of the present study, these works are of particular relevance, since we are interested in the dynamics of flexible fibers in wall-bounded turbulent flow. In particular, we focus on fibers. To study this problem, several micro-hydrodynamic approaches, which differ for the mathematical model employed to represent the fiber, have been proposed. The first model was put forth by (Yamamoto and Matsuoka, 1993): The fiber is modelled as a chain of spherical beads (hence the name bead-chain model) in which each bead obeys a kinematic constraint that prevents detachment of neighbouring beads while allowing for relative rotation. This model has been used recently by Delmotte et al. (2015) to study self-propelling filaments in viscous flow and by Sasayama and Inagaki (2017) to study fiber motion during processing of fiber-reinforce thermoplastics.

A modified version of the bead-chain model was later proposed by Ross and Klingenberg (1997), who used a chain of rigid ellipsoids, and by Schmid et al. (2000), who represented each element in the chain as a massless, rigid, cylindrical segment. This latter model was extended to inertial fibers by Lindström and Uesaka (2007), who derived an approximate model for the interaction between fiber elements and the surrounding fluid at finite element Reynolds number, and accounted for long-range hydrodynamic interactions between fibers. The model was used by the same authors to study paper forming (Lindström and Uesaka, 2008), and later by Martínez et al. (2017), to study clustering of long flexible fibers in 2D Arnold-Beltrami-Childress flow, and by Andrić et al. (2013, 2014) to study fiber-flow interactions and rheological properties of dilute suspensions in channel flow turbulence.

In the present thesis, we build on the work of Andrić et al. (2013) and of Kunhappan et al. (2017), and develop a comprehensive database of fiber trajectories, velocities and orientations to examine how flexibility adds to fiber elongation and inertia in determining fiber translation, rotation and spatial distribution within the flow. Compared to Andrić et al. (2013), we use Reynolds-number dependent expressions for the drag coefficient (instead of assuming it constant) and we consider much longer simulations (to reach a steady state for fiber concentration), higher fiber-to-fluid density ratios and a much higher number of fibers. In this way it was possible to obtain a statistical description of fibers interaction with wall-bounded turbulence. More specifically, the number of tracked fibers was selected in order to examine both a dilute suspension and a semi-dilute suspension. In the case of dilute flow, the fiber volume fraction is low enough to neglect the momentum exchange from the dispersed phase to the carrier fluid ($one-way$ coupling). In the case of a semi-dilute flow, the fiber volume fraction is such that the momentum exchange must be accounted for ($two-way$ coupling), even if the characteristic length scale of the dispersed phase is smaller than

the Kolmogorov dissipative scale.
In literature, for the spheres, a relation between the volume fraction and the flow regime is available for the case of spherical particles (Elgobashi, 2006; Balachandar and Eaton, 2010). A rather large body of literature is available for studies dealing with pointwise spheres in turbulent $two-way$ coupling regime. The main objective of these studies was to investigate the modulation of turbulence (drag reduction or increase) induced by the presence of the particles, and several methods have been proposed. Among others, the particle in cell (PIC) method developed by Crowe et al. (1977) and improved by Horwitz and Mani (2016) the hybrid direct numerical simulation (HDNS) approach by Ayala et al. (2007). More recently, alternative methods that account for momentum coupling irrespective of particle number density have been proposed: For instance, Pan and Banerjee (2001); Ireland and Desjardins (2017). Relevant to the present thesis is the exact regulareized by Gualtieri et al. (2014); Battista et al. (2018), which will be presented in detail in sec.[2.4], and applied for the first time on the motion of non-spherical (flexible) particles.
Much less work has been performed on semi-dilute suspensions of pointwise non-spherical particles in turbulence. To the best of our knowledge, there are just a few works dealing with two-way coupled rigid fibers (Zhao et al., 2013; Zhao and Wachem, 2015) and even less with two-way coupled flexible fibers (Lindström and Uesaka, 2008). The present work represents a first attempt to fill this gap in the literature.

Layout of the thesis

This thesis is organised as follows. In chap.[2], we present the physical problem and the approach to describe the simulations cumputed.
In chap.[3] we provide statistical characterization for the dynamics of a dilute suspension of fibers, comparing the motion of flexible fibers, with that of rigid fibers having the same physical properties and equivalent geometrical dimensions. We examine the translational, rotational and bending dynamics at varying fiber inertia and fiber elongation.
In chap.[4], we provide statistical observation for the dynamics of a semi-dilute suspension of fibers: in particular we focus on the effect of $two-way$ coupling on the main statistical observables of both the fluid and the fibers. Finally, we draw conclusions and outline future developments.

2

Methodology

"La filosofia é scritta in questo grandissimo libro che continuamente ci sta aperto innanzi a gli occhi (io dico l'universo), ma non si può intendere se prima non s'impara a intender la lingua, e conoscer i caratteri, ne' quali é scritto. Egli è scritto in lingua matematica, e i caratteri son triangoli, cerchi, ed altre figure geometriche, senza i quali mezi é impossibile a intenderne umanamente parola; senza questi é un aggirarsi vanamente per un oscuro laberinto."

- Galileo Galilei, *Il Saggiatore*

Part of the methodology described in this chapter has been accepted in the journal Acta Mechanica, under the title: *"Orientation, distribution and deformation of inertial flexible fibers in turbulent channel flow", (D.Dotto and C.Marchioli, 2019).*

The most precise and reliable methodology to study the behavior of a dilute or semi-dilute suspension particles in a turbulent flow field is the use of Direct Numerical Simulation (DNS) coupled with Lagrangian Particle Tracking (LPT). DNS means that the continuity equation (eq.[2.1]) and the Navier Stokes equations (eq.[2.2]) are solved without using any kind of turbulence model (as eddy viscosity, $k-\varepsilon$ or large-eddy ones) on a grid finer enough to capture all the detailed scales of the turbulence, from the integral ones down to the Kolmogorov micro-scale. This of course requires a big computational effort and in fact is only possible for very simple geometries and relatively moderate Reynolds numbers. LPT means that the dispersed phase is treated as an ensemble of real particles that posses inertia and that the trajectory of each particle is obtained by solving the governing equations of motion. In this chapter we will describe the reference geometry, the equations of motion for the continuous phase, their non-dimensional form in the physical space and their treatment in the spectral space; after we will state the description of the translational and rotational motion of

ellipsoidal particles and finally we will describe the methodology for the numerical resolution of the system of motion.

Fluid Flow Equations

The equations that fully describe the incompressible flow of a generic Newtonian fluid in which are dispersed a semi-diluted suspension of particle are the continuity equation (which expresses the mass conservation) and the Navier-Stokes equation (which expresses the momentum conservation). In dimensional form they are:

$$\nabla \cdot \mathbf{u} = 0 \tag{2.1}$$

$$\rho \left[\frac{\partial \mathbf{u}}{\partial t} + (\mathbf{u} \cdot \nabla)\, \mathbf{u} \right] = -\nabla P + \mu \nabla^2 \mathbf{u} + \mathbf{f}_{2w} \tag{2.2}$$

where $\mathbf{f}_{2w}$ is the drag force exerted by the particles on the surrounding fluid per unit of volume $[kg/(ms)^2]$, and the fluid parameters are ρ that represents the fluid density, μ that represents the fluid dynamic viscosity and P the equivalent pressure.

Non-dimensional Formulation

We will refer to the sketch reported in Fig.[2.1]: the channel we are interested in consists of two infinite parallel walls with non-slip conditions in which the flow is driven by a mean pressure gradient in the x-direction, $d\bar{P}/dx$; the computational domain it's supposed to be $L_z = 2h$ high , $L_x = 4\pi h$ long and $L_y = 2\pi h$ wide; the (x, y, z) frame represents streamwise, spanwise an wall-normal directions respectively, so that the flow is supposed periodic in the x and y directions.
To introduce the so called outer-scaling units (indicated by the "$^-$" apex) we need some characteristic flow scales: we will use the semi-height h as a characteristic length scale for the flow, while to get a typical speed we will again use the classical definition of shear velocity:

$$u_\tau = \sqrt{\frac{\tau_w}{\rho}} \tag{2.3}$$

where τ_w is the mean value of the shear at the wall; a very simple macroscopic force balance on the channel allows us to see that $\tau_w = h\frac{d\bar{P}}{dx}$, where $\frac{d\bar{P}}{dx}$ is the mean pressure gradient along x ($\bar{P} = \bar{P}(x)$ being the averaged value in the $y - z$ plane).
The shear velocity will thus result:

$$u_\tau = \sqrt{\frac{h}{\rho}\frac{d\bar{P}}{dx}} \tag{2.4}$$

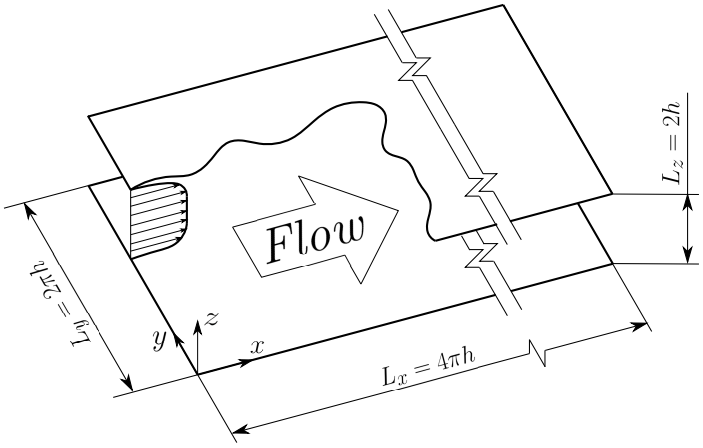

FIGURE 2.1 – Reference geometry for the channel flow DNS

It is now simple to see that the variables we are interested in can be put in non-dimensional form as follows:

$$\mathbf{x}^- = \frac{\mathbf{x}}{h}, \qquad \mathbf{u}^- = \frac{\mathbf{u}}{u_\tau}, \qquad t^- = \frac{tu_\tau}{h}, \qquad P^- = \frac{P}{\rho u_\tau^2} \qquad \mathbf{f}_{2w}^- = \mathbf{f}_{2w}\frac{h}{\rho u_\tau^2} \tag{2.5}$$

It is thus possible with some simple substitutions to obtain the following expressions for the continuity and Navier-Stokes equations:

$$\frac{\partial u_i^-}{\partial x_i^-} = 0. \tag{2.6}$$

$$\frac{\partial u_i^-}{\partial t^-} + u_j^-\frac{\partial u_i^-}{\partial x_j^-} = -\frac{\partial P^-}{\partial x_i^-} + \frac{1}{Re_\tau}\frac{\partial^2 u_i^-}{\partial x_j^- \partial x_j^-} + \mathbf{f}_{2w}^-. \tag{2.7}$$

where the shear Reynolds number Re_τ is defined as:

$$Re_\tau = \frac{\rho u_\tau h}{\mu} = \frac{u_\tau h}{\nu}, \tag{2.8}$$

in which $\nu[\frac{m}{s^2}]$ is the kinematic viscosity. If now we split the pressure gradient in mean ($\frac{d\bar{P}}{dx}$) and fluctuating ($\frac{\partial p^-}{\partial x_i^-}$) value, so that the real pressure is given by:

$$P^- = p^- + \frac{d\bar{P}}{dx}x,$$

we can obtain the following equation in which for sake of brevity the "-" notation is suppressed:

$$\frac{\partial u_i}{\partial t} = S_i + \frac{1}{Re_\tau}\frac{\partial^2 u_i}{\partial x_j \partial x_j} - \frac{\partial p}{\partial x_i}, \tag{2.9}$$

In the above equation the S_i source terms contain both the non-linear transport terms and the mean pressure gradient, imposed equal to -1 in outer-scaling units. Thus we have:

$$\begin{aligned} S_x &= -u_j \frac{\partial u_x}{\partial x_j} - 1 + f_{2w,x}, \\ S_y &= -u_j \frac{\partial u_y}{\partial x_j} + f_{2w,y}, \\ S_z &= -u_j \frac{\partial u_z}{\partial x_j} + f_{2w,z}, \end{aligned} \tag{2.10}$$

The derivation of the term $\mathbf{f}_{2w}$ will be provided in section [2.4].

Vorticity-Velocity Formulation

For the numerical resolution of the flow equations, it is very useful to rewrite the continuity and Navier-Stokes without taking explicitly into account the pressure $\frac{\partial p}{\partial x}$ gradient term By taking the curl of eq.[2.2] we can find:

$$\nabla \times \frac{\partial \mathbf{u}}{\partial t} = \nabla \times \mathbf{S} + \frac{1}{Re_\tau} \nabla \times \nabla^2 \mathbf{u} - \nabla \times \nabla p. \tag{2.11}$$

If we now observe that the last term is identically zero (because of a vectorial identity) and if we recall the definition of the vorticity vector $\boldsymbol{\omega} = \nabla \times \mathbf{u}$ (see appendix) it follows:

$$\frac{\partial \boldsymbol{\omega}}{\partial t} = \nabla \times \mathbf{S} + \frac{1}{Re_\tau} \nabla^2 \boldsymbol{\omega}, \tag{2.12}$$

which is an alternative expression of the vorticity transport equation. If we now take again the curl of this equation and we use the identity $\nabla \times \nabla \times \mathbf{c} = \nabla (\nabla \cdot \mathbf{c}) - \nabla^2 \mathbf{c}$ (which applies for every vectorial field $\mathbf{c}$) and the continuity equation, we can find the following Helmoltz fourth order equation:

$$\frac{\partial \left(\nabla^2 \mathbf{u} \right)}{\partial t} = \nabla^2 \mathbf{S} - \nabla \left(\nabla \cdot \mathbf{S} \right) + \frac{1}{Re_\tau} . \nabla^4 \mathbf{u} \tag{2.13}$$

The now classic resolution algorithm normal velocity-normal vorticity developed by Kim et al. (1987) requires to project the eq. [2.12] and [2.13] in the wall normal direction and solve them in order to obtain the wall normal components u_z and ω_z; the continuity equation and the definition of vorticity are then used to calculate the other two velocity components (u_x and u_y).
The system that is employed for the numerical resolution of the channel

flow is thus described by:

$$\begin{aligned}
\frac{\partial \omega_z}{\partial t} &= \frac{\partial S_y}{\partial x} - \frac{\partial S_x}{\partial y} + \frac{1}{Re_\tau}\nabla^2\omega_z \\
\frac{\partial \left(\nabla^2 u_z\right)}{\partial t} &= \nabla^2 S_z - \frac{\partial}{\partial x}\left(\frac{\partial S_j}{\partial x_j}\right) + \frac{1}{Re_\tau}\nabla^4 u_z \\
\frac{\partial u_x}{\partial x} + \frac{\partial u_y}{\partial y} &= -\frac{\partial u_z}{\partial z} \\
\frac{\partial u_y}{\partial x} + \frac{\partial u_x}{\partial y} &= \frac{\partial \omega_z}{\partial z}
\end{aligned} \tag{2.14}$$

Fluid Flow Equations in Spectral Space

Now it is illustrated a generic component of the velocity vector $\mathbf{u}(\mathbf{x}, t)$ case of homogeneous isotropic turbulence for a cubic box of size L in the discrete spectral space:

$$u_i(\mathbf{x}, t) = \sum_{n_x=-\frac{N}{2}+1}^{\frac{N}{2}} \sum_{n_y=-\frac{N}{2}+1}^{\frac{N}{2}} \sum_{n_y=-\frac{N}{2}+1}^{\frac{N}{2}} \hat{u}_i(\boldsymbol{\kappa}, t)\, e^{i\boldsymbol{\kappa}\cdot\mathbf{x}}, \tag{2.15}$$

in which $\kappa_i = \frac{2\pi n_i}{L}$ κ_i is the generic wavenumber, n_i is the n^{th} Fourier mode, is the total number of Fourier modes (and also grid nodes) used along each direction in order to represent the signal (in total we thus have N^3 nodes), $e^{i\boldsymbol{\kappa}\cdot\mathbf{x}}$ is the general Fourier mode and $\hat{u}_i(\boldsymbol{\kappa}, t)$ a generic Fourier coeffient for the velocity.

In the channel flow the presence of the non-slip walls rates high gradients in the wall normal z direction, making the homogeneous isotropic model un-suitable. Following Kim et al. (1987) it is however possible to treat the streamwise (x) and spanwise (y) directions as statistically homogeneous; if we also make the hypothesis that these directions are periodic of period L_x and L_y it will thus be possible to use the Fourier spectral representation at least along these two directions, by using N_x and N_y modes, that in physical space correspond to a uniform grid of spacing:

$$\begin{aligned}
\Delta x &= \frac{N_x}{L_x} \\
\Delta y &= \frac{N_y}{L_y}
\end{aligned} \tag{2.16}$$

While in the spectral space the corresponding wave numbers κ_x and κ_y apply:

$$\begin{aligned}
\kappa_x &= \frac{2\pi n_x}{L_x}, \\
\kappa_y &= \frac{2\pi n_y}{L_y},
\end{aligned} \tag{2.17}$$

doing so, the velocity signal will thus be expressed by:

$$u_i(\mathbf{x},t) = \sum_{n_x=-\frac{N}{2}+1}^{\frac{N}{2}} \sum_{n_y=-\frac{N}{2}+1}^{\frac{N}{2}} \sum_{n_y=-\frac{N}{2}+1}^{\frac{N}{2}} \hat{u}_i(\kappa_x,\kappa_y,z,t)\, e^{i(\kappa_x x+\kappa_y y)}, \quad (2.18)$$

where the dependence of the Fourier coefficient $\hat{u}_i$ on the inhomogeneous z coordinate is stressed; being z non homogeneous and non periodic it is in fact impossible to adopt the same strategy as for the other two coordinates. It is however possible to proceed in a quite analogous manner also along z adopting the Chebyshev polynomial representation instead of the Fourier one.

We have to use the following polynomials:

$$T_{n_z}(z) = \cos\left(n_z \cos^{-1}(z)\right), \quad (2.19)$$

where $z = z^- \in [-1;1]$ is a nondimensional variable and the grid points coordinates along z are given by:

$$z = \cos\left(\frac{n_z \pi}{N_z}\right), \quad (2.20)$$

where N_z is the total number of modes along z. An advantage of the Chebyshev representation is that it allows a great spatial resolution very close to the walls, which is necessary to properly describe the high gradients.

The generic velocity component will thus be expressed by the following Fourier-Chebyshev representation:

$$u_i(\mathbf{x},t) = \sum_{n_x=-\frac{N}{2}+1}^{\frac{N}{2}} \sum_{n_y=-\frac{N}{2}+1}^{\frac{N}{2}} \sum_{n_z=0}^{N_z} \hat{u}_i(\kappa_x,\kappa_y,n_z,t)\, T_{n_z}(z)\, e^{i(\kappa_x x+\kappa_y y)}. \quad (2.21)$$

Obviously such a reasoning applies not only for the velocity vector components but also for the vorticity or the pressure.
If we now apply the Fourier operator $F_{\boldsymbol{\kappa}}\{...\}$ to the eq.[2.14] previously stated in the physical space, we can carry the channel flow problem from physical to wavenumber space. We obviously must recall that only the x and y directions are Fourier-transformable and so we obtain:

$$F_{\boldsymbol{\kappa}}\left\{\frac{\partial u_i(\mathbf{x},t)}{\partial x_j}\right\} = i\kappa_j \hat{u}_i(\boldsymbol{\kappa},t) \quad (2.22)$$

applies only for $j = x, y$ but not for $j = z$.

Discretization of Fluid Flow Equations

The velocity equation is discretized as:

$$\begin{aligned}\frac{\partial}{\partial t}\left(\frac{\partial^2}{\partial z^2}-\kappa_{xy}^2\right)\hat{u}_z = &\left(\frac{\partial^2}{\partial z^2}-k_{xy}^2\right)\hat{S}_z + \\ &-\frac{\partial}{\partial z}\left(i\kappa_x\hat{S}_x + i\kappa_y\hat{S}_y + \frac{\partial \hat{S}_z}{\partial z}\right) + \\ &+\frac{1}{Re_\tau}\left(\frac{\partial^2}{\partial z^2}-\kappa_{xy}^2\right)\left(\frac{\partial^2}{\partial z^2}-\kappa_{xy}^2\right)\hat{u}_z\end{aligned} \tag{2.23}$$

where:
$\kappa_{xy}^2 = \kappa_x^2 + \kappa_y^2$.

The eq.[2.23] above it is discretized using an implicit-explicit scheme:

- Implicit Adam-Bashfort third order method for diffusive linear terms;
- Implicit Cranck-Nicholson method for the non-linear terms.

Considering the time steps $n-1$, n ed $n+1$ we obtain:

$$\begin{cases} n-1 & \Longrightarrow t-\Delta t, \\ n & \Longrightarrow t, \\ n+1 & \Longrightarrow t+\Delta t. \end{cases}$$

The eq.[2.23] above, become:

$$\begin{aligned}&\frac{1}{\Delta t}\left(\frac{\partial^2}{\partial z^2}-\kappa_{xy}^2\right)\left(\hat{u}_z^{n+1}-\hat{u}_z^n\right) = \frac{1}{2}\left(\frac{\partial^2}{\partial z^2}-\kappa_{xy}^2\right)\left(3\hat{S}_z^n-\hat{S}_z^{n-1}\right) + \\ &-\frac{3}{2}\frac{\partial}{\partial z}\left(i\kappa_x\hat{S}_x^n + i\kappa_y\hat{S}_y^n + \frac{\partial \hat{S}_z^n}{\partial z}\right) + \\ &+\frac{1}{2}\frac{\partial}{\partial z}\left(i\kappa_x\hat{S}_x^{n-1} + i\kappa_y\hat{S}_y^{n-1} + \frac{\partial \hat{S}_z^{n-1}}{\partial z}\right) + \\ &+\frac{1}{Re_\tau}\left(\frac{\partial^2}{\partial z^2}-\kappa_{xy}^2\right)\left(\frac{\partial^2}{\partial z^2}-\kappa_{xy}^2\right)\frac{\hat{u}_z^{n+1}+\hat{u}_z^n}{2},\end{aligned} \tag{2.24}$$

and defining:

$$\gamma = \frac{\Delta t}{2Re_\tau},$$

we obtain:

$$\begin{aligned}
&\left[1-\gamma\left(\frac{\partial^2}{\partial z^2}-\kappa_{xy}^2\right)\right]\left(\frac{\partial^2}{\partial z^2}-\kappa_{xy}^2\right)\hat{u}_z^{n+1}= \\
=&\frac{\Delta t}{2}\left(\frac{\partial^2}{\partial z^2}-k_{xy}^2\right)\left(3\hat{S}_z^n-\hat{S}_z^{n-1}\right)+ \\
-&\frac{3\Delta t}{2}\frac{\partial}{\partial z}\left(i\kappa_x\hat{S}_x^n+i\kappa_y\hat{S}_y^n+\frac{\partial\hat{S}_z^n}{\partial z}\right)+ \\
+&\frac{\Delta t}{2}\frac{\partial}{\partial z}\left(i\kappa_x\hat{S}_x^{n-1}+i\kappa_y\hat{S}_y^{n-1}+\frac{\partial\hat{S}_z^{n-1}}{\partial z}\right)+ \\
+&\left[\gamma\frac{\partial^2}{\partial z^2}+\left(1-\kappa_{xy}^2\right)\right]\left(\frac{\partial^2}{\partial z^2}-\kappa_{xy}^2\right)\hat{u}_z^n.
\end{aligned} \tag{2.25}$$

Considering the continuity equation:

$$i\kappa_x\hat{u}_x^n+i\kappa_y\hat{u}_y^n+\frac{\partial\hat{u}_z^n}{\partial z}=0 \quad\Longrightarrow\quad \frac{\partial\hat{u}_z^n}{\partial z}=-i\kappa_x\hat{u}_x^n-i\kappa_y\hat{u}_y^n, \tag{2.26}$$

and defining:

$$\Lambda^2=\frac{1+\gamma\kappa_{xy}^2}{\gamma},$$

we obtain:

$$\begin{aligned}
&-\gamma\left(\frac{\partial^2}{\partial z^2}-\lambda^2\right)\left(\frac{\partial^2}{\partial z^2}-\kappa_{xy}^2\right)\hat{u}_z^{n+1}= \\
&=-\kappa_{xy}^2\left(\frac{3}{2}\hat{S}_z^n-\frac{1}{2}\hat{S}_z^{n-1}\right)\Delta t-\kappa_{xy}^2\left[\gamma\frac{\partial^2}{\partial z^2}+\left(1-\gamma\kappa_{xy}^2\right)\right]\hat{u}_z^n+ \\
&-\frac{\partial}{\partial z}i\kappa_x\left(\frac{3}{2}\hat{S}_x^n-\frac{1}{2}\hat{S}_x^{n-1}\right)\Delta t-\frac{\partial}{\partial z}i\kappa_x\left[\gamma\frac{\partial^2}{\partial z^2}+\left(1-\gamma\kappa_{xy}^2\right)\right]\hat{u}_x^n+ \\
&-\frac{\partial}{\partial z}i\kappa_y\left(\frac{3}{2}\hat{S}_y^n-\frac{1}{2}\hat{S}_y^{n-1}\right)\Delta t-\frac{\partial}{\partial z}i\kappa_y\left[\gamma\frac{\partial^2}{\partial z^2}+\left(1-\gamma\kappa_{xy}^2\right)\right]\hat{u}_y^n.
\end{aligned} \tag{2.27}$$

Now we define the terms:

$$\hat{H}_x^n=\left(\frac{3}{2}\hat{S}_x^n-\frac{1}{2}\hat{S}_x^{n-1}\right)\Delta t+\left[\gamma\frac{\partial^2}{\partial z^2}+\left(1-\gamma\kappa_{xy}^2\right)\right]\hat{u}_x^n, \tag{2.28}$$

$$\hat{H}_y^n=\left(\frac{3}{2}\hat{S}_y^n-\frac{1}{2}\hat{S}_y^{n-1}\right)\Delta t+\left[\gamma\frac{\partial^2}{\partial z^2}+\left(1-\gamma\kappa_{xy}^2\right)\right]\hat{u}_y^n, \tag{2.29}$$

$$\hat{H}_z^n=\left(\frac{3}{2}\hat{S}_z^n-\frac{1}{2}\hat{S}_z^{n-1}\right)\Delta t+\left[\gamma\frac{\partial^2}{\partial z^2}+\left(1-\gamma\kappa_{xy}^2\right)\right]\hat{u}_z^n. \tag{2.30}$$

Applying the terms defined in the eq.[2.28]-[2.30] in the eq.[2.27]:

$$\left(\frac{\partial^2}{\partial z^2}-\Lambda^2\right)\left(\frac{\partial^2}{\partial z^2}-\kappa_{xy}^2\right)\hat{u}_z^{n+1} = \frac{1}{\gamma}\kappa_{xy}^2\hat{H}_z^n + \\ +\frac{1}{\gamma}\frac{\partial}{\partial z}\left(i\kappa_x\hat{H}_x^n + i\kappa_y\hat{H}_y^n\right), \tag{2.31}$$

and defining:

$$\hat{H}^n = \kappa_{xy}^2\hat{H}_z^n + \frac{\partial}{\partial z}\left(i\kappa_x\hat{H}_x^n + i\kappa_y\hat{H}_y^n\right), \tag{2.32}$$

we find the discretized equation for the velocity:

$$\left(\frac{\partial^2}{\partial z^2}-\Lambda^2\right)\left(\frac{\partial^2}{\partial z^2}-\kappa_{xy}^2\right)\hat{u}_z^{n+1} = \frac{\hat{H}^n}{\gamma}. \tag{2.33}$$

In order to solve this $4^{th}-$order eq.[2.33], we consider the following variable:

$$\hat{\theta} = \left(\frac{\partial^2}{\partial z^2}-\kappa_{xy}^2\right)\hat{u}_z^{n+1},$$

in this way we can obtain two $2^{nd}-$order equations:

$$\left(\frac{\partial^2}{\partial z^2}-\Lambda^2\right)\hat{\theta} = \frac{\hat{H}^n}{\gamma}, \tag{2.34}$$

$$\left(\frac{\partial^2}{\partial z^2}-\kappa_{xy}^2\right)\hat{u}_z^{n+1} = \hat{\theta}, \tag{2.35}$$

The eq.[2.35] is solved using the no-slip condition and the continuity equation at the wall:

$$\begin{cases} \hat{u}_z^{n+1}(\pm 1) = 0, \\ \dfrac{\partial \hat{u}_z^{n+1}}{\partial z}(\pm 1) = 0. \end{cases} \tag{2.36}$$

The solution to the eq.[2.36] requires the boundary condition on $\hat{\theta}$ that lacks on the physical model, so, in order to avoid this problem we define:

$$\hat{\theta} = \hat{\theta}_1 + \hat{A}\theta_2 + \hat{B}\theta_3, \tag{2.37}$$

where $\hat{A}, \hat{B} \in \Im$ are two constants.

The components $\hat{\theta}_1$, $\hat{\theta}_2$ and $\hat{\theta}_3$, are respectively the particolar solution and the homogeneous solutions to the eq.[2.34]. These solutions are obtained from:

$$\left(\frac{\partial^2}{\partial z^2}-\Lambda^2\right) = \hat{\theta}_1, \quad \hat{\theta}_1(1) = 0, \quad \hat{\theta}_1(-1) = 0, \tag{2.38}$$

$$\left(\frac{\partial^2}{\partial z^2} - \Lambda^2\right) = 0, \quad \theta_2(1) = 0, \quad \theta_2(-1) = 0, \tag{2.39}$$

$$\left(\frac{\partial^2}{\partial z^2} - \Lambda^2\right) = 0, \quad \theta_3(1) = 0, \quad \theta_3(-1) = 0. \tag{2.40}$$

Similarly:

$$\hat{u}_z^{n+1} = \hat{u}_{z,1} + \hat{A}u_{z,2} + \hat{B}u_{z,3}, \tag{2.41}$$

where $\hat{A}, \hat{B} \in \Im$ are two constants.

The components $\hat{u}_{z,1}$, $\hat{u}_{z,2}$ e $\hat{u}_{z,3}$, are respectively the particular solution and the homogeneous solutions to the eq.[2.35]. These solutions are obtained from:

$$\left(\frac{\partial^2}{\partial z^2} - \kappa_{xy}^2\right)\hat{u}_{z,1} = \hat{\theta}, \quad \hat{u}_{z,1}(1) = 0, \quad \hat{u}_{z,1}(-1) = 0, \tag{2.42}$$

$$\left(\frac{\partial^2}{\partial z^2} - \kappa_{xy}^2\right)u_{z,2} = 0, \quad u_{z,2}(1) = 0, \quad u_{z,2}(-1) = 0, \tag{2.43}$$

$$\left(\frac{\partial^2}{\partial z^2} - \kappa_{xy}^2\right)u_{z,3} = 0, \quad u_{z,3}(1) = 0, \quad u_{z,3}(-1) = 0. \tag{2.44}$$

The constants $\hat{A}$ and $\hat{B}$ are determinated using the condition:

$$\frac{\partial \hat{u}_z^{n+1}}{\partial z}(\pm 1) = 0 \quad \Longrightarrow \quad \begin{cases} \dfrac{\partial \hat{u}_{z,1}}{\partial z}(1) + \hat{A}\dfrac{\partial u_{z,2}}{\partial z}(1) + \hat{B}\dfrac{\partial u_{z,3}}{\partial z}(1), \\ \dfrac{\partial \hat{u}_{z,1}}{\partial z}(-1) + \hat{A}\dfrac{\partial u_{z,2}}{\partial z}(-1) + \hat{B}\dfrac{\partial u_{z,3}}{\partial z}(-1). \end{cases}$$

The solution of this equation [2.38]-[2.40] e [2.42]-[2.44] is obtained using Gauss elimination algorithm.

The vorticity equation for the component z in the pseudo-spectral space, become:

$$\left(\frac{\partial^2}{\partial z^2} - \Lambda^2\right)\hat{\omega}_z^{n+1} = -\frac{1}{\gamma}\left(i\kappa_x \hat{H}_y^n - i\kappa_y \hat{H}_x^n\right) \tag{2.45}$$

The solution of the equation [2.45] is obtained with the boundary conditions:

$$\hat{\omega}_z^{n+1}(\pm 1) = i\kappa_x \hat{u}_y^{n+1} - i\kappa_y \hat{u}_x^{n+1} \tag{2.46}$$

The solution to the equation [2.46] is obtained using Gauss elimination algorithm.

Once determined $\hat{u}_z^{n+1}$ and $\hat{\omega}_z^{n+1}$, it is possible to obtain the velocity components $\hat{u}_x^{n+1}$ e $\hat{u}_y^{n+1}$ from the discretization of the definitions of vorticity and continuity equations:

$$-i\kappa_y \hat{u}_x^{n+1} + i\kappa_x \hat{u}_y^{n+1} = \hat{\omega}_z^{n+1} \tag{2.47}$$

$$-i\kappa_x \hat{u}_x^{n+1} - i\kappa_y \hat{u}_y^{n+1} = \frac{\partial \hat{u}_z^{n+1}}{\partial z} \tag{2.48}$$

Equations of Motion for a Flexible Fiber

The model that we present starts from the formulation presented in (Lindström and Uesaka, 2007; Schmid et al., 2000). Each fiber is modeled as a chain of N rigid and inextensible elements (rods) of circular cross section, indexed $r \in [1, \mathcal{N}]$. Fiber elements have the same diameter and length, and are connected together through $\mathcal{N} - 1$ hinges, as shown in Fig.[2.2].

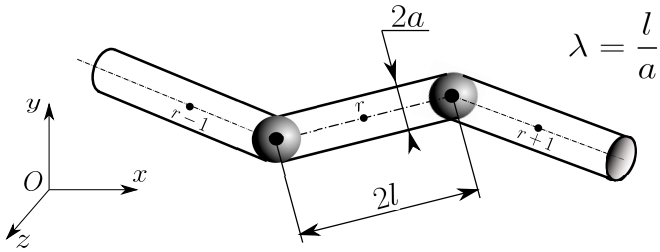

FIGURE 2.2 – Reference geometry for the flexible fiber

The location of each element is given with respect to a inertial frame of reference that uses a Cartesian coordinate system, with axes defined by the base vectors $\{\mathbf{e}_x, \mathbf{e}_y, \mathbf{e}_z\}$, and origin denoted by O. The interactions that are applied on a single cylinder can be divided in two groups: hydrodynamic interactions, as the drag force or the drag torque; and constraint interactions due to the inextensibility.

In the contest of not only low Reynolds number and inertial particle, the relation between stresses and velocities is not linear in general. In particular it means that it is necessary to write the hydrodynamic forces and torques for a wide range of Reynolds numbers, developping a method that in relation to this, uses the equation that fits best.

The constraint forces ensures that two adjacent cylinders can perform a relative rotation, that takes also into accont the resistence of the material to the bending force applied by the fluid.

Each fiber element is subject to hydrodynamic interactions, determined by the action of the drag force and torques, but also to interactions with its neighbours due to the connectivity constraint, which ensures that end-points of adjacent elements coincide: The resulting contact forces preserve the integrity of the fiber by allowing relative rotation of adjacent elements, yet not relative translation.

The motion of a generic element r (Lindström and Uesaka, 2007), (Schmid et al., 2000), with semi-length l, radius a (so the aspect ratio is $\lambda = l/a$) and density ρ_p, with velocity v_r, angular velocity $\boldsymbol{\omega}_r$, position $\mathbf{p}_r$ and orientation $\mathbf{o}_r$ is governed by the first and second Euler equations as shown in Fig.[2.3], Fig.[2.4] and the equation of the constraint as shown in Fig.[2.5]. Those equations are referred to an absolute frame of reference 0 and are related to a generic element r of the chain:

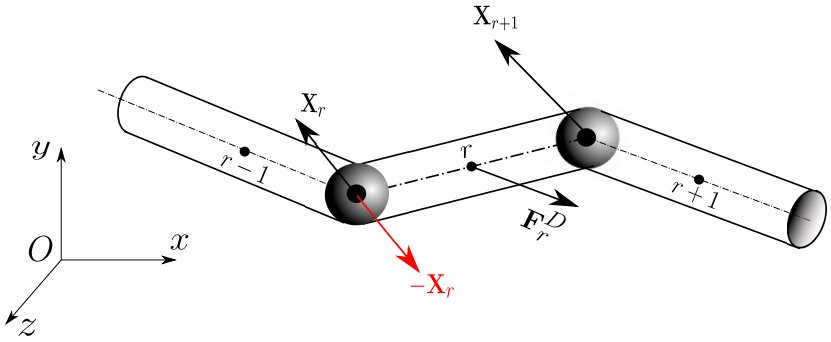

FIGURE 2.3 – Forces applied on the element r of the fiber.

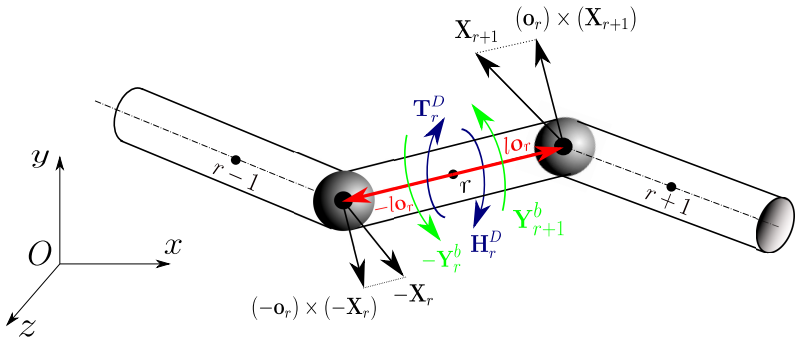

FIGURE 2.4 – Torques applied on the element r of the fiber.

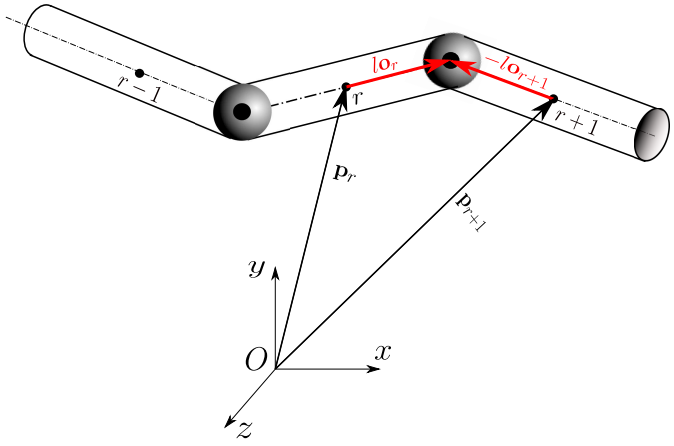

FIGURE 2.5 – Inextensibility cinematic constraint on the hinge between the elements r and $r+1$.

1^{st} *Euler's equation*

$$m_p \frac{d\mathbf{v}_r}{dt} = \mathbf{F}_r^D + (\mathbf{X}_{r+1} - \mathbf{X}_r) \tag{2.49}$$

2^{nd} *Euler's equation*

$$\begin{aligned} \frac{d\left(\bar{\bar{\mathbf{J}}}_r \boldsymbol{\omega}_r\right)}{dt} =& \mathbf{T}_r^D + \mathbf{H}_r^D + \left(\mathbf{Y}_{r+1}^b - \mathbf{Y}_r^b\right) + \\ &+ l_r \mathbf{o}_r \times (\mathbf{X}_{r+1} + \mathbf{X}_r) \end{aligned} \tag{2.50}$$

Constraint equation

$$\boldsymbol{\Psi}_r (\mathbf{p}_r, \mathbf{o}_r) = \mathbf{p}_r + l_r \mathbf{o}_r - (\mathbf{p}_{r+1} - l\mathbf{o}_{r+1}) = \mathbf{0} \tag{2.51}$$

Cinematic position equation

$$\frac{d\mathbf{p}_r}{dt} = \mathbf{v}_r \tag{2.52}$$

Cinematic orientation equation

$$\frac{d\mathbf{o}_r}{dt} = \boldsymbol{\omega}_r \times \mathbf{o}_r \tag{2.53}$$

For the eq.[2.49]:

$$\begin{cases} \mathbf{v}_r \implies \textit{Velocity of the center of mass of the } r^{th} \textit{ fiber element;} \\ m_p \implies \textit{Mass of the element } r\textit{;} \\ \mathbf{F}_r^D \implies \textit{Hydrodynamic Viscous Drag force anchting on the } r^{th} \\ \quad \textit{fiber element;} \\ \mathbf{X}_r \implies \textit{Constraint force exerted on the } (r-1)^{th} \textit{ fiber element} \\ \quad \textit{by the } r^{th} \textit{ fiber element, equal and opposite to the} \\ \quad \textit{costraint force that the } r^{th} \textit{ fiber element exerted on} \\ \quad \textit{the } (r-1)^{th} \textit{ fiber element;} \\ \mathbf{X}_{r+1} \implies \textit{Constraint force exerted on the } r^{th} \textit{ fiber element by} \\ \quad \textit{the } (r+1)^{th} \textit{ fiber element;} \end{cases}$$

For the eq.[2.50]:

$$\begin{cases} \boldsymbol{\omega}_r \implies \textit{Angular velocity of the center of mass of the } r^{th} \textit{ fiber element;} \\ \bar{\bar{\mathbf{J}}}_r \implies \textit{Inertia tensor in absolute frame of reference for the } r^{th} \textit{ fiber element;} \\ \mathbf{T}_r^D \implies \textit{Hydrodynamic drag torque due to the vorticity rate tensor acting on the } r^{th} \textit{ fiber element;} \\ \mathbf{H}_r^D \implies \textit{Hydrodynamic drag dorque due to the strain rate tensor acting on the } r^{th} \textit{ fiber element;} \\ \mathbf{Y}_r^b \implies \textit{Bending torque exerted by the } r^{th} \textit{ fiber element on the } (r-1)^{th} \textit{ fiber element, equal and opposite to the bending torque exerted by the } (r-1)^{th} \textit{ fiber element on the } r^{th} \textit{ fiber element;} \\ \mathbf{Y}_{r+1}^b \implies \textit{Bending torque exerted on the } (r+1)^{th} \textit{ fiber element by the } r^{th} \textit{ fiber element;} \\ \mathbf{o}_r \implies \textit{Orientation of the center of mass of the } r^{th} \textit{ fiber element;} \\ l\boldsymbol{o}_r \times \mathbf{X}_r \implies \textit{Constraint torque exerted by the } r^{th} \textit{ fiber element on the } (r-1)^{th} \textit{ fiber element, equal and opposite to the constraint torque exerted by the } (r-1)^{th} \textit{ fiber element on the } r^{th} \textit{ fiber element;} \\ l\boldsymbol{o}_r \times \mathbf{X}_{r+1} \implies \textit{Constraint torque exerted on the } (r+1)^{th} \textit{ fiber element by the } r^{th} \textit{ fiber element;} \\ \bar{\bar{\boldsymbol{\delta}}} \implies \textit{Identity matrix} \end{cases}$$

For the eq.[2.52]

$$\mathbf{p}_r \implies \textit{Position of the center of mass of the } r^{th} \textit{ fiber element;}.$$

The detailed derivation of the eq.[2.53] is given in the appendix (sec.[6.2]).

Since the equations are written for a single segment of the fiber r, also the Reynolds number are defined for a single segment $Re_{p;r}$ and not for the whole fiber:

$$Re_{p;r} = \frac{2\rho a}{\mu} \underbrace{\left| \left(\bar{\bar{\boldsymbol{\delta}}} - \mathbf{o}_r \mathbf{o}_r^T \right) (\mathbf{u}_r - \mathbf{v}_r) \right|}_{v_{\perp;r}}, \tag{2.54}$$

where $v_{\perp;r}$ is the modulus of the relative velocity orthogonal to the vector $\mathbf{o}_r$.
The an explanation of the eq.[2.54] is given in the appendix (sec.[6.5]).

Hydrodynamic viscous forces and torques (Stokes Limit)

If the Reynolds number for the fiber segment is low:

$$Re_{p;r} \simeq 0$$

We can consider the analytical solution given by the Stokes flow survey past an ellypsoidal particle and transponding it in the study of elements: an analytical solution, for the Hydrodynamic viscous drag force and torques exists for isolated spheroidal particles and laminar conditions (Kim and Karrila, 1991). According to the semi-empirical formula derived by (Cox, 1971), a prolate spheroid is hydrodynamically equivalent to a finite circular cylinder in the sense that their orbiting behavior in shear flow is the same if:

$$\frac{\lambda_{el}}{\lambda_r} = \frac{1.24}{\sqrt{\ln(\lambda_r)}} \tag{2.55}$$

where λ_{el} is the prolate spheroid equivalent aspect ratio.

Since a fiber segment r is a cylinder of diameter $2a$ and length $2l$ its aspect ratio is:

$$\lambda_r = \frac{2l_r}{2a}$$

The hydrodynamically equivalent prolate spheroid, whose minor semi-axes a_{el} and major semi-axis l_{el} equals a cylinder length $2l$, has:

$$\lambda_{el} = \frac{2l_{el}}{2a_{el}}$$

where a_{el} is the spheroid minor semi-axis.

From the formula derived by (Cox, 1971) it follows that a cylindrical fiber segment i is hydrodynamically equivalent to a prolate spheroid whose minor axis e_{el} Fig.[2.6]:
So:

$$a_{el} = \frac{a}{1.24}\sqrt{\ln(\lambda_r)} \tag{2.56}$$

The formula derived by Cox (1971) is valid for isolated particles and slender body approximation. None of these assumptions is true for fiber segments.

For a given velocity field $\mathbf{u}_r$ of the fluid, angular velocity field $\mathbf{\Omega}_r$ of the fluid, and gradient velocity field $\partial u_{i;r}/\partial x_j$ of the fluid, the viscous hydrodynamic viscous drag force $\mathbf{F}_r^D$, and torques $\mathbf{T}_r^D$, $\mathbf{H}_r^D$ are defined as Kim

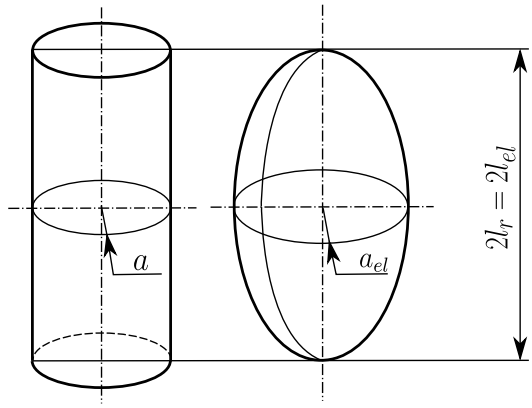

FIGURE 2.6 – Hydordinamic equivalence for $Re_{p;r} < 0.1$ between a cylinder and an ellipsoidal particle throught empirical formula of Cox (1971)

and Karrila (1991):

$$\mathbf{F}_r^D = \mathbf{F}_r^{D;*} = \underbrace{6\pi\lambda_r a\mu \left[X_r^A \bar{\bar{\boldsymbol{\delta}}} + \left(Y_r^A - X_r^A\right) \mathbf{o}_r \mathbf{o}_r^T\right]}_{\bar{\bar{\mathbf{A}}}_r^*} \left(\mathbf{u}_r - \mathbf{v}_r\right) \quad (2.57)$$

$$\mathbf{T}_r^D = \mathbf{T}_r^{D;*} = \underbrace{8\pi\lambda_r^3 a^3 \mu \left[X_r^C \bar{\bar{\boldsymbol{\delta}}} + \left(Y_r^C - X_r^C\right) \mathbf{o}_r \mathbf{o}_r^T\right]}_{\bar{\bar{\mathbf{C}}}_r^*} \left(\boldsymbol{\Omega}_r - \boldsymbol{\omega}_r\right) \quad (2.58)$$

$$\mathbf{H}_r^D = \mathbf{H}_r^{D;*} = -8\pi\lambda_r^3 a^3 \mu Y_r^H \left(\bar{\bar{\boldsymbol{\varepsilon}}} \mathbf{o}_r\right) : \left(\dot{\bar{\bar{\boldsymbol{\gamma}}}}_r \mathbf{o}_r\right) \quad (2.59)$$

where $\bar{\bar{\mathbf{A}}}_r^*$ is the resistence drag force tensor for $Re_{p;r} \simeq 0$; $\bar{\bar{\mathbf{C}}}_r^*$ is the resistence drag torque tensor for $Re_{p;r} \simeq 0$; and $\mathbf{H}_r^{D;*}$ is the resistence drag torque due to the gradient velocity flow field for $Re_{p;r} \simeq 0$.

The coefficient X_r^A, Y_r^A, X_r^C, Y_r^C and Y_r^H are derived from the parameter $e_{c,r}$:

$$e_{c,r} = \sqrt{\frac{\lambda_r^2 a^2 - a_{el}^2}{\lambda^2 a^2}} \quad (2.60)$$

So:

$$\begin{aligned}
X_r^A =& \frac{8e_{c;r}^3}{-6e_{c;r} + 3\left(1+e_{c,r}^2\right)\ln\left(\frac{1+e_{c,r}}{1-e_{c,r}}\right)} \\
Y_r^A =& \frac{16e_{c,r}^3}{6e_{c,r} + 3\left(3e_{c,r}^2-1\right)\ln\left(\frac{1+e_{c,r}}{1-e_{c,r}}\right)} \\
X_r^C =& \frac{4e_{c,r}^3\left(1-e_{c,r}^2\right)}{6e_{c,r} - 3\left(1-e_{c,r}^2\right)\ln\left(\frac{1+e_{c,r}}{1-e_{c,r}}\right)} \\
Y_r^C =& \frac{4e_{c,r}^3\left(2-e_{c,r}^2\right)}{-6e_{c,r} - 3\left(1+e_{c;r}^2\right)\ln\left(\frac{1+e_{c,r}}{1-e_{c;r}}\right)} \\
Y_r^H =& \frac{4e_{c;r}^5}{-6e_{c,r} + 3\left(1+e_{c,r}^2\right)\ln\left(\frac{1+e_{c,r}}{1-e_{c,r}}\right)}
\end{aligned} \tag{2.61}$$

In the eq. (2.59):

$$\left(\dddot{\bar{\varepsilon}}\mathbf{o}_r\right) : \left(\ddot{\bar{\gamma}}_r\mathbf{o}_r\right)\Big|_i = \varepsilon_{ijk}\left(\dot{\gamma}_{jl;r}o_{l;r}\right)o_{j;r}$$

$\ddot{\bar{\gamma}}_r$ is the gradient tensor:

$$\ddot{\bar{\gamma}}_r = \dot{\gamma}_{jl,r} = \frac{1}{2}\left(\frac{\partial u_{j,r}}{\partial x_l} + \frac{\partial u_{l,r}}{\partial x_j}\right)$$

And $\dddot{\bar{\varepsilon}}$ is the Levi-Civita 3 rank tensor :

$$\dddot{\bar{\varepsilon}} = \varepsilon_{ijk} = \begin{cases} 1 & if \quad i,j,k = 1,2,3; \quad i,j,k = 2,3,1; \quad i,j,k = 3,1,2 \\ -1 & if \quad i,j,k = 2,1,3; \quad i,j,k = 1,3,2; \quad i,j,k = 3,2,1 \\ 0 & if \quad i = j; \quad i = k; \quad j = k \end{cases}$$

Hydrodynamic viscous forces and torques for finite $Re_{p;r}$

If the Reynolds number of the fiber segment is:

$$Re_{p;r} > 0.$$

For a given velocity field $\mathbf{u}_r$ of the fluid, angular velocity field $\mathbf{\Omega}_r$ of the fluid, and gradient velocity field $\partial u_{i;r}/\partial x_j$ of the fluid, the viscous hydrodynamic

viscous drag force $\mathbf{F}_r^D$, and torques $\mathbf{T}_r^D$, $\mathbf{H}_r^D$ are:

$$\mathbf{F}_r^D = \mathbf{F}_r^{D;**} = \underbrace{2C_{D;r}\rho\lambda_r a^2 v_{\perp;r}\left(\bar{\bar{\boldsymbol{\delta}}} - \mathbf{o}_r\mathbf{o}_r^T\right)}_{\bar{\bar{\mathbf{A}}}_r^{**}}\left(\mathbf{u}_r - \mathbf{v}_r\right), \tag{2.62}$$

$$\mathbf{T}_r^D = \mathbf{T}_r^{D;**} = \underbrace{\frac{2}{3}C_{D;r}\rho\lambda_r^3 a^4 v_{\perp;r}\left(\bar{\bar{\boldsymbol{\delta}}} - \mathbf{o}_r\mathbf{o}_r^T\right)}_{\bar{\bar{\mathbf{C}}}_r^{**}}\left(\boldsymbol{\Omega}_r - \boldsymbol{\omega}_r\right), \tag{2.63}$$

$$\mathbf{H}_r^D = \mathbf{H}_r^{D;**} = -\frac{2}{3}C_{D;r}\rho\lambda_r^3 a^4 v_{\perp;r}\left(\bar{\bar{\boldsymbol{\varepsilon}}}\mathbf{o}_r\right) : \left(\dot{\bar{\bar{\boldsymbol{\gamma}}}}_r\mathbf{o}_r\right), \tag{2.64}$$

where $\bar{\bar{\mathbf{A}}}_r^{**}$ is the resistence drag force tensor for $Re_{p;r} > 0$; $\bar{\bar{\mathbf{C}}}_r^{**}$ is the resistence drag torque tensor for $Re_{p;r} > 0$; and $\mathbf{H}_r^{D;*}$ is the resistence drag torque due to the gradient velocity flow field for $Re_{p;r} > 0$. The detailed derivation of the equation for the torques $\mathbf{T}_r^D$, $\mathbf{H}_r^D$ is given in the sec.[6.6].

The drag coefficient $C_{D;r}$ that characterized the equations can be calculated as a function of the Reynolds number for the generic element r [2.54]:

$$C_{D;r} = f\left(Re_{p;r}\right)$$

It is possible to correlate drag coefficient $C_{D;r}$ with the Reynolds number for the fiber segment, using the equations provided by Clift et al. (1978), as shown in Fig.[2.7]:
The mathematical expression of the curve in the Fig.[2.7] above is:

$$C_{D;r} = \begin{cases} C_{D;r}^I & Re_{p;r} \in (0, 0.1], \\ C_{D;r}^I\left(1 + 0.147Re_{p;r}^{0.82}\right) & Re_{p;r} \in (0.1, 5], \\ C_{D;r}^I\left(1 + 0.227Re_{p;r}^{0.55}\right) & Re_{p;r} \in (5, 40], \\ C_{D;r}^I\left(1 + 0.0838Re_p^{0.82}\right) & Re_{p;r} \in (40, 400], \\ 1 & Re_{p;r} > 400, \end{cases} \tag{2.65}$$

where:

$$C_{D;r}^I = 9.689Re_{p;r}^{-0.78}.$$

Bending Stiffness

The torque acting on the $(r-1)^{th}$ fiber element, applied by the r^{th} fiber element, following Lindström and Uesaka (2007), is:

$$\mathbf{Y}_r^b = -k_b\alpha_r^b\mathbf{e}_r^b, \tag{2.66}$$

where, k_b is a Costant, due to the materials of the fiber:

$$k_b = \frac{E_Y\left(J + J\right)}{2l_r + 2l_r} = \frac{\pi E_y a^3}{8\lambda_r},$$

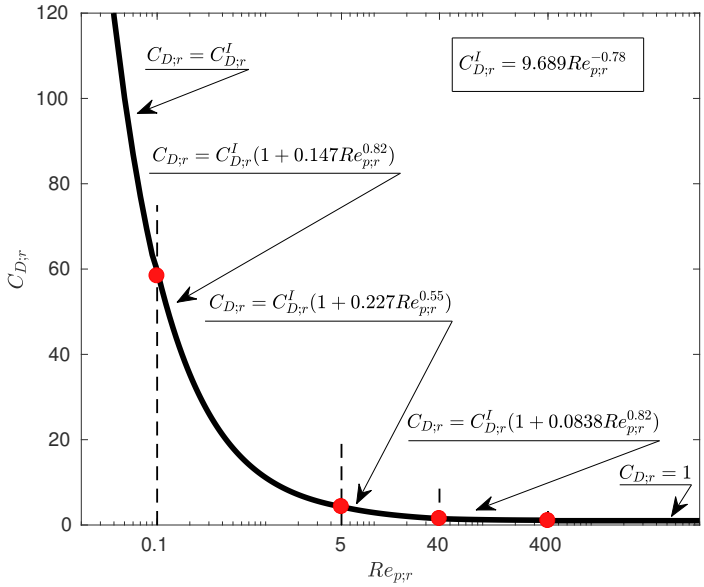

FIGURE 2.7 – Drag coefficient for a fiber element.

where, E_Y is the Young modulus, $l_r = 2\lambda_r a$, $J = \frac{1}{2}\pi a^4$ is the inertia tensor for a cylinder in a relative frame of reference, α^b_r is the solid angle (in radiant) between the $(r-1)^{th}$ fiber element (with orientation $\mathbf{o}_{r-1}$) and the r^{th} (with orientation $\mathbf{o}_r$):

$$\alpha^b_r = \cos^{-1}(\mathbf{o}_r \cdot \mathbf{o}_{r-1}) \quad \Longrightarrow \quad \begin{cases} \mathbf{o}_r \parallel \mathbf{o}_{r-1} & \Longrightarrow \quad \alpha^b_r = 0, \\ \mathbf{o}_r \perp \mathbf{o}_{r-1} & \Longrightarrow \quad \alpha^b_r = \frac{\pi}{2}. \end{cases}$$

While $\mathbf{e}^b_r$ is the versor othogonal to the versors $\mathbf{o}_{r-1}$ and $\mathbf{o}_r$:

$$\mathbf{e}^b_r = \frac{\mathbf{o}_r \times \mathbf{o}_{r-1}}{|\mathbf{o}_r \times \mathbf{o}_{r-1}|}.$$

So the bending can be expressed as:

$$\mathbf{Y}^b_r = -\frac{\pi E_Y a^3}{8\lambda_r} \cos^{-1}(\mathbf{o}_r \cdot \mathbf{o}_{r-1}) \frac{\mathbf{o}_r \times \mathbf{o}_{r-1}}{|\mathbf{o}_r \times \mathbf{o}_{r-1}|} \tag{2.67}$$

In this thesis we will a value of the Joung modulus $E_Y \neq 0$ only in the sec.[2.5].

Constraint Equation

The constraint equation, eq.[2.51] can be rewritten, following (Lindström and Uesaka, 2007), (Andrić et al., 2014), (Andrić et al., 2013) in order to

obtain an easier integration system:

$$\boldsymbol{\Psi}_r = \mathbf{0} \iff \begin{cases} \dfrac{d\boldsymbol{\Psi}_r}{dt} = \mathbf{v}_r - \mathbf{v}_{r+1} + \lambda_r a \left(\boldsymbol{\omega}_r \times \mathbf{o}_r + \boldsymbol{\omega}_{r+1} \times \mathbf{o}_{r+1}\right) = \mathbf{0} \\ \boldsymbol{\Psi}_r|_{t=0} = 0 \end{cases} \tag{2.68}$$

The equations that are involved in the problem for the generic segment r of the fiber are:

$$m_p \frac{d\mathbf{v}_r}{dt} = \bar{\bar{\mathbf{A}}}_r \left(\mathbf{u}_r - \mathbf{v}_r\right) + \mathbf{X}_{r+1} - \mathbf{X}_r \tag{2.69}$$

$$\begin{aligned} \dot{\bar{\bar{\mathbf{J}}}}_r \boldsymbol{\omega}_r + \bar{\bar{\mathbf{J}}}_r \frac{d\boldsymbol{\omega}_r}{dt} =& \bar{\bar{\mathbf{C}}}_r \left(\boldsymbol{\Omega}_r - \boldsymbol{\omega}_r\right) + \mathbf{H}_r + \\ &+ \frac{\pi E_Y a^3}{8\lambda_r} \left(\alpha_{r+1}^b \mathbf{e}_{r+1}^b - \alpha_r^b \mathbf{e}_r^b\right) + \\ &+ \lambda_r a \mathbf{o}_r \times \left(\mathbf{X}_{r+1} + \mathbf{X}_r\right) \end{aligned} \tag{2.70}$$

$$\mathbf{v}_r - \mathbf{v}_{r+1} + \lambda_r a \left(\boldsymbol{\omega}_r \times \mathbf{o}_r + \boldsymbol{\omega}_{r+1} \times \mathbf{o}_{r+1}\right) = \mathbf{0} \tag{2.71}$$

$$\frac{d\mathbf{p}_r}{dt} = \mathbf{v}_r \tag{2.72}$$

$$\frac{d\mathbf{o}_r}{dt} = \boldsymbol{\omega}_r \times \mathbf{o}_r \tag{2.73}$$

where:

$$m_p = 2\pi\rho_p \lambda_r a^3$$

$$\bar{\bar{\mathbf{A}}}_r = \begin{cases} \bar{\bar{\mathbf{A}}}_r^{\,*} = 6\pi\lambda_r a\mu \left[Y_r^A \bar{\bar{\boldsymbol{\delta}}} + \left(X_r^A - Y_r^A\right) \mathbf{o}_r \mathbf{o}_r^T\right] & if \quad Re_{p;r} \simeq 0 \\ \bar{\bar{\mathbf{A}}}_r^{\,**} = 2C_{D;r}\rho a^2 \lambda_r v_{\perp;r} \left(\bar{\bar{\boldsymbol{\delta}}} - \mathbf{o}_r \mathbf{o}_r\right) & if \quad Re_{p;r} > 0 \end{cases}$$

$$\bar{\bar{\mathbf{J}}}_r = \frac{1}{12} \underbrace{\left(2\pi\rho_p \lambda_r a^3\right)}_{m_p} a^2 \left[\left(4\lambda_r^2 + 3\right) \left(\bar{\bar{\boldsymbol{\delta}}} - \mathbf{o}_r \mathbf{o}_r^T\right) + 6\mathbf{o}_r \mathbf{o}_r^T\right]$$

$$\dot{\bar{\bar{\mathbf{J}}}}_r = \frac{1}{12} \underbrace{\left(2\pi\rho_p \lambda a^3\right)}_{m_p} a^2 \left(4\lambda_r^2 - 3\right) \left\{\left(\mathbf{o}_r \times \boldsymbol{\omega}_r\right) \mathbf{o}_r^T + \left[\left(\mathbf{o}_r \times \boldsymbol{\omega}_r\right) \mathbf{o}_r^T\right]^T\right\}$$

$$\bar{\bar{\mathbf{C}}}_r = \begin{cases} \bar{\bar{\mathbf{C}}}_r^{\,*} = 8\pi\lambda_r^3 a^3 \mu \left(Y^C \bar{\bar{\boldsymbol{\delta}}} + \left[X_r^C - Y_r^C\right) \mathbf{o}_r \mathbf{o}_r^T\right] & if \quad Re_{p;r} \simeq 0 \\ \bar{\bar{\mathbf{C}}}_r^{\,**} = \frac{2}{3} C_{D;r} \rho \lambda_r^3 a^4 v_{\perp;r} \left(\bar{\bar{\boldsymbol{\delta}}} - \mathbf{o}_r \mathbf{o}_r^T\right) & if \quad Re_{p;r} > 0 \end{cases}$$

$$\mathbf{H}_r = \begin{cases} \mathbf{H}_r^* = -8\pi\lambda_r^3 a^3 \mu Y_r^H \left(\bar{\bar{\boldsymbol{\varepsilon}}} \mathbf{o}_r\right) : \left(\dot{\bar{\bar{\boldsymbol{\gamma}}}}_r \mathbf{o}_r\right) & if \quad Re_{p;r} \simeq 0 \\ \mathbf{H}_r^{**} = -\frac{2}{3} C_{D;r} \rho \lambda_r^3 a^4 v_{\perp;r} \left(\bar{\bar{\boldsymbol{\varepsilon}}} \mathbf{o}_r\right) : \left(\dot{\bar{\bar{\boldsymbol{\gamma}}}}_r \mathbf{o}_r\right) & if \quad Re_{p;r} > 0 \end{cases}$$

The detailed derivation of the inertial tensor equation (in a relative frame of reference) is given in the appendix (sec.[6.3]).

Temporal discretization of fiber equations

The final system is:

$$\mathbf{v}_r^{n+1} = \mathbf{K}_r^n + \bar{\bar{\mathbf{Q}}}_r^n \left(\mathbf{X}_{r+1}^n - \mathbf{X}_r^n\right) \tag{2.74}$$

$$\boldsymbol{\omega}_r^{n+1} = \mathbf{R}_r^n + \bar{\bar{\mathbf{S}}}_r^n \bar{\bar{\mathbf{O}}}_r^n \left(\mathbf{X}_{r+1}^n + \mathbf{X}_r^n\right) \tag{2.75}$$

$$\mathbf{v}_r^{n+1} - \mathbf{v}_{r+1}^{n+1} + \lambda a \left(\boldsymbol{\omega}_r^{n+1} \times \mathbf{o}_r^n + \boldsymbol{\omega}_{r+1}^{n+1} \times \mathbf{o}_{r+1}^n\right) = \mathbf{0} \tag{2.76}$$

$$\mathbf{p}_r^{n+1} = \mathbf{p}_r^n + \Delta t \mathbf{v}_r^{n+1} \tag{2.77}$$

$$\mathbf{o}_r^{n+1} = \mathbf{o}_r^n + \frac{1}{6}\left[\mathbf{k}_{rk1;r}^n + 2\left(\mathbf{k}_{rk2;r}^n + \mathbf{k}_{rk3;r}^n\right) + \mathbf{k}_{rk4;r}^n\right] \tag{2.78}$$

where:

$$\bar{\bar{\mathbf{O}}}_r^n = \begin{bmatrix} 0 & -o_{z;r}^n & o_{y;r}^n \\ o_{z;r}^n & 0 & -o_{x;r}^n \\ -o_{y;r}^n & o_{x;r}^n & 0 \end{bmatrix} \quad \Longrightarrow \quad \mathbf{o}_r^n \times \mathbf{a} = \bar{\bar{\mathbf{O}}}_r^n \mathbf{a} \quad \forall \mathbf{a}$$

$$\mathbf{K}_r^n = \left(\bar{\bar{\boldsymbol{\delta}}} + \frac{\Delta t}{m_p} \bar{\bar{\mathbf{A}}}_r^n\right)^{-1} \left(\mathbf{v}_r^n + \frac{\Delta t}{m_p} \bar{\bar{\mathbf{A}}}_r^n \mathbf{u}_r^n\right)$$

$$\bar{\bar{\mathbf{Q}}}_r^n = \left(\bar{\bar{\boldsymbol{\delta}}} + \frac{\Delta t}{m_p} \bar{\bar{\mathbf{A}}}_r^n\right)^{-1}$$

$$\mathbf{R}_r^n = \left[\bar{\bar{\mathbf{J}}}_r^n + \Delta t \left(\dot{\bar{\bar{\mathbf{J}}}}_r^n + \bar{\bar{\mathbf{C}}}_r^n\right)\right]^{-1} \left[\bar{\bar{\mathbf{J}}}_r^n \boldsymbol{\omega}_r^n + \Delta t \left(\bar{\bar{\mathbf{C}}}_r^n \boldsymbol{\Omega}_r^n + \mathbf{H}_r^n + \mathbf{Y}_{r+1}^{b,n} - \mathbf{Y}_r^b\right)\right]$$

$$\bar{\bar{\mathbf{S}}}_r^n = \lambda a \left[\bar{\bar{\mathbf{J}}}_r^n + \Delta t \left(\dot{\bar{\bar{\mathbf{J}}}}_r^n + \bar{\bar{\mathbf{C}}}_r^n\right)\right]^{-1}$$

$$\mathbf{k}_{rk1;r}^n = -\Delta t \mathbf{o}_r^n \times \boldsymbol{\omega}_r^{n+1}$$

$$\mathbf{k}_{rk2;r}^n = -\Delta t \left(\mathbf{o}_r^n + \frac{1}{2}\mathbf{k}_{rk1;r}^n\right) \times \boldsymbol{\omega}_r^{n+1}$$

$$\mathbf{k}_{rk3;r}^n = -\Delta t \left(\mathbf{o}_r^n + \frac{1}{2}\mathbf{k}_{rk2;r}^n\right) \times \boldsymbol{\omega}_r^{n+1}$$

$$\mathbf{k}_{rk4;r}^n = -\Delta t \left(\mathbf{o}_r^n + \mathbf{k}_{rk3;r}^n\right) \times \boldsymbol{\omega}_r^{n+1}$$

$$\mathbf{Y}_r^{b,n} = \frac{\pi E_Y a^3}{8\lambda_r} \alpha_r^{b,n}$$

After some algrbra, the equation [2.76] became:

$$\bar{\bar{\mathbf{M}}}_{r+1}^n \mathbf{X}_{r+2}^n + \underbrace{\left(\bar{\bar{\mathbf{N}}}_{r+1}^n + \bar{\bar{\mathbf{N}}}_r^n\right)}_{\bar{\bar{\mathbf{N}}}_{r,r+1}^n} \mathbf{X}_{r+1}^n + \bar{\bar{\mathbf{M}}}_r^n \mathbf{X}_r^n = \mathbf{K}_r^{tot,n} \tag{2.79}$$

where:

$$\begin{aligned}
\mathbf{K}_{r+1}^{tot,n} &= -\mathbf{K}_{r+1}^{n} + \mathbf{K}_{r}^{n} - \lambda_r a \bar{\bar{\mathbf{O}}}_{r}^{n} \mathbf{R}_{r}^{n} - \lambda_r a \bar{\bar{\mathbf{O}}}_{r+1}^{n} \mathbf{R}_{r+1}^{n} \\
\bar{\bar{\mathbf{M}}}_{r+1}^{n} &= \bar{\bar{\mathbf{Q}}}_{r+1}^{n} + \lambda_r a \bar{\bar{\mathbf{O}}}_{r+1}^{n} \bar{\bar{\mathbf{S}}}_{r+1}^{n} \bar{\bar{\mathbf{O}}}_{r+1}^{n} \\
\bar{\bar{\mathbf{M}}}_{r}^{n} &= \bar{\bar{\mathbf{Q}}}_{r}^{n} + \lambda_r a^{+} \bar{\bar{\mathbf{O}}}_{r}^{n} \bar{\bar{\mathbf{S}}}_{r}^{n} \bar{\bar{\mathbf{O}}}_{r}^{n} \\
\bar{\bar{\mathbf{N}}}_{r+1}^{n} &= -\bar{\bar{\mathbf{Q}}}_{r+1}^{n} + \lambda_r a \bar{\bar{\mathbf{O}}}_{r+1}^{n} \bar{\bar{\mathbf{S}}}_{r+1}^{n} \bar{\bar{\mathbf{O}}}_{r+1}^{n} \\
\bar{\bar{\mathbf{N}}}_{r}^{n} &= -\bar{\bar{\mathbf{Q}}}_{r}^{n} + \lambda_r a \bar{\bar{\mathbf{O}}}_{r}^{n} \bar{\bar{\mathbf{S}}}_{r}^{n} \bar{\bar{\mathbf{O}}}_{r}^{n}
\end{aligned}$$

In particular the eq.[2.79], in the consideration of all the segments represents a tridiagonal block matrix system (see sec.[6.4]) that, in a compact form, is:

$$\bar{\bar{\boldsymbol{\mathcal{M}}}}^{n} \boldsymbol{\mathcal{X}}^{n} = \boldsymbol{\mathcal{K}}^{n} \tag{2.80}$$

where:

$$\bar{\bar{\boldsymbol{\mathcal{M}}}}^{n} = \begin{bmatrix}
\bar{\bar{\mathbf{N}}}_{1,2}^{n} & \bar{\bar{\mathbf{M}}}_{2}^{n} & \bar{\bar{\mathbf{0}}} & \dots & \bar{\bar{\mathbf{0}}} \\
\bar{\bar{\mathbf{M}}}_{2}^{n} & \bar{\bar{\mathbf{N}}}_{2,3}^{n} & \bar{\bar{\mathbf{M}}}_{3}^{n} & \bar{\bar{\mathbf{0}}} & \dots \\
\dots & \dots & \dots & \dots & \dots \\
\dots & \dots & \dots & \dots & \dots \\
\bar{\bar{\mathbf{0}}} & \dots & \bar{\bar{\mathbf{0}}} & \bar{\bar{\mathbf{M}}}_{\mathcal{N}}^{n} & \bar{\bar{\mathbf{N}}}_{\mathcal{N}-1,\mathcal{N}}^{n}
\end{bmatrix} \tag{2.81}$$

$$\boldsymbol{\mathcal{X}}^{n} = \begin{Bmatrix}
\mathbf{X}_{2}^{n+1} \\ \mathbf{X}_{3}^{n+1} \\ \dots \\ \mathbf{X}_{\mathcal{N}}^{n+1}
\end{Bmatrix} \tag{2.82}$$

$$\boldsymbol{\mathcal{K}}^{n} = \begin{Bmatrix}
\mathbf{K}_{1}^{tot,n} \\ \mathbf{K}_{2}^{tot,n} \\ \dots \\ \mathbf{K}_{\mathcal{N}-1}^{tot,n}
\end{Bmatrix} \tag{2.83}$$

The tridiagonal-block matrix in the eq.[2.81] can be rewritten in a compact form as:

$$\bar{\bar{\boldsymbol{\mathcal{M}}}}^{n} = \bar{\bar{\boldsymbol{\mathcal{L}}}}^{n} \bar{\bar{\boldsymbol{\mathcal{U}}}}^{n} \tag{2.84}$$

where:

$$\bar{\bar{\boldsymbol{\mathcal{L}}}}^{n} = \begin{bmatrix}
\bar{\bar{\mathbf{L}}}_{2}^{n} & \bar{\bar{\mathbf{0}}} & \bar{\bar{\mathbf{0}}} & \dots & \bar{\bar{\mathbf{0}}} \\
\bar{\bar{\mathbf{M}}}_{2}^{n} & \bar{\bar{\mathbf{L}}}_{2}^{n} & \bar{\bar{\mathbf{0}}} & \dots & \bar{\bar{\mathbf{0}}} \\
\dots & \dots & \dots & \dots & \dots \\
\dots & \dots & \dots & \dots & \dots \\
\bar{\bar{\mathbf{0}}} & \dots & \bar{\bar{\mathbf{0}}} & \bar{\bar{\mathbf{M}}}_{\mathcal{N}}^{n} & \bar{\bar{\mathbf{L}}}_{\mathcal{N}-1}^{n}
\end{bmatrix} \tag{2.85}$$

$$\bar{\bar{\boldsymbol{\mathcal{U}}}}^n = \begin{bmatrix} \bar{\bar{\boldsymbol{\delta}}} & \bar{\bar{\mathbf{U}}}_1^n & \bar{\bar{\mathbf{0}}} & \dots & \bar{\bar{\mathbf{0}}} \\ \dots & \dots & \dots & \dots & \dots \\ \dots & \dots & \dots & \dots & \dots \\ \bar{\bar{\mathbf{0}}} & \dots & \bar{\bar{\mathbf{0}}} & \bar{\bar{\boldsymbol{\delta}}} & \bar{\bar{\mathbf{U}}}_{\mathcal{N}-\infty}^n \\ \bar{\bar{\mathbf{0}}} & \dots & \bar{\bar{\mathbf{0}}} & \bar{\bar{\mathbf{0}}} & \bar{\bar{\boldsymbol{\delta}}} \end{bmatrix} \tag{2.86}$$

And:

$$\begin{aligned} \bar{\bar{\mathbf{L}}}_1^n &= \bar{\bar{\mathbf{N}}}_{1,2}^n \\ \bar{\bar{\mathbf{U}}}_1^n &= \left(\bar{\bar{\mathbf{N}}}_{1,2}^n\right)^{-1} \bar{\bar{\mathbf{M}}}_2^n \\ \bar{\bar{\mathbf{L}}}_r^n &= \bar{\bar{\mathbf{N}}}_{r,r-1}^n - \bar{\bar{\mathbf{M}}}_r^n \bar{\bar{\mathbf{U}}}_{r-1}^n \qquad if \quad r \in [2, \mathcal{N}-1] \\ \bar{\bar{\mathbf{U}}}_r^n &= \left(\bar{\bar{\mathbf{L}}}_r^n\right)^{-1} \bar{\bar{\mathbf{M}}}_{r+1}^n \qquad if \quad r \in [2, \mathcal{N}-1] \end{aligned} \tag{2.87}$$

The system [2.80] is equivalent to:

$$\bar{\bar{\boldsymbol{\mathcal{L}}}}^n \bar{\bar{\boldsymbol{\mathcal{U}}}}^n \boldsymbol{X}^{n+1} = \boldsymbol{K}^n \quad \Longleftrightarrow \quad \begin{cases} \bar{\bar{\boldsymbol{\mathcal{U}}}}^n \boldsymbol{X}^{n+1} = \boldsymbol{Y}^n \\ \bar{\bar{\boldsymbol{\mathcal{L}}}}^n \boldsymbol{Y}^n = \boldsymbol{K}^n \end{cases} \tag{2.88}$$

where:

$$\begin{aligned} \bar{\bar{\mathbf{Y}}}_1^n &= \left(\bar{\bar{\mathbf{L}}}_1^n\right)^{-1} \mathbf{K}_1^{tot,n} \\ \bar{\bar{\mathbf{Y}}}_r^n &= \left(\bar{\bar{\mathbf{L}}}_r^n\right)^{-1} \left(\mathbf{K}_r^{tot,n} - \bar{\bar{\mathbf{M}}}_r^n \mathbf{Y}_{r-1}^n\right) \qquad if \quad r \in [2, \mathcal{N}-1] \\ \bar{\bar{\mathbf{X}}}_{\mathcal{N}}^{n+1} &= \mathbf{Y}_{\mathcal{N}}^n \\ \bar{\bar{\mathbf{X}}}_r^{n+1} &= \mathbf{Y}_r^n - \bar{\bar{\mathbf{U}}}_r^n \mathbf{X}_{r+1}^n \qquad if \quad r \in [\mathcal{N}-1, 2] \end{aligned} \tag{2.89}$$

Fiber Equations in Non-Dimensional Form

The equation above are non-dimensionalized throught these terms:

$$u_\tau \left[\frac{m}{s}\right], \qquad \rho \left[\frac{kg}{m^3}\right], \qquad \nu \left[\frac{m^2}{s}\right]$$

So the terms involved in the system of equations [2.69]-[6.42], are re-written in non-dimensional form using the apex $^+$ (differently from the flow field with the apex $^-$), in this way:

$$\begin{aligned} &\mathbf{u}_r^+ = \frac{\mathbf{u}_r}{u_\tau} \quad \mathbf{v}_r^+ = \frac{\mathbf{v}_r}{u_\tau} \quad \boldsymbol{\omega}_r^+ = \frac{\boldsymbol{\omega}_r \mu}{\rho u_\tau^2} \quad t^+ = \frac{t u_\tau^2 \rho}{\mu} \\ &a^+ = \frac{a \rho u_\tau}{\mu} \quad \rho_p^+ = \frac{\rho_p}{\rho} \quad v_{\perp;r}^+ = \frac{v_{\perp;r}}{u_\tau} \quad \boldsymbol{\Omega}_r^+ = \frac{\boldsymbol{\Omega}_r \mu}{\rho u_\tau^2} \\ &E_Y = E_Y^+ u_\tau^2 \rho \quad \mathbf{X}_r^+ = \frac{\mathbf{X}_r \rho}{\mu^2}. \end{aligned}$$

The final system for the equations of motion in non-dimensional form and discretized in time, is shown in appendix (secs.[6.7],[6.8]).

Two-way Coupling

The role of the particles inside the flow field is linked directly to the feed-back effect or $two-way$ coupling. Here the particle suspension could be locally sufficiently dense so that the effect of the particles on the fluid phase is important: therefore force from the flow to the particle ats simultaneously back on the same fluid phase through Newton's third law, so we have a new term inside Navier-Stokes equation that will take in a account it.

Therefore, we could write the volume fraction of particles as:

$$\Phi_p = \frac{N_p V_p}{V}, \tag{2.90}$$

where N_p is the number of particles, V_p, is the volume of a single particle and V is the volume occupied by the fluid and by the particles. $Two-way$ coupling, for spheres, is based on the hypothesis that:

$$10^{-5} < \Phi_p < 10^{-2}$$

Implementation of two-way coupling

We can recall the eq.[2.2]:

$$\rho \left[\frac{\partial \mathbf{u}}{\partial t} + (\mathbf{u} \cdot \nabla)\, \mathbf{u} \right] = -\nabla P + \mu \nabla^2 \mathbf{u} + \mathbf{f}_{2w}.$$

The most straightforward method in order to compute the term $\mathbf{f}_{2w}$ is to consider it as the sum of the volume forces exerted by the single element on the fluid (Particle in cell method (Crowe et al., 1977)), that is given by:

$$\mathbf{f}_{2w} = \sum_{i_p=1}^{N_m} \sum_{r=1}^{\mathcal{N}} \mathbf{F}_{2w,r}^{i_p}, \tag{2.91}$$

where n_p is the number of particles constituting the whole set. The particular the contribute of the single element r of generic fiber i_p, $\mathbf{F}_{2w,r}^{i_p}$, is calculated from the force $\mathbf{F}_r^{D,i_p}$, defined in the eq.[2.57], [2.62], expressed in $[N]$, exerted by the fluid on the element r.

Since the feed-back force due to the 3^{rd} action-reaction Newton's law, we can write:

$$\mathbf{F}_{2w,r}^{i_p} = -\mathbf{F}_r^{D,i_p} \delta\left(\mathbf{x} - \mathbf{x}_r^{i_p}\right) \tag{2.92}$$

where $\delta\left(\mathbf{x}-\mathbf{x}_r^{i_p}\right)$ is the volumic Dirac function centered at the element location $\mathbf{x}_r^{i_p}$.

However, starting from this point, the force $\mathbf{f}_{2w}$ to be included in the Navier-Stokes eq.[2.2] can also be calculated through a more refined method than the one proposed above. In fact, following Gualtieri et al. (2014), the $two-way$ force can be redefined taking into account the time necessary for the momentum exerted on the particle to the surrounding fluid to be diffused, starting from the position of the particle, towards the closest nodes.

$$\mathbf{f}_{2w} = \sum_{i_p=1}^{N_m} \sum_{r=1}^{\mathcal{N}} \mathbf{F}_{2w,r}^{i_p}\left(t-\epsilon_R\right), \tag{2.93}$$

where $t-\epsilon_R$ is the time delay in which the force diffuses from the particle position to the neighbouring nodes. In particular ϵ_R is the regularization diffusion time scale, defined starting from the smallest lenght scale $\eta_K = \sqrt{2\nu\epsilon_R}$.
Also the feed-back force due to the 3^{rd} action-reaction Newton's law, should be re-written in order to take into account this time delay:

$$\mathbf{F}_{2w,r}^{i_p}(t-\epsilon_R) = -\mathbf{F}_r^{D,i_p}(t-\epsilon_R) g\left[\mathbf{x}-\mathbf{x}_r^{i_p}\left(t-\epsilon_R\right), \epsilon_R\right] \tag{2.94}$$

where $\mathbf{F}_r^{D,i_p}(t-\epsilon_R))$ is again the contribute of the single element r of generic fiber i_p defined in the eq.[2.62], [2.57], expressed in $[N]$, exerted by the fluid on the element r, but evaluated at the time $t-\epsilon_R$, and $g\left[\mathbf{x}, \mathbf{x}_r^{i_p}\left(t-\epsilon_R\right), \epsilon_R\right]$ is the solution of the diffusion equation.

$$g\left[\mathbf{x}-\mathbf{x}_r^{i_p}\left(t-\epsilon_R\right), \epsilon_R\right] = \frac{exp\left[-\frac{||\mathbf{x}-\mathbf{x}_r^{i_p}(t-\epsilon_R)||^2}{4\nu(t-\epsilon_R)}\right]}{\left[4\pi\nu\left(t-\epsilon_R\right)\right]^{3/2}}. \tag{2.95}$$

Eq.[2.93] should be non-dimensionalized with the "$^-$" units, while $F_{flu,r}^{i_p}$ is non-dimensionalized with the wall units "$^+$".
Then, we have to write, for each segment of each fiber (the definition of $\mathbf{F}_r^{D,i_p,+}$, is given in sec[6.7]):

$$\frac{d\mathbf{v}_r^{i_p,+}}{dt^+}|_{t^+-\varepsilon_R^+} = \mathbf{F}_r^{D,i_p,+}|_{t^+-\varepsilon_R^-} + \frac{1}{m_p^+}\left(\mathbf{X}_{r+1}^{i_p,+} - \mathbf{X}_r^{i_p,+}\right)|_{t^+-\varepsilon^-}, \tag{2.96}$$

where:

$$m_p = m_p^+ \rho\left(\frac{\nu}{u_\tau}\right)^3$$

The time go from t^+ to t^- with the follow equation:

$$t^- = \frac{t^+}{Re_\tau},$$

so we have:

$$\tilde{\mathbf{F}}_r^{D,i_p,+}|_{t^- - \varepsilon_R^-} = \frac{\mathbf{F}_r^{D,i_p}}{m_p}\left(\frac{\nu}{u_\tau^3}\right) = \frac{\mathbf{F}_r^{D,i_p,+}}{m_p^+}|_{t^- - \varepsilon_R^-}, \tag{2.97}$$

and:

$$\begin{aligned}\mathbf{F}_{2w,r}^{i_p,+}|_{t^- - \varepsilon^-} =& \mathbf{F}_{2w,r}^{i_p}\frac{1}{\rho\nu^2}|_{t-\varepsilon} = \\ =& -\mathbf{F}_r^{D,i_p}(t-\epsilon_R)g\left[\mathbf{x}-\mathbf{x}_r^{i_p}\left(t-\epsilon_R\right),\epsilon_R\right]\frac{1}{\rho\nu^2} = \\ =& -\frac{\mathbf{F}_r^{D,i_p,+}}{\rho\nu^2}(t^+-\epsilon_R^+)g^-\left[\mathbf{x}^- - \mathbf{x}_r^{i_p,-}\left(t^- - \epsilon_R^-\right),\epsilon_R^-\right],\end{aligned} \tag{2.98}$$

where:

$$g^-\left[\mathbf{x}^- - \mathbf{x}_r^{i_p,-}\left(t^- - \epsilon_R^-\right),\epsilon_R^-\right] = \frac{exp\left[-\frac{||\mathbf{x}^- - \mathbf{x}_r^{i_p,-}\left(t^- - \epsilon_R^-\right)||^2}{4Re_\tau\left(t^- - \epsilon_R^-\right)}\right]}{\left[4\pi h^3\left(t^- - \epsilon_R^-\right)\right]^{3/2}}. \tag{2.99}$$

Since the Navier-Stokes equations are written using the channel units $^-$, we have to trasform the drag force term $\mathbf{F}_{2w,r}^{i_p,+}$ in this non-dimensional formulation:

$$\begin{aligned}\mathbf{f}_{2w}^- =& \mathbf{f}_{2w}\left(\frac{h}{\rho u_\tau^2}\right) = \\ =& \left[\sum_{i_p=1}^{N_m}\sum_{r=1}^{\mathcal{N}}\mathbf{F}_{2w,r}^{D,i_p}(t-\epsilon_R)\right]\left(\frac{h}{\rho u_\tau^2}\right) = \\ =& -\left[\sum_{i_p=1}^{N_m}\sum_{r=1}^{\mathcal{N}}\tilde{\mathbf{F}}_r^{D,i_p,+}\left(t^- - \epsilon_R^-\right)g^-\left[\mathbf{x}^- - \mathbf{x}_r^{i_p,-}\left(t^- - \epsilon_R^-\right),\epsilon_R^-\right]\right]\frac{m_p^+}{Re_\tau^2}.\end{aligned} \tag{2.100}$$

From a mathematical point of view the constraint in the domain $\mathcal{D}^-$ is:

$$\int_{\mathcal{D}^-} g^-\left[\mathbf{x}^- - \mathbf{x}_r^{i_p,-}\left(t^- - \epsilon_R^-\right),\epsilon_R^-\right]d\mathbf{x}^- = 1. \tag{2.101}$$

From a numerical point of view the previous constraint become:

$$\int_{\mathcal{D}|_{Sp_{6\eta_K^-}^-}} g^-\left[\mathbf{x}^- - \mathbf{x}_r^{i_p,-}\left(t^- - \epsilon_R^-\right),\epsilon_R^-\right]d\mathbf{x}^- = 1, \tag{2.102}$$

where $Sp_{6\eta_K^-}^-$ is the spere centered in $\mathbf{x}_r^{i_p,-}$ and with a radius of $6\eta_K^-$.

Validation

To validate our code for the Lagrangian tracking we can consider the behaviour of a single flexible fiber in a simple shear layer flow, aligned with the moving walls (i.e. aligned with compressive axes of the ambient rate of strain), and compare our results with those obtained by Delmotte et al. (2015) with the gears model. First of all, it is necessary to define the bending ratio, BR, which is a dimentionless parameter and identifies the ratio between the bending stresses over the shear stress, as shown in Schmid et al. (2000); Forgacs and Mason (1959). The bending ratio is defined as:

$$BR = \frac{E_Y \left[\ln\left(2r_e\right) - 1.5\right]}{\mu\dot{\gamma} 2 \left(\mathcal{N}\lambda_r\right)^2} \tag{2.103}$$

where $\mathcal{N}\lambda_r$ is the aspect ratio of the fiber, $r_e = 1.24\left(\mathcal{N}\lambda_r\right)/\sqrt{\ln\left(\mathcal{N}\lambda_r\right)}$ calculated from Cox (1971) empirical formula is the equivalent ellipsoidal aspect ratio, and $\dot{\gamma}$ is the shear rate of the carring flow.
In order to be consistent with the result by Delmotte et al. (2015), we consider a flexible fiber with $Re_{p,r} \simeq 0$ (so forces and torques have the analytical solution proposed by Kim and Karrila (1991)) for each of the $\mathcal{N}$ elements, and we compare the results for $BR = 0.04$, as shown in Fig.[2.8]: The fiber

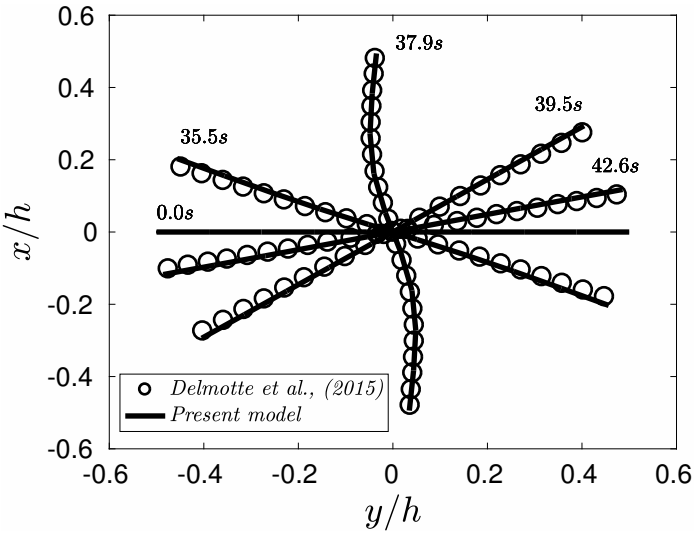

FIGURE 2.8 – Time deformation of a flexible fiber in a shear flow, the present model (straight lines) is compared with the gears model developped by Delmotte et al. (2015) (circles)

with the present model, in this results, is build up with $\mathcal{N} = 9$ elements with aspect ratio $\lambda_r = 1.4$.
In general if a fiber is fully stretched at rest, it will symmetrically deform

in a shear flow. If the fiber is initially aligned with the moving walls, it will deform assuming the "S-shape" observed in Fig.[2.8].
In particular from the Fig.[2.8] we see an excellent agreement between instantaneous position and deformation predicted by the present model and the result provided by the gears model of Delmotte et al. (2015).

3

Dilute Suspension of Flexible Fibers

"Tu prova ad avere un mondo nel cuore
E non riesci ad esprimerlo con le parole".

- Fabrizio De André, *Un matto*

Part of the results presented in this chapter, have been accepted in the journal Acta Mechanica, under the title: *"Orientation, distribution and deformation of inertial flexible fibers in turbulent channel flow", (D.Dotto and C.Marchioli, 2019).*
Other part of the results presented in this chapter, are under review, in the journal Meccanica (selected for special issue), under the title: *"Defomation dynamics of flexible fibers in turbulence", (D.Dotto and C.Marchioli, 2019).*

In this chapter, we characterize from a statistical point of view the behavior of a dilute suspension of fibers. We first provide a summary of the simulations, followed by a comprehensive statistical analysis of fiber translation, rotation and deformation dynamics under the $one-way$ coupling regime.

Summary of Simulations

In this first part of the thesis we consider the motion of a dilute suspension of flexible fibers in turbulence (i.e. $\mathbf{f}_{2w} = 0$ and contacts among the fibers are not considered). Moreover the following results are related to simulations in which there is no bending stiffness between two neighbouring elements (i.e. $E_Y = 0$) and the fibers' rebound on the wall is fully elastic (see sec.[6.1]). The same time step size as that of the fluid is used for integration, and the total Lagrangian tracking time in wall units is $t^+ = t\nu/u_\tau^2 = 1250$, which was enough to reach the steady state in fiber wall-normal concentration.

Simulations are carried out at friction Reynolds number $Re_\tau = u_\tau h/\nu_f = 150$, where $u_\tau = 0.1177m/s$ is the friction velocity based on the mean wall shear stress and on fluid density, $\nu = 1.57 \cdot 10^{-5} m^2/s$ is fluid viscosity and $h = 0.02m$ is the channel half height. The corresponding bulk Reynolds number is $Re = u_b h/\nu \simeq 2250$, where $u_b = 1.77m/s$ is the bulk velocity. The Reynolds number based on the hydraulic diameter is $Re_D \simeq 9000$. The size of the computational domain is $1885 \times 942 \times 300$ wall units in x, y and z, discretized with $128 \times 128 \times 129$ grid nodes. The non-dimensional step for time integration is 0.003 in wall units.
The relevant parameters for time integration are a, λ_r and the response time of the fiber element (Shapiro and Goldenberg, 1993):

$$\tau_{p,r} = \frac{2a^2 \lambda_r \rho_p^+}{9\nu} \frac{\ln\left(\lambda_r + \sqrt{\lambda_r^2 - 1}\right)}{\sqrt{\lambda_r^2 - 1}} \tag{3.1}$$

In this study, we have selected the following dimensionless values: $a^+ = 0.17$ (corresponding to $a \simeq 22.7\mu m$ in dimensional units), $\lambda_r = 2, 5$, and $St_r = \tau_p/\tau_f = 1, 5, 30$ with $\tau_f = \nu/u_\tau^2$. For this choice of values, fiber specific density is varied in the range $102.4 < \rho_p^+ < 3071.8$ for $\lambda_r = 2$ and $66.55 < \rho_p^+ < 1996.5$ for $\lambda_r = 5$. The corresponding Stokes numbers for a fully stretched fiber (namely for a rigid fiber with equal density and total length $L_f = 2\mathcal{N} l_r$ are: $St_f = 2.2, 11.0$ and 64.9 for $\lambda_r = 2$, and $St_f = 1.8, 9.1$ and 54.5 for $\lambda_r = 5$, respectively. To ensure converged statistics, swarms of $N_m = 10^5$ fibers, each having $\mathcal{N} = 7$ elements (as in Andrić et al. (2013)), are tracked for each combination of values in the (λ_r, St_r) space, assuming one-way coupling between the phases. The corresponding volume fractions are $\Phi_V \simeq 0.8 \cdot 10^{-4}$ for $\lambda_r = 2$, and $\Phi_V \simeq 2.0 \cdot 10^{-4}$ for $\lambda_r = 5$, whereas the percent mass fractions are in the range $0.6 < \Phi_M^{\%} < 19.2$ for $\lambda_r = 2$ and $1.0 < \Phi_M^{\%} < 31.1$ for $\lambda_r = 5$. The parameters are summarized in Tab.[3.1].
The time step used, ensures that during the simulation is respected, for every fiber, the following constraint:

$$||p_r + a^+ l_r \mathbf{o}_r - p_{r+1} + a^+ l_{r+1} \mathbf{o}_{r+1}|| \leq \frac{2l_r}{100}$$

In order to be within the limits of the model, individual fiber elements are smaller (or not longer, at least) than the smallest flow scale; however the entire fiber is longer regardless of λ_r. In the present flow configuration, the Kolmogorov length scale has a mean value $\eta_{K,avg}^+ \simeq 2$, and varies from $\eta_{K,min}^+ \simeq 1.62$ at the wall to $\eta_{K,max}^+ \simeq 3.61$ at the channel center (Picciotto et al., 2005). The semi-length of a fiber element is $l_r^+ \simeq 0.34$ for $\lambda_r = 2$ and $l_r^+ \simeq 0.84$ for $\lambda_r = 5$, corresponding to a total length of a fully stretched fiber $L_f^+ \simeq 4.7$ (equivalent to $L_f \simeq 634.9\mu m$ in dimensional units) for $\lambda_r = 2$ and $L_f^+ \simeq 11.8$ (equivalent to $L_f \simeq 1587.3\mu m$ in dimensional units)

for $\lambda_r = 5$. The corresponding ratio of fiber length to channel half height is $L_f/h \simeq 0.032$ and $L_f/h \simeq 0.079$, which is higher than those considered by Andrić et al. (2013) ($0.013 < L_f/h < 0.03$). Fiber elements will thus experience slightly different local flow conditions (velocity fluctuations and gradients) with respect to their neighbours (Ravnik et al., 2018): Our model can take these differences into account, and can reproduce their effect on the overall translational and rotational dynamics of the fiber. By doing so, we expect to observe a different long-term behaviour in fiber dispersion compared to the case of rigid fibers, which evolve only according to the flow conditions at the position of the fiber center of mass.

St_r	λ_r	a^+	ρ_p^+	L_f^+	St_f	Φ_V	$\Phi_M^{\%}$
1	2	0.17	102.4	4.7	2.2	$0.8 \cdot 10^{-4}$	0.6
1	5	0.17	66.55	11.8	1.8	$2.0 \cdot 10^{-4}$	1.0
5	2	0.17	512.0	4.7	11.0	$0.8 \cdot 10^{-4}$	3.2
5	5	0.17	322.8	11.8	9.1	$2.0 \cdot 10^{-4}$	5.2
30	2	0.17	3071.8	4.7	64.9	$0.8 \cdot 10^{-4}$	19.2
30	5	0.17	1996.5	11.8	54.5	$2.0 \cdot 10^{-4}$	31.1

TABLE 3.1 – Summary of the parameters in the simulations

Results and Discussion

In this section, we provide a statistical characterization of fiber translational and rotational dynamics inside the channel. Fig.[3.1] provides a qualitative visualization of the instantaneous distribution of the $St_r = 5$ fibers in a fluid slab of size $698 < x^+ < 1306$, $297 < y^+ < 705$, $0 < z^+ < 150$. The non-homogeneous distribution attained by the fibers, which are released in a fully-stretched configuration (all fiber elements are aligned) at random position and with random orientation, is evident and is biased by fiber inertia. Our aim is to quantify the effect of flexibility on the macroscopic processes that stem from such distribution, namely preferential concentration and near-wall segregation (Martínez et al., 2017). To this aim, several statistical observables discussed in this section provide direct comparison against the case of rigid fibers with equal shape and mass. Note that, in the present simulations, a rigid fiber is fully equivalent to a flexible fiber when the latter is completely stretched.

Velocity Statistics

The mean streamwise velocity, $\langle v_{x,G} \rangle$ (lines), of the different fiber sets is shown in Fig.[3.2], together with the mean streamwise velocity, $\langle u_{x,G} \rangle$ (symbols), of the fluid seen at the fiber's center of mass G. These profiles were

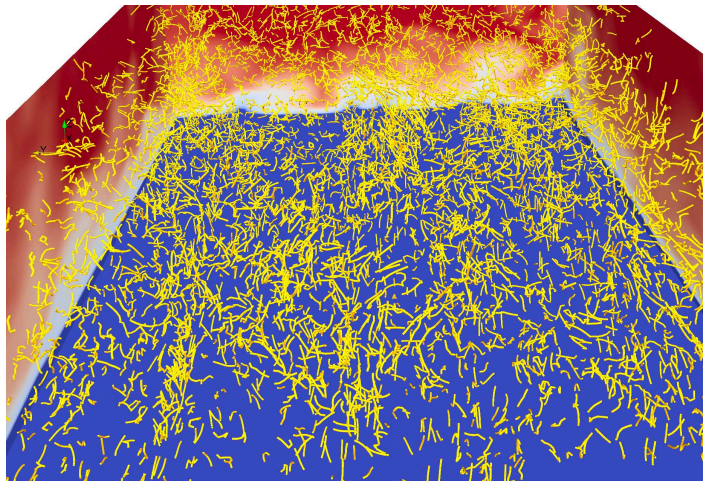

FIGURE 3.1 – Instantaneous distribution of $St_r = 5$ fibers in turbulent channel flow. For visualization purposes, only fibers in the slab $698 < x^+ < 1306$, $297 < y^+ < 705$, $0 < z^+ < 150$ are shown. Colormaps at the sides of the slab show the streamwise fluid velocity distribution (red: higher-than-mean velocity, blue:lower-than-mean velocity

obtained by computing the instantaneous values of v_x and u_x at the center of each fiber element (this implies interpolation for u_x) and then by averaging: Over all elements of one fiber, over all fibers located at the same wall-normal distance, and Over time.
The resulting mean quantity is represented by angular brackets, $\langle \dots \rangle$, hereinafter. Values for velocities are expressed in wall units, but the superscript $^+$ has been dropped for ease of notation. We remark that, different from a rigid fiber, the position of the center of mass of a deformed fiber does not necessarily coincide with the position of center point of the fiber's middle element. Each panel in Fig.[3.2] refers to a different Stokes number, and compares the velocity profiles for different aspect ratios. The horizontal axis starts at $z^+ = 1$ because the number of fibers comprised between the wall and this location is too low to ensure convergence of the statistics. It is apparent that fibers with small inertia ($St_r = 1$, panel (a)) move at the same mean velocity of the surrounding fluid, lagging slightly the Eulerian fluid velocity in the buffer layer. As fiber inertia and elongation increase, $\langle v_{x,G} \rangle$ starts to deviate from $\langle u_{x,G} \rangle$ especially in the near-wall region where fibers appear to lead the fluid proportionally to their length. The extent of this region widens as the fiber Stokes number is increased, reaching out in the buffer region for the $St_r = 30$ fibers (Fig.[3.2](c)). Here, the tendency of fibers to lag behind the fluid and sample regions of the flow characterized by local fluid velocity lower than the mean is enhanced by inertia. These observations are in agreement with previous studies in which rigid fibers were considered (Marchioli et al., 2010), suggesting a negligible effect of

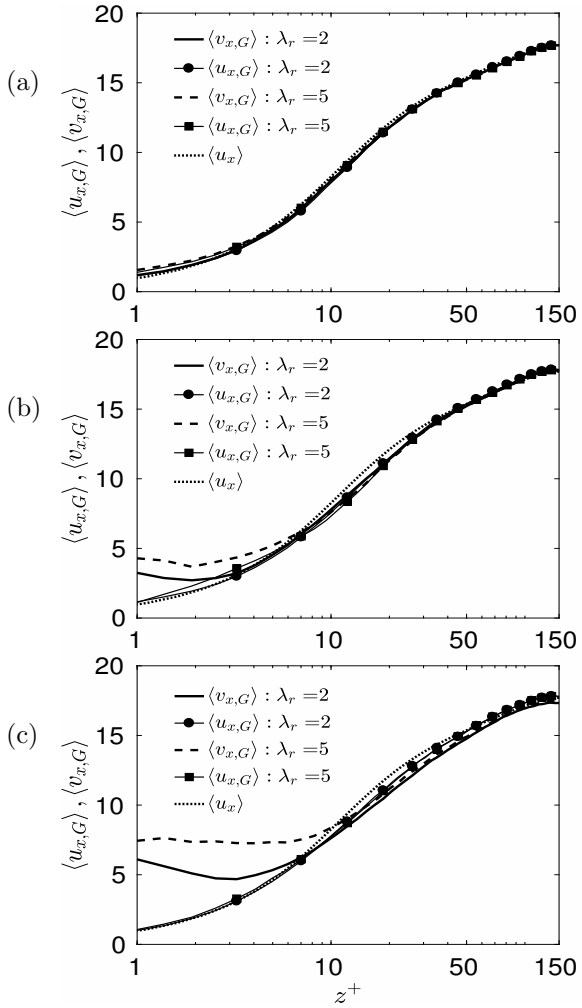

FIGURE 3.2 – Fiber mean streamwise velocity, $\langle v_{x,G}\rangle$. Subscript G indicates that the velocity at the fiber's center of mass G is considered. For comparison purposes, also the mean fluid velocity seen by the fibers is shown. Panels: (a) $St_r = 1$; (b) $St_r = 5$; (c) $St_r = 30$. Symbols represent fluid velocity interpolated at point G, solid and dashed lines represent fiber velocity, dotted lines represent the Eulerian fluid velocity.

deformability on the capability of fibers to maintain their streamwise momentum while drifting to the wall due to turbophoresis. The difference between $\langle v_{x,G}\rangle$ and $\langle u_{x,G}\rangle$ indicates that a relative velocity between each fiber element and the local fluid is established.

The resulting Reynolds number, $Re_{p,r}$, computed using eq.[2.54], is shown in Fig.[3.3] as function of the wall-normal distance. The values attained by $Re_{p,r}$ determine the specific expression used to compute the drag coef-

ficient $C_{D,r}$ according to eq.[2.65]. As expected, $Re_{p,r}$ increases as fibers

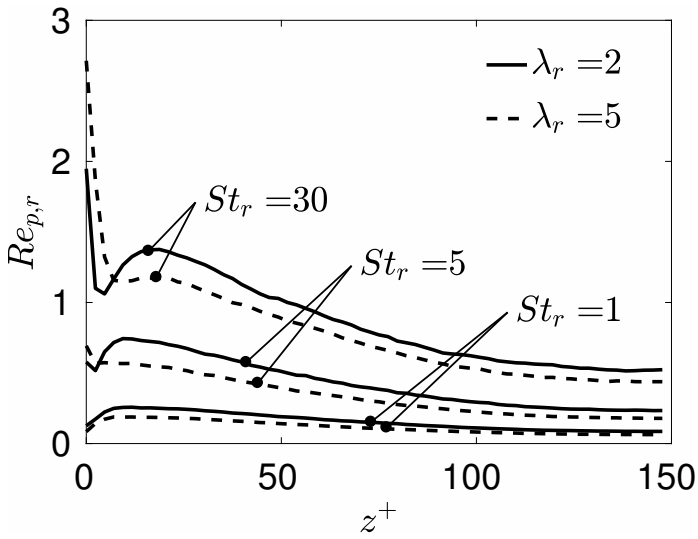

FIGURE 3.3 – Fiber element's mean Reynolds number, $Re_{p,r}$. Solid lines: $\lambda_r = 2$; dashed lines: $\lambda_r = 5$.

approach the wall, and is larger for higher-inertia fibers. A maximum is reached around the location of maximum fiber-to-fluid relative velocity, but values remain always smaller than unity. Interestingly, $Re_{p,r}$ is larger for flexible fibers with lower aspect ratio (except for the $St_r = 30$ fibers inside a thin near-wall region). This is due to the fact that fibers with $\lambda_r = 2$ are characterized by higher density with respect to $\lambda_r = 5$ fibers (this is needed to keep the values of St_r and a^+ fixed) and, in turn, by higher mass and higher value of St_f: Therefore, shorter fibers are expected to exhibit a larger relative velocity difference with respect to longer fibers in our simulations.

Because fibers are anisotropic in shape, their rotational dynamics are also important to understand their interaction with the flow. In Fig.[3.4], we show the spanwise component of the mean angular velocity, $\langle\omega_{y,G}\rangle$, for the different fiber sets. This observable quantifies the ability of the fiber to perform tumbling-like rotations in the longitudinal $x - z$ plane. The mean vorticity of the fluid "seen", $\langle\Omega_{y,G}\rangle$, and the mean Eulerian fluid vorticity, $\langle\Omega_y\rangle$, are also shown: These profiles are obtained using the same computation as in Fig.[3.2]. The streamwise and wall-normal components are not shown since their average value in the wall-normal direction is always equal to zero. Lines and symbols are as in Fig.[3.2]. Different from the translational velocities, the fiber angular velocity (lines) exhibits significant deviations from the vorticity of the fluid "seen" (symbols) for all St_r: Fibers

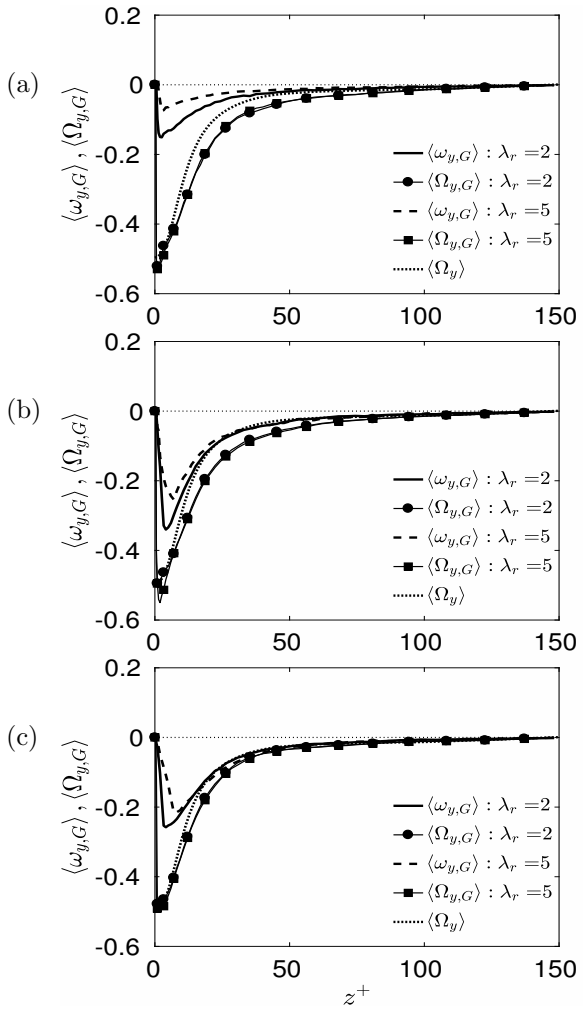

FIGURE 3.4 – Fiber mean spanwise angular velocity, $\langle\omega_{y,G}\rangle$. Subscript G indicates that only the velocity at the fiber's center of mass G is considered. Panels: (a) $St_r = 1$; (b) $St_r = 5$; (c) $St_r = 30$. Lines and symbols are as in Fig.[3.2]

always lag the fluid and rotate at a slower rate, especially when characterized by small inertia. Note that the fibers sample fluid regions characterized by vorticity larger than the Eulerian one. We also observe that the behaviour of $\langle\omega_{y,G}\rangle$ is dependent on the aspect ratio (namely on the rotational inertia of the fiber), which has no effect on $\langle\Omega_{y,G}\rangle$: Shorter fibers tend to rotate faster than longer ones, this tendency being more evident for small fiber inertia. As discussed in Marchioli et al. (2016), the rotational inertia of an elongated particle can be parameterized by a Stokes number $St_{rot,\perp}$, referred to the minor symmetry axes of the fiber, which quantifies the inertial

response of the fiber to tumbling; and a Stokes number $St_{rot,\parallel}$, referred to the major symmetry axis of the fiber, which quantifies the inertial response of the fiber to drilling. It can be shown that both $St_{rot,\perp}$ increases with aspect ratio, whereas $St_{rot,\parallel}$ decreases. This implies that, in our simulation setting, fibers with higher aspect ratio exhibit higher rotational inertia with respect to tumbling, thus explaining the trends shown in Fig.[3.4].

Orientation Statistics

The orientation of the fibers within the flow provides useful information about their preferential alignment. In Fig.[3.5], we shown the probability density function (PDF) of the fiber mean orientation in the streamwise and wall-normal directions, indicated as $\langle o_{x,G} \rangle$ and $\langle o_{x,G} \rangle$ respectively.
All fiber sets are considered, and $PDFs$ are conditioned to the location of the fiber in the wall-normal direction: Lines refer to $PDFs$ computed considering only fibers in a near-wall region of thickness equal to $5\delta_{VS}$, with δ_{VS} the viscous sublayer thickness (equal to 6 wall units in the present simulations); symbols refer to $PDFs$ computed considering only fibers in the bulk of the flow (namely, fibers located at distances larger than $5\delta_{VS}$ from the wall). The thin solid line in each panel represents the PDF corresponding to a random distribution of fiber orientations in a three-dimensional domain. We remind that the component o_x (resp. o_z) of the orientation vector is equal to the absolute value of the cosine of the angle between the major axis of the fiber element and the streamwise (resp. wall-normal) coordinate of the Cartesian frame of reference. Therefore, $o_j = 1$ (resp. $o_j = 0$) means that the fiber is aligned with (resp. orthogonal to) the j^{th} flow direction. Because we are examining flexible fibers, an orientation can be computed for each element of the fiber. The profiles shown in Fig.[3.5] were obtained upon averaging o_x and o_z over all elements of each flexible fiber; and then averaging the resulting values over all fibers pertaining to the same near-wall or bulk-flow fluid slab.

For the case of fibers with low inertia ($St_r = 1$, panels (a) and (b) in Fig.[3.5]) a significant difference can be observed between the near-wall PDF and the bulk-flow PDF for both aspect ratios examined. The near-wall PDF is negatively-skewed (resp. positively-skewed) for $\langle o_{x,G} \rangle$ (resp. $\langle o_{z,G} \rangle$), indicating that $St_r = 1$ fibers are preferentially aligned with the streamwise flow direction, and perpendicular to mean shear. This trend is more evident for the longer fibers (compare dashed and solid lines). The bulk-flow PDF is more symmetric and relatively insensitive to the aspect ratio. This finding is in agreement with the fact that turbulence in the central region of the channel is more homogeneous and isotropic and, hence, is expected to induce little or no preferential orientation. The symmetry of the bulk-flow PDF is maintained also at higher Stokes numbers, even

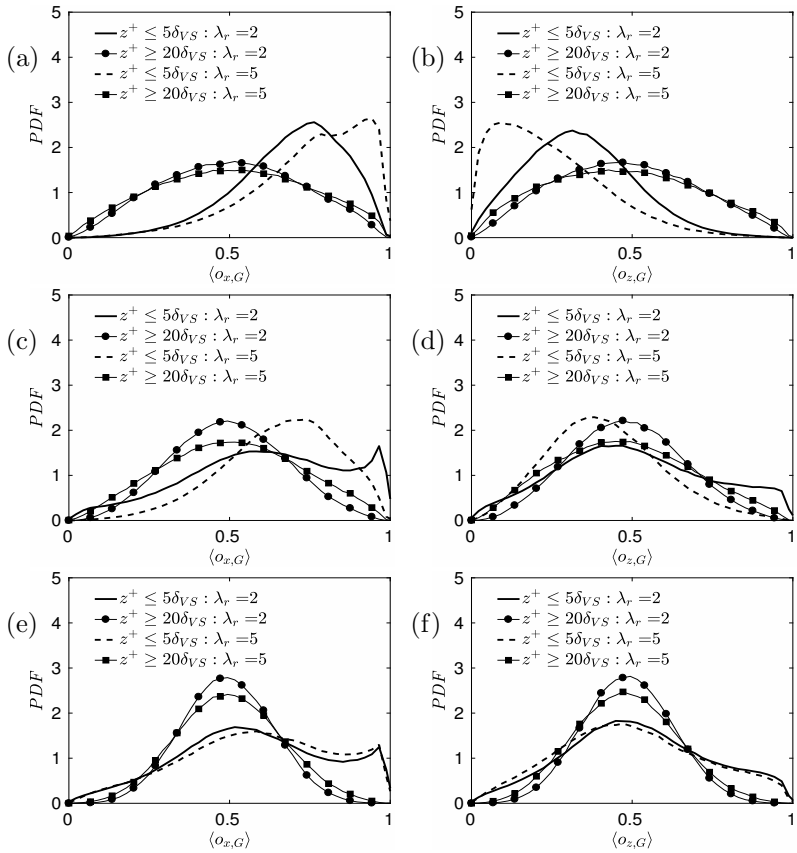

FIGURE 3.5 – Fiber mean orientation in the streamwise and wall-normal directions, $\langle o_{x,G} \rangle$ and $\langle o_{z,G} \rangle$, respectively. Subscript G indicates that the orientation of the fiber's center of mass is considered. Panels: (a), (b) $St_r = 1$; (c), (d) $St_r = 5$; (e), (f) $St_r = 30$. Solid lines represent the orientation of fibers in a near-wall slab of thickness $0 \leq z^+ < 5\delta_{VS}$ with δ_{VS} the thickness of the viscous sublayer. Symbols represent the orientation of fibers in a core-flow slab of thickness $5\delta_{VS} \leq z^+ \leq h$.

if a non-negligible λ_r-dependence is observed. What is more interesting to discuss is the behaviour of the near-wall PDF, which changes significantly between $St_r = 5$ and $St_r = 30$. At the intermediate Stokes (panels (c) and (d) in Fig.[3.5]), the PDFs of the $\lambda_r = 5$ fibers are just slightly skewed, indicating that the increase in fiber inertia has reduced the tendency to attain a preferential orientation within the flow. The PDF of $\langle o_{x,G} \rangle$ for the $\lambda_r = 2$ fibers (panel (c) in Fig.[3.5]), however, exhibits a sharp peak at values close to unity, which is associated to a marked drop in the PDF of ho $\langle o_{z,G} \rangle$ (panel (d) in Fig.[3.5]). This peak is due to fiber trapping in a thin region very close to the wall: In this region, alignment with the mean flow direction is determined by the geometric constraint imposed by the

presence of the wall in combination with the fiber-wall interaction model adopted in the present study. The striking difference between the $PDFs$ occurring at $St_r = 5$ is lost almost completely at $St_r = 30$: In this latter case, fiber inertia is high enough to damp any effect due to the fiber aspect ratio in the near-wall region. More in general, fiber flexibility is seen to become of secondary importance when fiber inertia is large.

Preferential Concentration and Near-Wall Segregation

Because of inertia, elongation and flexibility, the macroscopic outcome of fiber translational and orientational behaviour is twofold: A non-homogeneous spatial distribution is attained in both the wall-normal and wall-parallel directions. To characterize statistically such distributions, we focus here on two observables: The fiber particle number density, referred to as concentration hereinafter (shown in Fig.[3.6]), and the PDF of the fluid velocity fluctuations sampled by the fibers in the near-wall region (shown in Fig.[3.8]).

Fiber concentration, $C_G/C_{0,G}$, is computed as follows:

1. the flow domain is divided into N_s wall-parallel fluid slabs of equal thickness;
2. the number $N_{f,s}(t^+)$ of fibers with center of mass G falling in each fluid slab at a given time step is counted;
3. the number density $C_G(t^+) = N_{f,s}(t)/V_s$ is computed, with V_s the volume of the s^{th} slab;
4. the normalised concentration is obtained dividing $C_G(t^+)$ by its initial value $C_{0,G} = C_G|_{t^+=0}$.

By doing so, values of $C_G/C_{0,G}$ larger (resp. smaller) than unity indicate accumulation (resp. depletion) of fibers. Profiles shown in Fig.[3.6] refer to time $t^+ = 1250$ of the simulations and were obtained using $N_s = 300$. To highlight the effect of flexibility on wall-normal accumulation, profiles for flexible fibers (lines in Fig.[3.6]) are contrasted with profiles for "equivalent" rigid fibers having the same physical and geometrical parameters (symbols in Fig.[3.6]). At low fiber inertia (Fig.[3.6](a)), the concentration of flexible fibers in the near-wall region is always higher than that of rigid fibers, indicating that flexible fibers experience a stronger wallward turbophoretic drift. This allows a more efficient trapping of the flexible fibers inside the viscous sublayer, in particular within 2 or 3 viscous units from the wall.

At intermediate inertia (Fig.[3.6](b)), the largest differences are observed for the shorter $St_r = 5$ fibers: In this case, the peak of concentration for

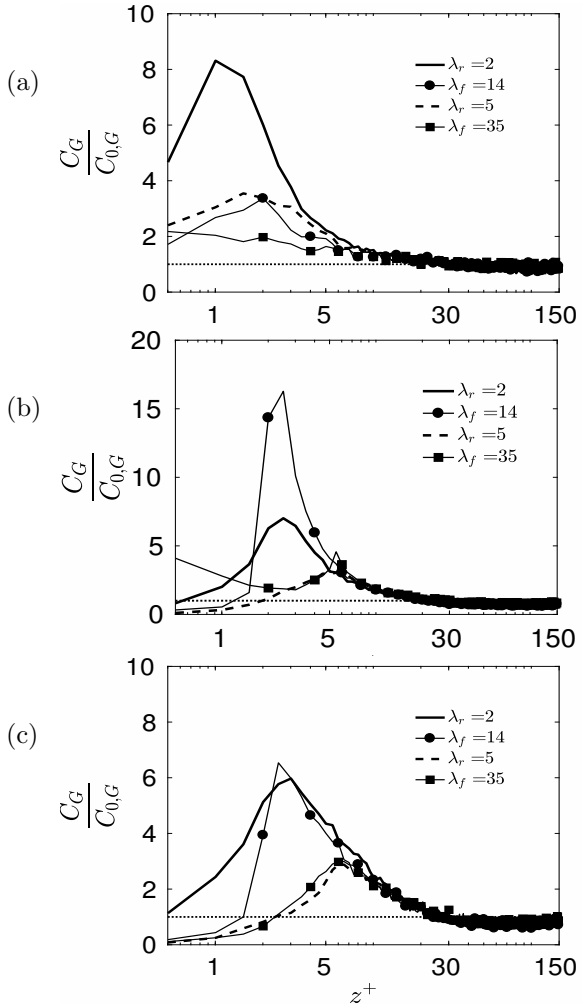

FIGURE 3.6 – Profiles are taken at time $t^+ = 1250$. Panels: (a) $St_r = 1$; (b) $St_r = 5$; (c) $St_r = 30$.

flexible fibers (solid line), located at $z^+ \simeq 2.5$, is significantly lower than that of the rigid fibers (circles), but the number of flexible fibers in the last 1.5 viscous units from the wall is higher. The concentration profile for the longer $St_r = 5$ fibers (dashed line) does not differ much from that of the rigid fibers (squares), even if a slightly lower peak of concentration is observed for the flexible fibers. Examining now the $St_r = 30$ fibers (Fig.[3.6](c)), we observe again that flexibility is associated to stronger accumulation in close proximity to the wall, especially in the $\lambda_r = 2$ case. In this case, it can also be noted that the peak value of concentration is not much affected by the increase of inertia (this value being nearly the same as that obtained for

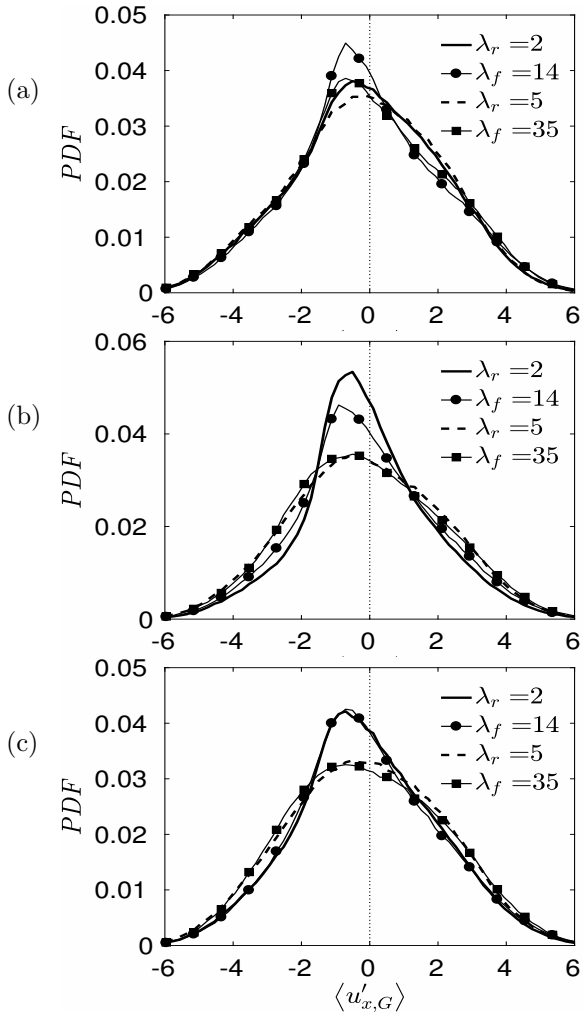

FIGURE 3.7 – PDF of the fluid velocity fluctuations sampled at the position of the fiber's center of mass G in the near-wall region (in a fluid slab $\Delta z^+ = 30$ thick). Panels: (a) $St_r = 1$; (b) $St_r = 5$; (c) $St_r = 30$.

the $St_r = 5$ fibers), whereas a strong decrease is found for the rigid fibers (from $C_G/C_{0,G} \simeq 16$ in panel (b) to $C_G/C_{0,G} \simeq 6$ in panel (c)). Overall, rigid fibers seem to be more sensitive to a change in their inertia as far as wall-normal accumulation is concerned, and flexibility appears to produce significant quantitative modifications to concentration profiles.

The analysis of concentration profiles indicates that, in agreement with the findings of previous studies on pointwise spherical particles (see Soldati and Marchioli (2009) for a review) and rigid fibers (Marchioli et al., 2010), wall

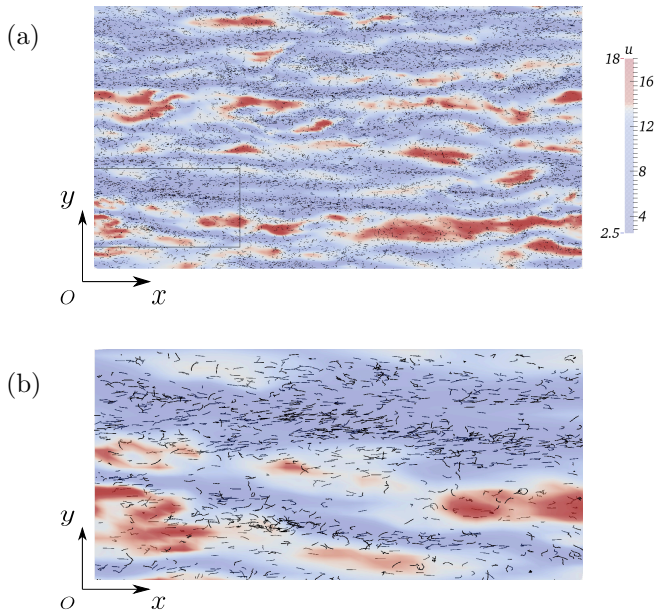

FIGURE 3.8 – Instantaneous fiber distribution in the near-wall region. For visualization purposes, only the $St_r = 5$ fibers with $\lambda_r = 5$ in the slab $0 < z^+ < 30$ are shown. The colormap shows the streamwise fluid velocity fluctuations (red: high-speed streaks with $u'_{G,x} > 0$, blue: low-speed streaks with $u'_{G,x} < 0$). Panel (b) is a close-up view of the rectangular region highlighted in panel (a).

accumulation of flexible fibers is driven by turbophoresis and modulated by fiber inertia. In view of this analogy, it is therefore natural to expect similarities in the spatial distribution of the trapped fibers, namely formation of elongated streaks within the low-speed regions of the flow. A sample snapshot of the instantaneous distribution of the flexible fibers in the present simulation setting is provided in Fig.[3.8].

The $St_r = 5$ fibers with $\lambda_r = 5$ are chosen as reference for visualisations. The correlation between fiber clusters and low-speed regions (in blue) is quite clear, and can be appreciated better in the close-up view of Fig. [3.8](b), where high-speed regions (in red) appear depleted of particles. To quantify this correlation, in Fig.[3.7] we show the PDF of the streamwise fluid velocity fluctuations, $\langle u'_{x,G} \rangle$, sampled at the position of the fiber's center of mass G. The PDF is conditioned to the wall-normal location of G: Only fibers with center of mass within a near-wall region of thickness $\Delta z^+ = 30$, considered as trapped, where taken into account for the calculation. For comparison purposes, the $PDFs$ for flexible fibers (lines) are shown together with the $PDFs$ for rigid fibers with the same physical and geometrical parameters (symbols). As previously, angular brackets denote triple averaging: Over all elements of a single fiber, over all fibers in the

selected fluid slab and over time. Comparing the three panels of Fig.[3.7], the following observations can be made. First, the effect of flexibility on segregation into low-speed streaks is limited to fibers with low or intermediate inertia: In the $St_r = 1$ case, the peak of the PDF for both the $\lambda_r = 2$ fibers and the $\lambda_r = 5$ fibers in the negative hu $\langle u'_{x,G} \rangle$ semi-plane decreases with respect to the rigid fibers and the curve is more negatively skewed in the positive $\langle u'_{x,G} \rangle$ semi-plane, indicating weaker segregation; in the $St_r = 5$ case, the peak of the PDF for the $\lambda_r = 2$ fibers in the negative $\langle u'_{x,G} \rangle$ semi-plane increases and the curve is less negatively skewed in the positive $\langle u'_{x,G} \rangle$ i semi-plane, indicating stronger segregation. In all other cases, namely $St_r = 5$ fibers with $\lambda_r = 5$ and $St_r = 30$ fibers (regardless of the aspect ratio), the deviation of the PDFs is minor indicating no effect on segregation. In particular, as the Stokes number is increased, inertia appears to dominate over flexibility even if changes in the shape of the PDF due to the different fiber elongation become more evident: Longer fibers, no matter if rigid or flexible, exhibit stronger tendency to segregate in low-speed streaks, in agreement with the findings of Marchioli et al. (2010).

The statistical observables discussed in this section demonstrate that flexibility can lead to significant quantitative changes in the macroscopic phenomena associated to inertia-driven preferential concentration, and that the importance of these changes on fiber dynamics depends in a non-trivial way on aspect ratio.

Bending

One crucial aspect of fiber dynamics is bending, induced by the fluid velocity gradients acting along the fiber. Even if our study is based on a point-particle approach, the model used to approximate the fiber can take into account the effect due to a spatial change of velocity gradients by considering their value at the center of each element composing the fiber. Fig.[3.9] provides a qualitative visualization of the instantaneous distribution of the $St_r = 5$ fibers in a fluid slab of size $698 < x^+ < 1021$, $297 < y^+ < 559$, $0 < z^+ < 120$; the fluid structures in blue represents the Q-criterion in the range $[-0.05, -0.008]$: To quantify bending, we use the three-dimensional fiber end-to-end distance, which is the distance between the end points of the fiber. When the fiber is fully stretched, it means that the end-to-end distance is equal to the fiber length L_f^+, when the end-to-end distance is zero, the two end points of the fiber touch each other.
In particular we study the fiber end-to-end distance (expressed in wall units), for two different subsets: fibers in the near wall region and fibers in the center of the channel. Statistics are shown for all fiber sets in Fig.[3.10]. Curves are conditioned to the location of the fiber in the wall-normal direction as in Fig.[3.5]: The length of a fully-stretched fiber, represented by the

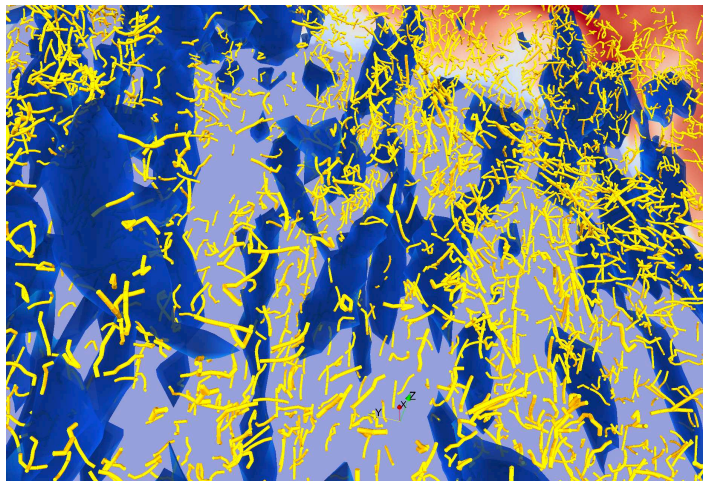

FIGURE 3.9 – Instantaneous distribution of $St_r = 5$ fibers in turbulent channel flow. For visualization purposes, only fibers in the slab $698 < x^+ < 1021$, $297 < y^+ < 559$, $0 < z^+ < 120$ are shown; the fluid structures in blue represents the Q-criterion in the range $[-0.05, -0.008]$. Colormaps at the sides of the slab show the streamwise fluid velocity distribution (red: higher-than-mean velocity, blue:lower-than-mean velocity

horizontal thin solid lines in Fig.[3.10], is $L_f^+ = 4.7$ (resp 11.75) for a fiber with $\lambda_r = 2$ (resp. $\lambda_r = 5$): Lower values of L^+ indicate bending.
Starting from the initial time step of the simulations (in which the fibers are fully stretched as initial condition) we observe a decrease of L^+ for all fiber sets and in all regions. In general we can see that the fibers in the near-wall region (lines), reach the steady state condition earlier than the fibers in the center of the channel (symbols). Moreover the fibers with low apect ratio reach the steady state condition earlier than the fibers with higher aspect ratio.
In the $St_r = 1$ case (Fig.[3.10](a)), the steady state value of L^+ for the fibers in the near-wall region is the same for the fibers in the center of the channel for both the aspect ratios. The fibers with lower λ_r, in the near-wall region (solid line) reach the steady state condition at $t^+ \simeq 75$ while those in the center of the channel (line with circles) reach the steady state condition at $t^+ \simeq 150$. The trend is similar for the fibers with higher λ_r. The fibers in the near wall region (dashed line), reach the steady state at $t^+ \simeq 150$; while those in the center of the channel (line with squares), reach the steady state condition at $t^+ \simeq 300$.
In the $St_r = 5$ case (Fig.[3.10](b)), the steady state values of L^+ for the fibers in the near-wall region is higher indicating lower deformation (this effect being higher for $\lambda_r = 2$). This is also observed at higher fiber inertia, as can be seen in Fig.[3.10](c). As before, the state state condition is reached earlier by the fibers in the near-wall region and with lower aspect

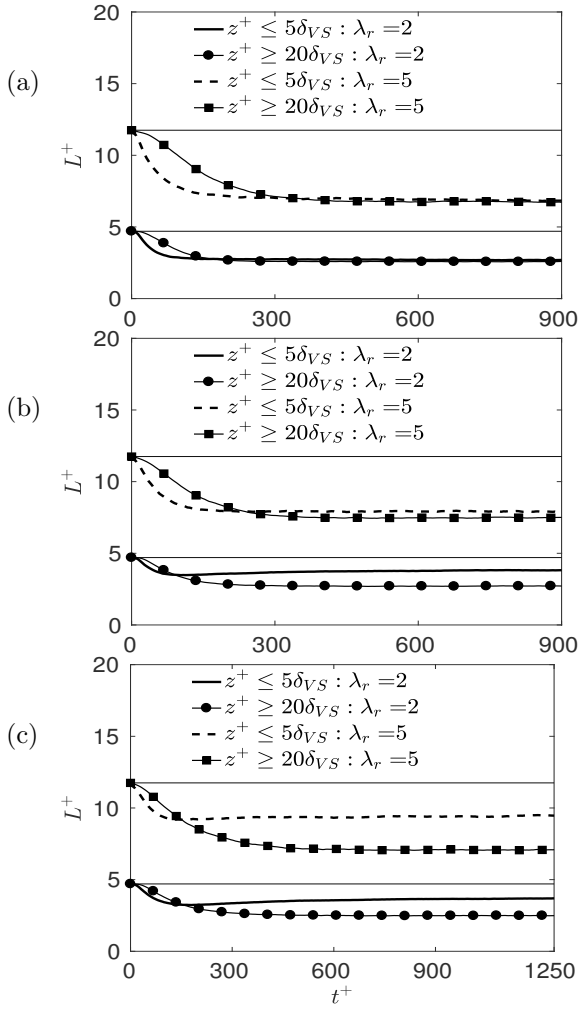

FIGURE 3.10 – Dimensionless time behaviour of fiber end-to-end distance, L^+. Panels: (a) $St_r = 1$; (b) $St_r = 5$; (c) $St_r = 30$.

ratio. This occurs also for the $St_r = 30$ case.
The results shown in Fig.[3.10] indicate that mean fiber deformation is characterized by an initial transient during which fibers adapt to the local flow conditions and "forget" about the imposed initial condition. This transient is generally shorter in the near-wall region due to the persistent action of the mean shear, while fibers in the bulk of the flow (especially those in the center region of the channel) are subject to a nearly delta-correlated flow field. Eventually, a steady state is always reached, and the effect of flow anisotropy on mean deformation is felt only at sufficiently high fiber inertia ($St_r > 1$ in the present simulations).

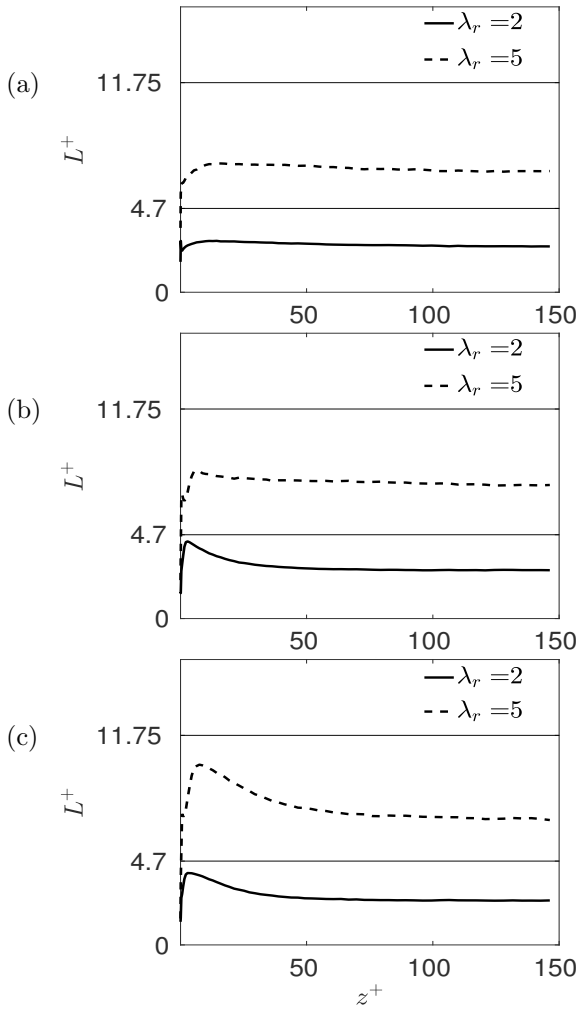

FIGURE 3.11 – Dimensionless fiber end-to-end distance, L^+. Panels: (a) $St_r = 1$; (b) $St_r = 5$; (c) $St_r = 30$.

Once the steady state is reached, it is possible to correlate the end-to-end distance with the wall-normal coordinate. This correlation is shown in dimensionless form (wall units) and for all fiber sets in Fig.[3.11].
Profiles refer to a mean distance, averaged over all fibers in the flow domain and in time (over the last 90 viscous time units of the simulation). As in Fig.[3.10] the length of a fully-stretched fiber is represented by the horizontal thin solid lines. Starting from the wall and moving away from it, we observe an increase of L^+ for all fiber sets. In the $St_r = 1$ case (Fig.[3.11](a)), this increase continues up to $z^+ \simeq 20$: beyond this point, the curves reach a plateau that is maintained throughout the core region of

the flow. The plateau value of L^+ is roughly equal to 60% of L_f^+ regardless of the element's aspect ratio. In the $St_r = 5$ case (Fig.[3.11](b)), L^+ reaches a rather sharp maximum at $z^+ \simeq 10 - 15$, indicating local stretching, and then drops to a uniform value (again approximately equal to 60% of L_0^+) beyond $z^+ \simeq 50$ from the wall. In the $St_r = 30$ case (Fig.[3.11](c)), the maximum of L^+ is more evident and corresponds to a wider region of fiber stretching. As before, we find that the ratio of the end-to-end distance to the length of the fully-stretched fiber is roughly equal to 0.6. It also suggests that fiber bending away from the wall is weakly dependent on St_r and λ_r. This independency can be attributed to the fact that, outside of the buffer layer, the length of one fiber element is significantly smaller than the local Kolmogorov scale and the length of the entire fiber is smaller than $7\eta_k$, value for which fiber rotation is independent of inertia (Parsa et al., 2012). The conclusion of effect of turbulence on fiber's bending is the same for the steady state part of the Fig.[3.10].
We remark that, once the steady state is reached, the region of higher stretching correlates well with the region of maximum turbulent Reynolds stress and that the strength of this correlation depends on inertia, as well as on elongation since longer fibers appear to get stretched closer to the wall than shorter ones.

In an attempt to identify a scaling behavior for the time taken by the fibers to reach a steady-state condition, we computed the correlation of the velocity fluctuation of the fluid in particle position $Corr(u_i(t^+), t^+)$ (note that in the following equation the Einstein notation for sum is not valid):

$$Corr(u_i(t^+), t^+) = \frac{\langle u_i\,(t^+)\,u_i\,(0)\rangle}{\langle u_i\,(0)\,u_i\,(0)\rangle}. \tag{3.2}$$

To compute this correlation, we divide the domain in 3 zones, the near-wall region ($z^+ \leq 5\delta_{VS}$), the intermediate region ($z^+ \in (5\delta_{VS}, 20\delta_{VS})$) and the center region ($z^+ \geq 20\delta_{VS}$). The correlation is computed following the fiber along its trajectory, and is conditioned to the region in which the fiber was initially released. In Fig.[3.12], we show this "Lagrangian conditioned correlation" for $St_r = 1$ (panels (a)-(b)) and for $St_r = 30$ (panels (c)-(d)), as well as for $\lambda_r = 2$, in panels (a) and (c), and for $\lambda_r = 5$, in panels (b) and (d).
The correlation in general decreases until the steady state (flucutation around zero) is reached. Regardless of fiber inertia and elongation, we observe that the fibers relased in the near-wall region (solid line) reach the steady state condition earlier than the fibers relased in the center of the channel (symbols).
Tab.[3.2] shows the integral time scale associated to $Corr(u_x(t^+), t^+)$ at varying St_r and λ_r:
In particular we observe that the integral time scale is an increasing (resp. decreasing) function of the Stokes number in the center of the flow (resp.

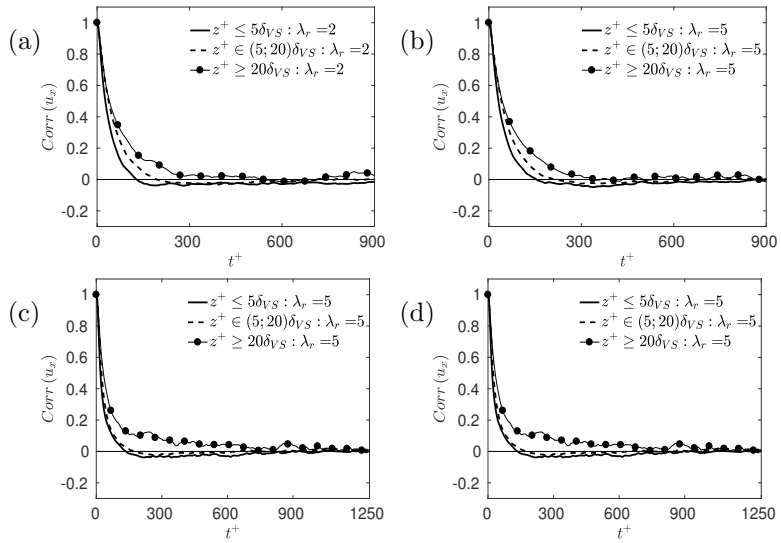

FIGURE 3.12 – Correlation of the fluctuation velocity of the fluid in particle position $Corr(u_x(t^+),(t^+)$. Panels (a): $St_r = 1$, $\lambda_r = 2$; (b) $St_r = 1$, $\lambda_r = 5$; (c) $St_r = 30$, $\lambda_r = 2$; (d) $St_r = 30$, $\lambda_r = 5$

	A_{Corr_x}					
	$St_r = 1$		$St_r = 5$		$St_r = 30$	
	$\lambda_r = 2$	$\lambda_r = 5$	$\lambda_r = 2$	$\lambda_r = 5$	$\lambda_r = 2$	$\lambda_r = 5$
$z^+ \leq 5\delta_{VS}$	18.83	27.89	10.78	13.52	10.62	14.99
$z^+ \in (5;20)\delta_{VS}$	45.11	51.25	33.69	42.26	32.07	36.03
$z^+ \geq 20\delta_{VS}$	79.55	80.1	87.46	92.74	93.12	98.9

TABLE 3.2 – Lagrangian integral time scale of $Corr(u_x(t^+),(t^+)$.

elsewhere). As expected, the time scale grows as one moves away from the wall and is an increasing function of the aspect ratio regardless of fiber inertia and of fiber release location.

We computed the same Lagrangian correlation for the end-to-end distance (in wall units) $L^+|_{lagr}$. Results are shown in Fig.[3.13]. Starting from the initial time step of the simulations (when all the fibers are stretched), we observe a decrease of $L^+|_{lagr}$ over time for all fiber sets in the near-wall region, and only for the fibers with lower inertia also in the middle and center regions. $L^+|_{lagr}$ for the fibers with higher inertia in the intermediate and center regions, decreases until a minimum and then increases until the steady state value. In general, the steady state value of this end-to-end distance for a given inertia and aspect ratio is independent to the initial position of the fibers.

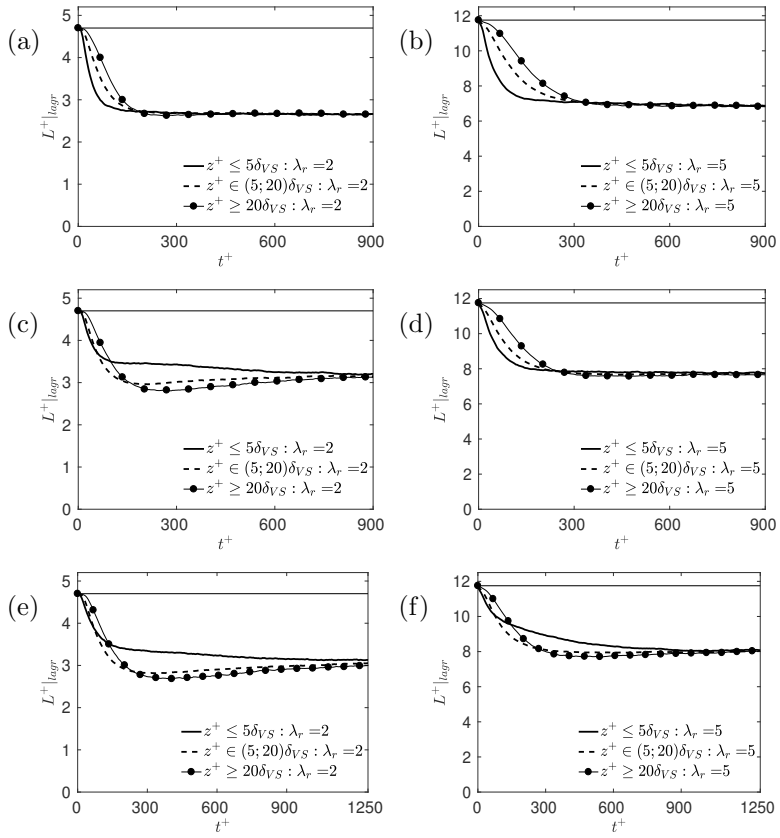

FIGURE 3.13 – Dimensionless time behaviour of fiber end-to-end distance, L^+, using a 'lagrangian evolution approach'. Rows: (a), (b) $St_r = 1$; (c), (d) $St_r = 5$; (e), (f) $St_r = 30$. Columns: (a), (c), (e) $\lambda_r = 2$; (d), (d), (f) $\lambda_r = 5$.

In the $St_r = 1$ case, the $\lambda_r = 2$ fibers (Fig.[3.13](a)) initialy released in the near-wal region (resp. the center of the chanel) reach the steady state condition at $t^+ \simeq 75$ (resp. $t^+ \simeq 150$. If we increase the aspect ratio, this trend is just shift forward. The $\lambda_r = 5$ fibers (Fig.[3.13](b)) initialy released in the near-wal region (resp. the center of the chanel) reach the steady state condition at $t^+ \simeq 150$ (resp. $t^+ \simeq 300$). In general the steady state condition is reached at the same time as in Fig.[3.10](a), regarless of the aspect ratio or the initial position.
In the $St_r = 5$ case, we observe that the fibers with lower λ_r (Fig.[3.13](c)) initially released in the near wall region follow a monotonic behaviour, while those initially released in the center of the channel show a non-monotonic behaviour with a minimum at $t^+ \simeq 300$. The fibers with higher λ_r show a similar trend. The fibers initially released in the near-wall region (resp. the

center of the channel) reach the steady state condition at $t^+ \simeq 150$ (resp. $t^+ \simeq 300$).
We observe that, in the $St_r = 30$ case (Fig.[3.13](e)(f)), regarless of the aspect ratio, the fibers initially released in the near wall region follow a monotonic behaviour, while those initially released in the center of the channel show a non-monotonic behaviour with a minimum at $t^+ \simeq 300$ as in Fig.[3.13](c).
We observe that the correlation follows the same time evolution for both fluid velocity fluctuations and end-to-end distance at low fiber inertia, indicating a clear connection between the local flow conditions experienced by the fibers and their deformation. The correlation weakens as fiber inertia increases, indicating that mean deformation is not significantly affected by the instantaneous turbulent flow (but rather by its time-persistent features, as the mean shear experienced by fibers upon accumulating in the near-wall region).

Another observable that we examine to characterize bending is the solid angle α_r between two neighbouring fiber elements, r and $r+1$:

$$\alpha_r = \mathbf{o}_r \cdot \mathbf{o}_{r+1} \quad \forall r \in [1, \mathcal{N}-1] \tag{3.3}$$

The solid angle $\alpha_r = 0$ corresponds to a situation in which r and $r+1$ have the same orientation, whereas bending is associated with $\alpha_r > 0$ (the stronger the bending, the higher the value of α_r, in particular $\alpha = \pi$ means that the the elements r and $r+1$ have the opposite orientation). In Fig.[3.14], we show the scatter-plot correlation between the mean value of the solid angle $\langle\alpha\rangle$, obtained upon averaging over all fiber elements, and the relative end-to-end distance, $L_f^+ - L^+$ (expressed in wall units), at $t^+ = 900$ for $St_r = 1$ and $St_r = 5$ and at $t^+ = 1250$ for $St_r = 30$.
Here, $L_f^+ - L^+ = 0$ represents the end-to-end distance of a fully-stretched fiber: Hence, the limiting values are $L_f^+ - L^+ = 0$, when the fiber is completely stretched, and $L_f^+ - L^+ = L_f^+$ when the two ends of a fiber touch each other. The thick solid line in each panel represents the mean value of $L_f^+ - L^+$, obtained upon ensemble averaging over all points in the scatter plot and over time (essentially to get $\langle L^+ \rangle$). Error bars represent the standard deviation from such mean value and provide a measure of the uncertainty associated with the plots. It can be noted that there is a direct proportionality between α and $L_f^+ - L^+$: Stretched (resp. bent) fibers are characterized by large (resp. small) values of both $\langle\alpha\rangle$ and $L_f^+ - L^+$, even if the distribution in the values of $\langle\alpha\rangle$ at small end-to-end distance is rather widespread.

Once the relation between L^+ and $\langle\alpha\rangle$ has been defined, we can study the PDF of the solid angle $\langle\alpha\rangle$ as is shown in Fig.[3.15]:
All fiber sets are considered, and $PDFs$ are conditioned to the location

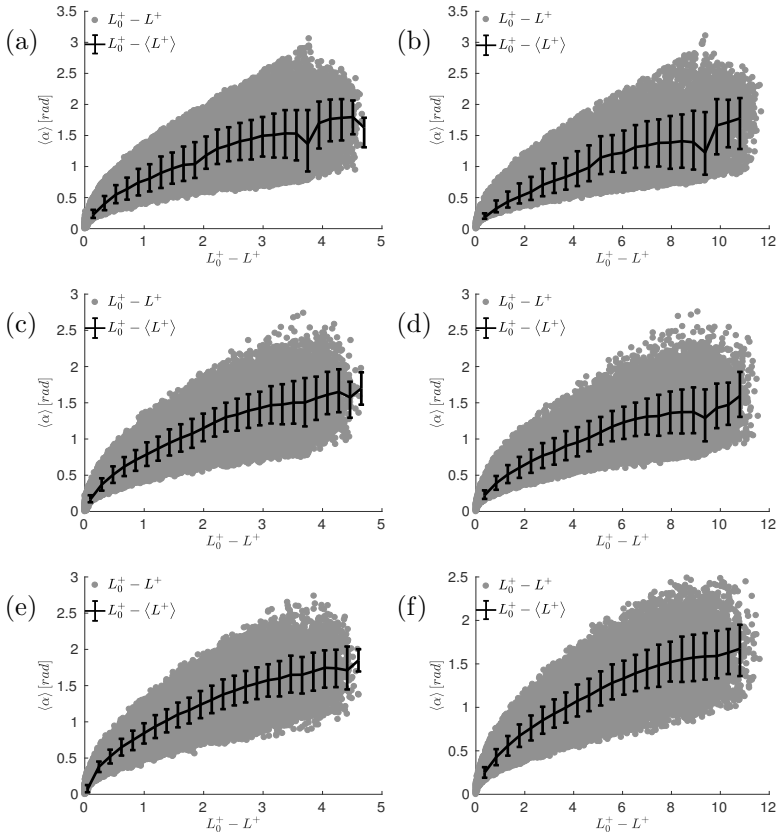

FIGURE 3.14 – Scatter plot of the correlation between the fiber end-to-end distance, $L_f^+ - L^+$, and the mean solid angle between adjacent fiber elements, $\langle \alpha \rangle$. The solid line represents the mean value of the correlation. Errorbars represent the standard deviation from the mean. Rows: (a), (b) $St_r = 1$; (c), (d) $St_r = 5$; (e), (f) $St_r = 30$. Columns: (a), (c), (e) $\lambda_r = 2$; (b), (d), (f) $\lambda_r = 5$.

of the fiber in the wall-normal direction as in Fig.[3.5]; this statistics are averaged in time (over last 90 viscous units).

In the $St_r = 1$ case, panel (a) in Fig.[3.15], we observe that the fibers in the near wall region (for both $\lambda_r = 2; 5$) sample almost uniformly all the angles in the range considered in the figure: there is a smooth peak at $\langle \alpha \rangle = 1$ and a smooth decay after this peak. The fibers in the center of the channel sample more or less the same angles $\langle \alpha \rangle$, but show a more irregular trend; there is a relative minimum in near $\langle \alpha \rangle = 0.7$ and a sharp peak is near the value $\langle \alpha \rangle = 1$. The value of $\langle \alpha \rangle \simeq 1.2$ is related to the preferential value of an uniform distribution of angles. It means that the fibers in the near wall-region and in the center of the channel sample preferentially the angles that represent (on average) a uniform distribution of deformations.

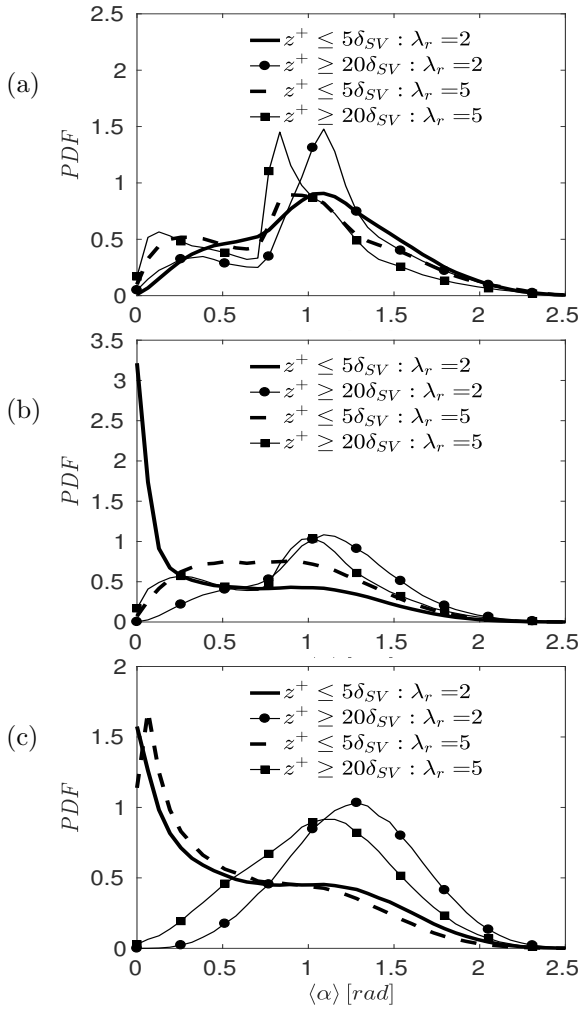

FIGURE 3.15 – PDF for the solid angle α in the near wall region and in the center of the chanel. Panels: (a) $St_r = 1$; (b) $St_r = 5$; (c) $St_r = 30$.

In the $St_r = 5$ case, panel (b) in Fig.[3.15], we observe that the fibers in the near-wall region, sample preferentially angles close to $\langle\alpha\rangle = 0$: in particular in the case $\lambda_r = 2$, there is a pronounced peak for fully stretched fibers. The fibers in the center of the channel sample almost preferentially the angles that represent (on average) a uniform distribution of deformations.
In the $St_r = 30$ case, panels (c) in Fig.[3.15], the behavior is quite similar to that just discussed for the $St_r = 5$ fibers.
We can conclude that the fibers in the center of the channel, regardless of inertia and elongation, sample preferentially the angles that represent (on average) a uniform distribution of deformations. In the near-wall region the

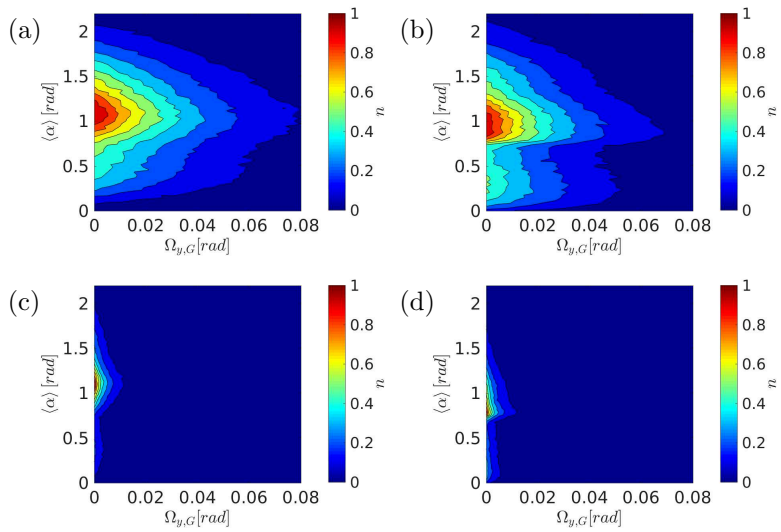

FIGURE 3.16 – Correlation between $\langle\alpha\rangle$ and $\langle\Omega_{G,y}\rangle$ for fibers with $St_r = 1$. Upper panels refer to the near-wall region, lower panels related to the bulk region; left $\lambda_r = 2$, right $\lambda_r = 5$

fibers with high (resp. low) inertia sample preferentially lower deformation angles (resp. angles that represent a uniform distribution of deformations).

Intuitively, one could argue that the observed trends for the deformation angle correlate with the mean shear rate acting on the fibers, especially in the near-wall region. To characterize and quantify this relation, in Figs.[3.16], [3.17] and [3.18] we show the correlation between the solid angle $\langle\alpha\rangle$ with the mean vorticity sampled by the center of mass of the fibers in spanwise direction $\langle\Omega_{y;G}\rangle$. The colormap shows regions of high correlation in red and regions of low correlation in blue.
agrees well with the trends shown in Figs.[3.10] and [3.15].
At lower inertia, the fibers in the near-wall region (Fig.[3.16](a)(b)) sample high values of the $\langle\Omega_{G,y}\rangle$ but are deformed more or less in the same way as those in the center of the channel (Fig.[3.16](c)(d)). In particular the peaks in Fig.[3.15](a) at $\langle\alpha\rangle \simeq 1$ are recovered here.
At intermediate inertia ($St_r = 5$, Fig.[3.17]) we observe that the fibers in the near-wall region (panels (a) and (b)), sample high values of $\langle\Omega_{G,y}\rangle$ and are more stretched, than deformed, particularly in the case $\lambda_r = 2$. The fibers in the center of the channel, regardless of aspect ratio, sample low values of vorticity in spanwise direction and are more deformed (panels (c) and (d) in Fig.[3.17]).
At high inertia ($St_r = 30$, Fig.[3.18]) we observe that, regardless of the aspect ratio, the fibers in the near-wall region (panels (a) and (b)), sample

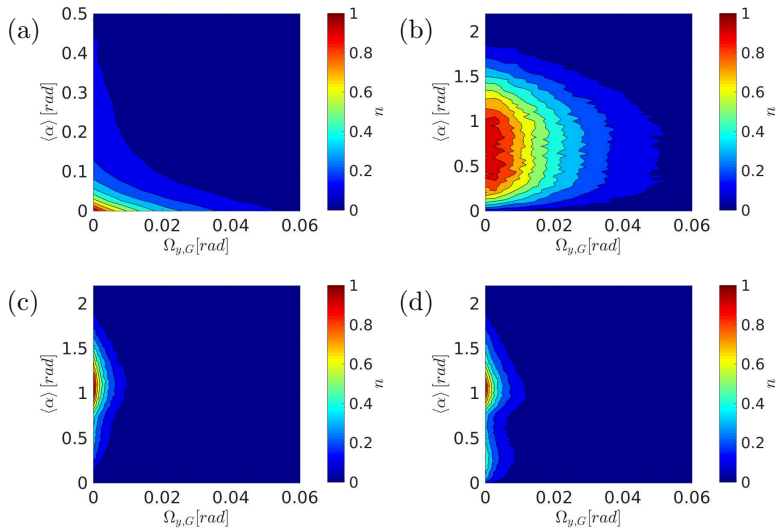

FIGURE 3.17 – Correlation between $\langle\alpha\rangle$ and $\langle\Omega_{G,y}\rangle$ for fibers with $St_r = 5$. Upper panels refer to the near-wall region, lower panels related to the bulk region; left $\lambda_r = 2$, right $\lambda_r = 5$

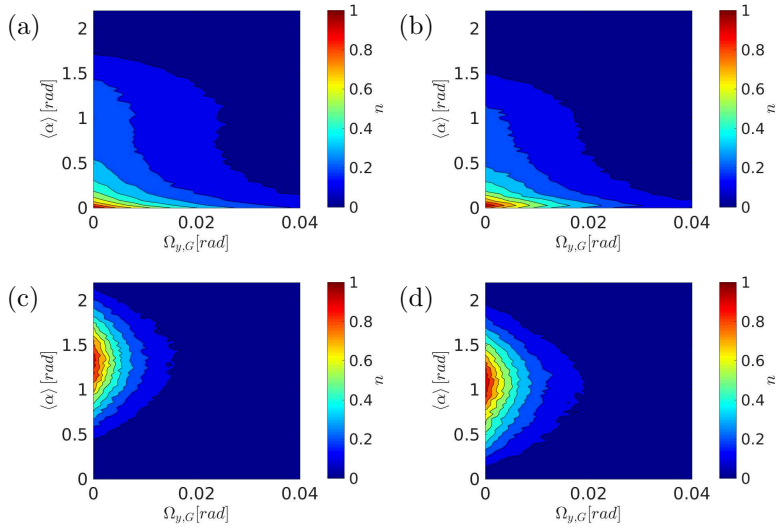

FIGURE 3.18 – Correlation between $\langle\alpha\rangle$ and $\langle\Omega_{G,y}\rangle$ for fibers with $St_r = 30$. Upper panels refer to the near-wall region, lower panels related to the bulk region; left $\lambda_r = 2$, right $\lambda_r = 5$

high values of $\langle\Omega_{G,y}\rangle$ and are stretched; while in the center of the channel,

they sample low values of vorticity in spanwise direction and are much more deformed (panels (c) and (d)).
To conclude, the results shown for the bending, suggest that the fibers in the center of the channel, regardless of inertia, are more deformed because they can sample an almost 'isotropic' and 'homogeneous' turbulent environment (as shown in Fig.[3.11]). On the other hand the fibers with high inertia in the near-wall region are stretched by the mean shear rate. Moreover, analysis of $\langle\alpha\rangle$ could lead to interesting findings about the importance of bending stiffness (which was not included in the present simulations). From Figs.[3.15]-[3.18], we see that, in the near-wall region, the most natural (or statistically probable) state for fibers with high inertia fibers is the stretched one, which corresponds to low values of $\langle\alpha\rangle$: In this case, bending stiffness would not play a very important role in fiber dynamics. On the other hand, we find significant near-wall deformation for fibers with low inertia, corresponding to high values of $\langle\alpha\rangle$: If the bending stiffness of these fibers would be accounted for, then they would drain a non-negligible amount of energy from the fluid. The same would apply to fibers in the center of the channel, regardless of their inertia.
The bending dynamics observed so far and the effect of the fluid velocity gradients on fiber deformation can be interpreted by means of the constraint forces generated within the fiber. These forces are computed directly by the Lagrangian tracking described in sec.[2.3]. The forces parallel and orthogonal to the direction of the axis of the elements are respectively:

$$\mathbf{X}_r \cdot \mathbf{o}_r \quad \forall r \in [2, \mathcal{N}],$$

$$\mathbf{X}_r \times \mathbf{o}_r \quad \forall r \in [2, \mathcal{N}].$$

The behavior of these forces along the wall-normal direction is shown in Fig.[3.19]:
Profiles refer to forces averaged over the last 90 viscous time units of the simulation.
Starting from the wall, and moving towards the center of the channel, we notice an increase of the forces $\mathbf{X}_r \cdot \mathbf{o}_r$ and $\mathbf{X}_r \times \mathbf{o}_r$ until a peak is reached: The location of this peak almost coincides with the location at which fiber concentration reaches a maximum (see also Fig.[3.6]). Beyond the peak, the curves decrease monotonically all the way to the center of the channel for all fiber sets. Fibers with higher aspect ratio, have higher values for both the forces $\mathbf{X}_r \cdot \mathbf{o}_r$ and $\mathbf{X}_r \times \mathbf{o}_r$. Since the trend for the parallel and the orthogonal components of the constraint force is similar (just scaled) the description of the Fig.[3.19] is given regardless of the type of the force.
In general the increasing of the force is related to inertia: fibers high inertia develop high constraint forces to avoid relative translation.
The aspect ratio plays an important role in this dynamcs: The fibers with higher aspect ratio are able to simultaneously sample different fluid regions. This means stronger interaction between elements with to respect to the

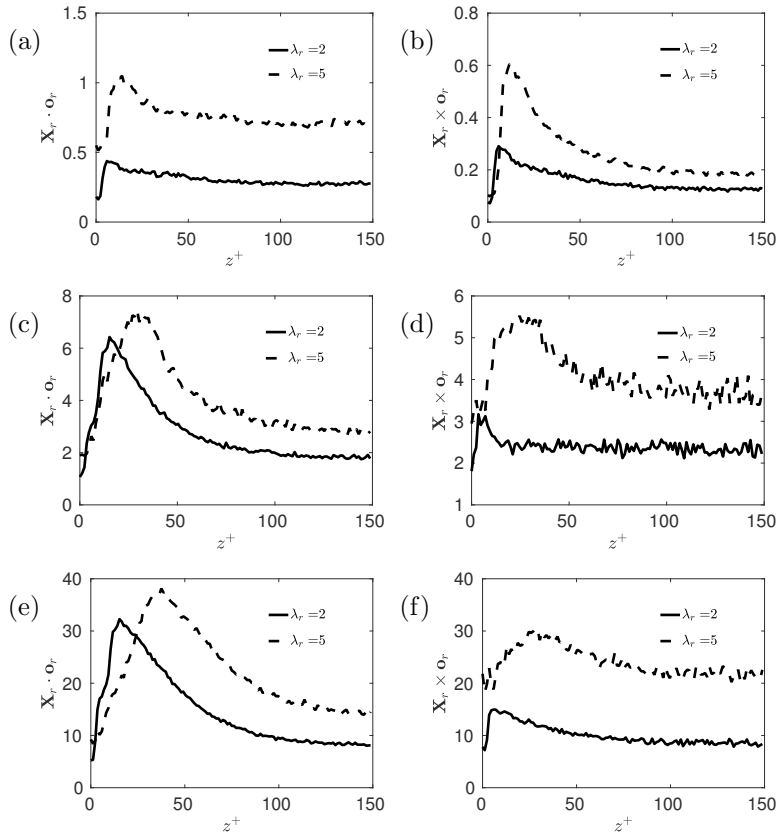

FIGURE 3.19 – Fiber constraint force in axial and orthogonal direction of the fiber, $\mathbf{X}_r \cdot \mathbf{o}_r$ and $\mathbf{X}_r \times \mathbf{o}_r$, respectively. Panels: (a), (b) $St_r = 1$; (c), (d) $St_r = 5$; (e), (f) $St_r = 30$. Columns: (a), (c), (e) $\mathbf{X}_r \cdot \mathbf{o}_r$; (d), (d), (f) $\mathbf{X}_r \times \mathbf{o}_r$.

fibers with lower aspect ratio.
For all sets, we observe that the peak is in the near-wall region (in particular near the value of maximum concentration Fig.[3.6]). In fact in this region the momentum transferred by the fluid to the fibers has a maximum.

4

Semi-Dilute Suspension of Flexible Fibers

"The answer my friend is blowing in the wind".

- Bob Dylan, *Blowing in the wind*

In this chapter, we characterize from a statistical point of view the behavior of a semi-dliute suspension of fibers. We first provide a summary of the simulations, followed by a comprehensive statistical analysis of fluid and fiber dynamics under the $two-way$ coupling regime.

Summary of the Simulations

In this second part of the chapter we examine the dynamics of a semi-dilute suspension of flexible fibers in turbulence (i.e. $\mathbf{f}_{2w} \neq 0$ but contacts among the fibers are still not considered). The analysis is made still neglecting bending stiffness effects and considering fully-elastic rebound with the wall. Simulations are run at the same Reynolds number considered for the dilute suspension flow, and the same time step size is used. The total Lagrangian tracking time in wall units is $t^+ = t\nu/u_\tau^2 = 1250$, which was enough to reach the steady state in fiber wall-normal concentration.
In this study, we have selected the following dimensionless values: $a^+ = 0.17$, $\lambda_r = 2, 5$, and $St_r = \tau_p/\tau_f = 30$. To ensure converged statistics, swarms of $N_m = 2 \cdot 10^5$ fibers, each having $\mathcal{N} = 7$ elements (as in Andrić et al. (2013)), are tracked for each combination of values in the (λ_r) space, assuming $two-way$ coupling between the phases. The corresponding volume fractions are $\Phi_V \simeq 1.6 \cdot 10^{-4}$ for $\lambda_r = 2$, and $\Phi_V \simeq 4.0 \cdot 10^{-4}$ for $\lambda_r = 5$, whereas the percent mass fractions are in the range $\Phi_M^{\%} < 38.4$ for $\lambda_r = 2$ and $\Phi_M^{\%} < 62.2$ for $\lambda_r = 5$. The parameters are summarized in Tab.[4.1]. We recall that the Kolmogorov length scale, has a mean value $\eta_{K,avg}^+ \simeq 2$, and varies from $\eta_{K,min}^+ \simeq 1.62$ at the wall to $\eta_{K,max}^+ \simeq 3.61$ at the channel

center (Picciotto et al., 2005).
The time scale in this conditions is $\epsilon_R^- \simeq 6.67 \cdot 10^{-2}$.

St_r	λ_r	a^+	ρ_p^+	L_f^+	St_f	Φ_V	$\Phi_M^{\%}$
30	2	0.17	3071.8	4.7	64.9	$1.6 \cdot 10^{-4}$	38.4
30	5	0.17	1996.5	11.8	54.5	$4.0 \cdot 10^{-4}$	62.2

TABLE 4.1 – Summary of the parameters in the simulations

Results and Discussion

Our aim is to quantify the effect considering suspensions with higher volume and mass fractions on the macroscopic fluid and particle dynamics: several statistical observables discussed in this section provide direct comparison against the dilute regime. We start by considering modifications to the flow field. In Figs.[4.1], [4.2] and [4.3] we compare the vortical flow structures as obtained using the well-known $Q - criterion$. The $Q - criterion$ is defined as Chong et al. (1990):

$$Q = \frac{1}{2}\left[\left(\frac{\partial u_i}{\partial x_i}\right)^2 - \frac{\partial u_i}{\partial x_j}\frac{\partial u_j}{\partial x_i}\right], \tag{4.1}$$

and represents an adequate tool to identify regions of simultaneous high strain-rate and low vorticity.
The snapshot at $t^+ \simeq 1200$ and with $Q \simeq -0.01$ in Figs.[4.1], [4.2] and [4.3] show the istantaneaus flow structures in the planes $x - z$ (side-view), $x - y$ (top-view) and $y - z$ (front-view) respectively. Top (resp. bottom) panels refer to $one - way$ (resp. $two - way$) coupled simulations.

The flow fields related laden with the fibers with $St_r = 30$ and $\lambda_r = 2$ are chosen as reference for visualisations.
In particular, we notice that, for the selected value of Q, structures in $one - way$ couple simulations appear to be more evenly distributed and more concentrated in the near-wall region.
However since the Figs.[4.1]- [4.3] refer to a single instant of the simulations, they can only provide a qualitative indication of two-way coupling effects and are not sufficient to determine the extent of flow field modifications. This quantification is provided in the next sections, where fluid and fiber statistics are discussed.

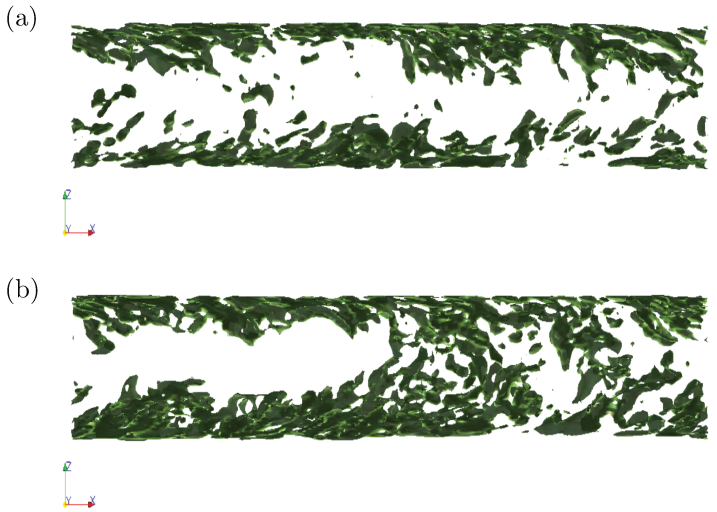

FIGURE 4.1 – Instantaneous ($t^+ \simeq 1200$) plot of the $Q-criterion$ (iso-surface $Q \simeq -0.01$) in the $x-z$ plane. For visualization purposes, only the flow field related to fibers with $St_r = 30$ and $\lambda_r = 2$ in the slab $450 < y^+ < 500$ is shown. Panels: (a) $one-way$ coupling, (b) $two-way$ coupling.

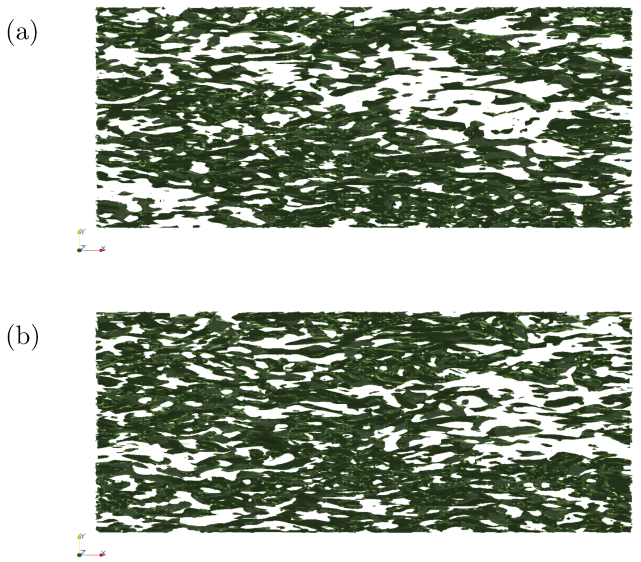

FIGURE 4.2 – Instantaneous ($t^+ \simeq 1200$) plot of the $Q-criterion$ (iso-surface $Q \simeq -0.01$) in the $x-y$ plane. For visualization purposes, only the flow field related to fibers with $St_r = 30$ and $\lambda_r = 2$ in the slab $z^+ < 30$ is shown. Panels: (a) $one-way$ coupling, (b) $two-way$ coupling.

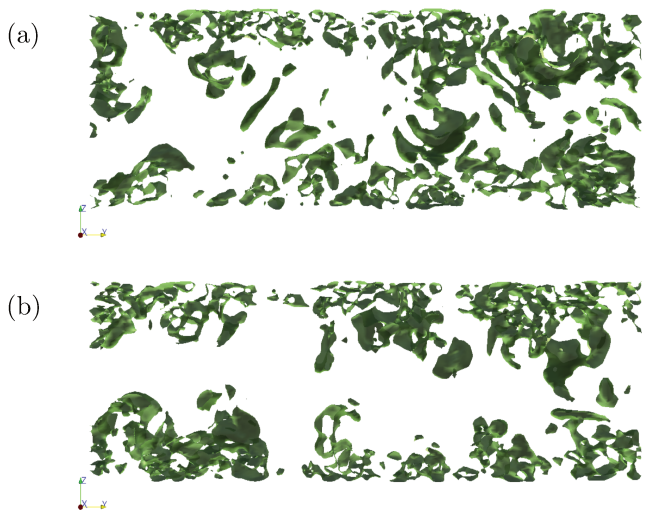

FIGURE 4.3 – Instantaneous ($t^+ \simeq 1200$) plot of the $Q - criterion$ (iso-surface $Q \simeq -0.01$) in the $y - z$ plane. For visualization purposes, only the flow field related to fibers with $St_r = 30$ and $\lambda_r = 2$ in the slab $x^+ < 50$ is shown. Panels: (a) $one - way$ coupling, (b) $two - way$ coupling.

Fluid Results

To examine the modification induced by the $two - way$ coupling on the flow field, we consider first the wall-normal profile of the reaction force in the x-direction and z-direction, $\mathbf{f}_{2w}^{-}|_x$ and $\mathbf{f}_{2w}^{-}|_z$ respectively. This force is defined in the eq.[2.100] and represents the feedback force applied by the flexible fibers on the surrounding fluid, as shown in the Fig.[4.4]. Since the forces $\mathbf{f}_{2w}|_x, \mathbf{f}_{2w}|_y$ are added as source terms in the Navier-Stokes eq.[2.7] they are plotted in the Fig.[4.4] with "$-$" units.
It is apparent that, for both the aspect ratios ($\lambda_r = 2$ - line with circles - and $\lambda_r = 5$, - line with squares -) the average value of the reacting force in x-direction and in z-direction is higher than zero in the near-wall region and vanishes when the center of the channel is approached. This is due to the fact that, as we will see in the Fig.[4.9], the flexible fibres in the near-wall region, even in $two - way$ coupling regime tend to segregate into low speed streaks. In this way the momentum transferred from the particles to the surrounding fluid is higher than zero in the near-wall region and decreases as we move away from the wall.
Moreover it is appearent that fibers with higher mass ($\lambda_r = 5$) can transfer higher momentum to the surrounding fluid than fibers with a lower mass ($\lambda_r = 2$).

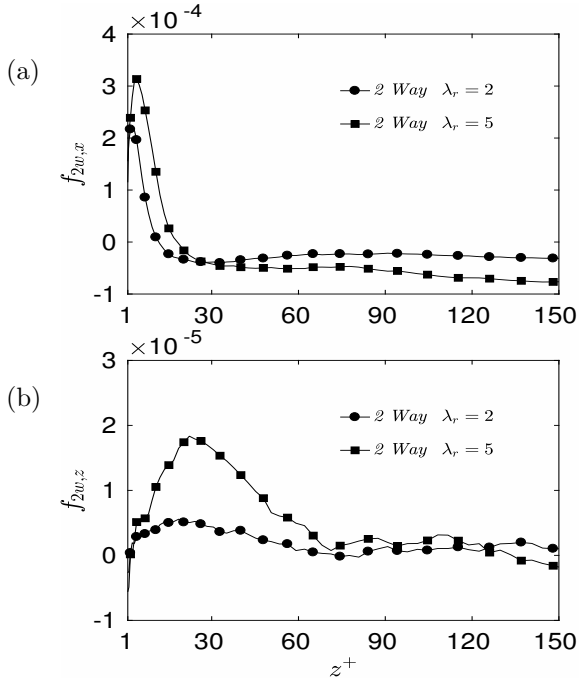

FIGURE 4.4 – Panel (a), $\mathbf{f}^+_{2w}|_x$ term, panel (b) $\mathbf{f}^+_{2w}|_x$ term. Lines with circles for $\lambda_r = 2$, lines with squares for $\lambda_r = 5$).

To quantify the $two-way$ effects, we start by examining the statistics of the flow field. In Fig.[4.5] we show the mean streamwise fluid velocity $\langle u_x \rangle$, and RMS of the streamwise and wall-normal fluid velocity $RMS(u_x), RMS(u_z)$, respectively. Lines refer to $one-way$ coupling case, symbols refer to $two-way$ coupling cases.
As we can see $two-way$ cases results overlap almost perfectly with those of one-way coupling regardless of the aspect ratio, indicating no effect on the mean flow rate.
We can observe some differences in the RMS. The RMS of the fluid streamwise velocity (resp. wall-normal velocity) as shown in Fig.[4.5](b)) (resp. as shown in Fig.[4.5](c)) is higher for $z^+ < 30$ (resp. for $z^+ > 45$).
These results, which provide evidence of almost negligible effects on turbulent fluctuations, are in agreement with those reported by Zhao et al. (2013) for rigid fibers and volume fractions of the same order of magnitude.

For a further quantification of $two-way$ coupling effects we can study the transport equation for the turbulent kinetic energy k:

$$\frac{Dk}{Dt} = P + T + \Pi + D - \epsilon, \tag{4.2}$$

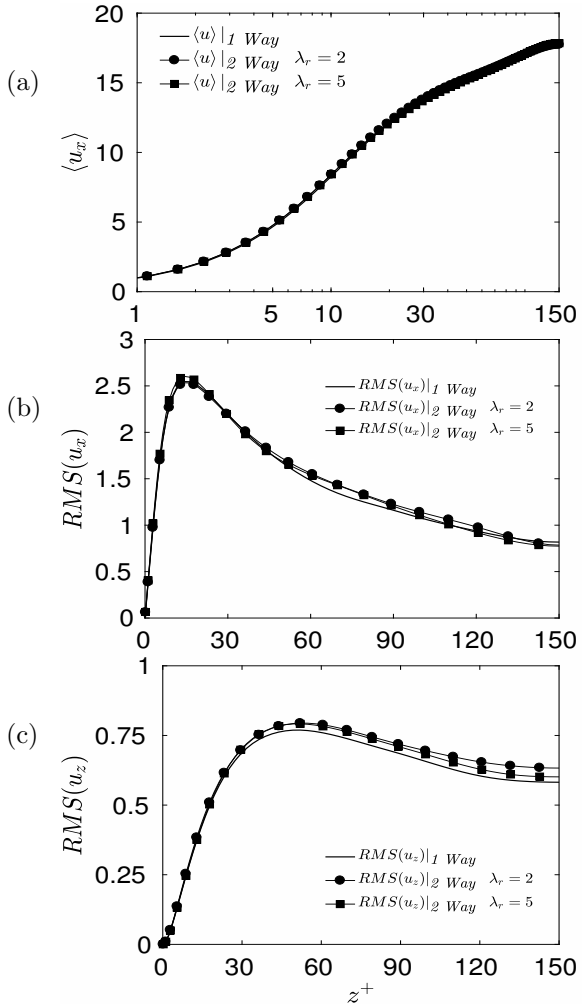

FIGURE 4.5 – Fluid velocity in $one - way$ case (straight line) and $two - way$ cases (lines with symbols - circles for $\lambda_r = 2$, squares for $\lambda_r = 5$). Panels: (a) Mean value of u_x; (b) $RMS(u_x)$; (c) $RMS(u_z)$.

where the different terms, or energy budgets are defined as:

- $k = Turbulent\ Kinetic\ Energy$:

$$k = \rho_f \left\langle u_i' u_i' \right\rangle , \tag{4.3}$$

- $P = Production\ rate$:

$$P = -2\rho_f \left\langle u_i' u_j' \right\rangle \frac{\partial u_i}{\partial x_j}, \tag{4.4}$$

- T = *Turbulent transport rate*:

$$T = -\rho \frac{\partial}{\partial x_j} \left\langle u_i' u_i' u_j', \right\rangle, \tag{4.5}$$

- Π = *Pressure gradient term*:

$$\Pi = -\left\langle u_i' \frac{\partial p'}{\partial x_i} \right\rangle, \tag{4.6}$$

  where, $p' = p - \langle p \rangle$ is the pressure fluctuation.

- D = *Viscous diffusion rate*:

$$D = -\mu \frac{\partial^2}{\partial x_i \partial x_i} \left\langle u_i' u_i' \right\rangle, \tag{4.7}$$

- ϵ = *Dissipation rate*:

$$\epsilon = 2\mu \left\langle \frac{\partial u_i'}{\partial x_j} \frac{\partial u_i'}{\partial x_j} \right\rangle. \tag{4.8}$$

In dimensionless form (wall units), the equation has the same form:

$$\frac{Dk^+}{Dt^+} = P^+ + T^+ + \Pi^+ + D^+ - \epsilon^+. \tag{4.9}$$

Upon averaging over the homogeneous directions, terms in eq.[4.9] read as:

- k^+ = *Turbulent Kinetic Energy*:

$$k^+ = \left\langle u_x^{+'} u_x^{+'} \right\rangle, \tag{4.10}$$

- P^+ = *Production rate*:

$$P^+ = -2 \left\langle u_x^{+'} u_z^{+'} \right\rangle \frac{\partial u_x^+}{\partial z^+}, \tag{4.11}$$

- T^+ = *Turbulent transport rate*:

$$T^+ = -\frac{\partial}{\partial z^+} \left\langle u_i^{+'} u_i^{+'} u_z^{+'} \right\rangle, \tag{4.12}$$

- Π^+ = *Pressure gradient term*:

$$\Pi^+ = -\left\langle u_z^{+'} \frac{\partial p^{+'}}{\partial z^+} \right\rangle, \tag{4.13}$$

- $D^+ =$ *Viscous diffusion rate*:

$$D^+ = -\frac{\partial^2}{\partial \left(z^+\right)^2} \left\langle u_i^{+'} u_i^{+'} \right\rangle, \tag{4.14}$$

- $\epsilon^+ =$ *Dissipation rate*:

$$\epsilon^+ = 2 \left\langle \frac{\partial u_i^{+'}}{\partial x_j^+} \frac{\partial u_i^{+'}}{\partial x_j^+} \right\rangle. \tag{4.15}$$

The most important terms from a quantitative point of view are the production rate P^+, the viscous diffusion rate D^+ and the dissipation rate ϵ^+. These terms are shown in Fig.[4.6](a)(b)(c) respectively.
Profile are time-averaged over the last 300 viscous time units.
Overall, we notice again negligible modifications due to the inclusion of two-way coupling in the simulations. Similar observations were made by Zhao et al. (2013).

Wall-normal Concentration and Near-wall Segregation

In this section we want to examine how the inclusion of $two-way$ coupling can influence wall-normal concentration and the near-wall segregation. In other words we want to see how inter-phasial momentum exchange can compete with inertia, elongation and flexibility in determining the spatial distribution in both wall-normal and streamwise directions. To this aim we focus of the fibers number density and the PDF of the velocity fluctuations sampled by the fibers in the near wall-region. A snapshot of the instantaneous distribution is provided in Fig.[4.7].
The $St_r = 30$ fibers with $\lambda_r = 2$ in the $one-way$ and $two-way$ cases are chosen as reference for visualisations (at $t^+ = 1250$). The background colormap shows the modulus of the fluid velocity. $One-way$ coupled fibers (Fig.[4.7](a)), seem to concentrate more in the near-wall region than the $two-way$ coupled fibers (Fig.[4.7](b)). To corroborate this qualitative observation, in Fig.[4.8] we show the near-wall concentration C/C_0. Profiles shown in Fig.[4.8] refer to time $t^+ = 1250$ and were obtained using $N_s = 150$ equal slabs. Profiles for $two-way$ coupled fibers (line with symbols in Fig.[4.8]) are contrasted with profiles for $one-way$ coupled fibers having the same physical and geometrical parameters (lines in Fig.[4.8]).
For fibers with $\lambda_r = 2$ Fig.[4.8](a) the peak value of the wall-normal concentration is higher for the $one-way$ case ($C/C_0|_{max} \simeq 5.8$) compared to the $two-way$ counterpart ($C/C_0|_{max} \simeq 4.9$). The same occurs for the fibers with $\lambda_r = 2$ Fig.[4.8](b) the maximum value of the wall-normal concentration is higher for the $one-way$ case ($C/C_0|_{max} \simeq 2.9$) compared to

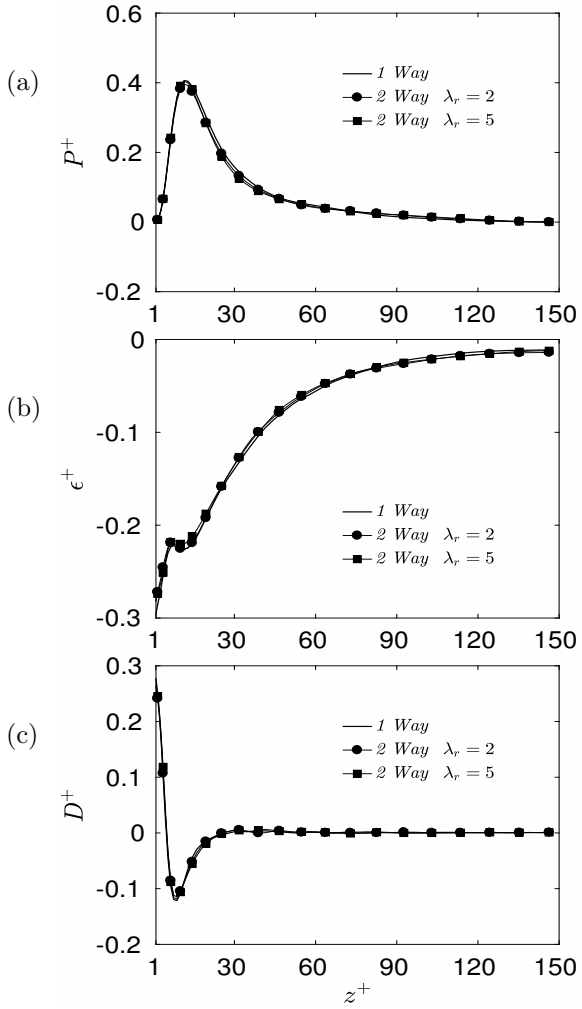

FIGURE 4.6 – Energy budgets. Production rate P^+ (a); Viscous diffusion rate D^+ (b); Dissipation rate ϵ^+ (c). Solid line represents $one-way$ coupling case; line with symbols represents $two-way$ coupling cases ($\lambda_r = 2$ - line with circles - $\lambda_r = 5$ - line with squares -)

the $two-way$ counterpart ($C/C_0|_{max} \simeq 2.3$). In other words $two-way$ coupled particles seem to be less sensitive to the turbophoretic effect. This reduced sensitivity may explain the weak of $two-way$ coupling on the flow field. Since the peak of concentration is nowhere very high, the exchange of momentum between the fibers and the surrounding fluid is relatively uniform and there are no regions of the flow that are particularly affected by this exchange.

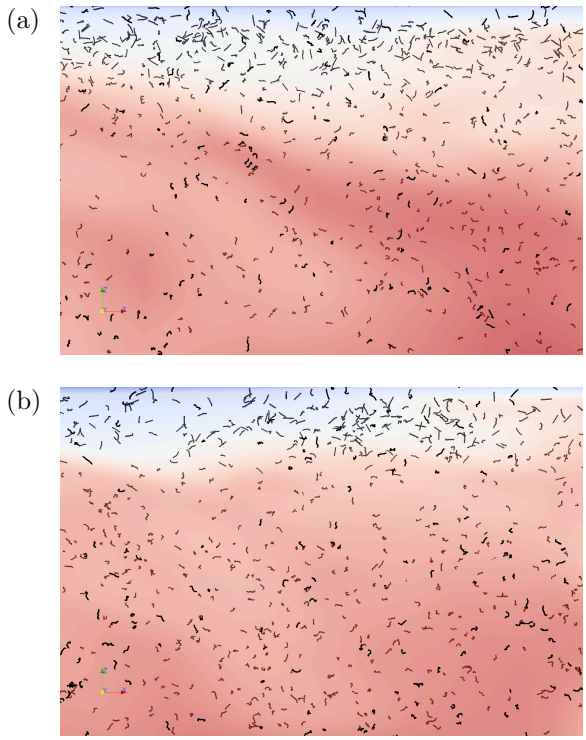

FIGURE 4.7 – Instantaneous fiber distribution in the near-wall region. For visualization purposes, only the $St_r = 2$ fibers with $\lambda_r = 30$ in the slab $1150 < x^+ < 1400$, $670 < y^+ < 780$, $z^+ > 180$ are shown. The colormap shows modulus of the fluid velocity (red: high-speed fluid flow, blue: low-speed fluid flow. Panel (a) is related to the $one - way$ coupling; (b) is related to the $two - way$ coupling.

To evaluate the impact of the $two - way$ coupling on the segregation of fibers trapped in near-wall streaks, in Fig.[4.9] we show the PDF of the streamwise fluid velocity fluctuations, $\langle u'_{x,G} \rangle$, sampled at the position of the fiber's center of mass G.

The same method to compute the results shown in Fig.[3.7], is used here; we just recall that the PDF is conditioned to the wall-normal location of G: Only fibers with center of mass within a near-wall region of thickness $\Delta z^+ = 30$, considered as trapped, where taken into account for the calculation.

Again, for comparison purposes, the $PDFs$ for $two - way$ coupled fibers (lines with symbols: circles for $\lambda_r = 2$ and squares for $\lambda_r = 5$) are shown together with the $PDFs$ for $one - way$ coupled fibers with the same physical and geometrical parameters (lines: solid for $\lambda_r = 2$ and dashed for $\lambda_r = 5$). Comparing curves in Fig.[4.9], we observe that the effect of $two - way$ cou-

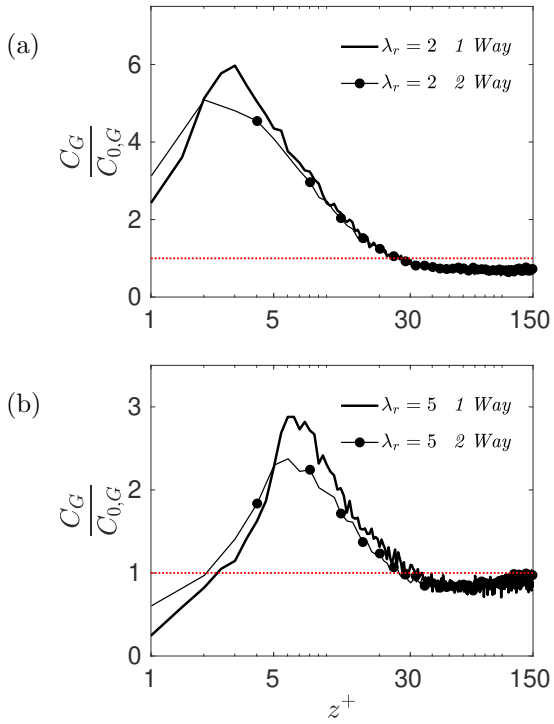

FIGURE 4.8 – Profiles are taken at time $t^+ = 1250$. Panels: (a) $\lambda_r = 1$; (b) $\lambda_r = 5$.

pling on the strength of segregation into low-speed streaks is just slightly lower with to respect to the $one - way$ case, in particular for fibers with lower aspect ratio $\lambda_r = 2$. This further proves that there are no regions in the domain that are significantly affected by the presence of the fibers.

The statistical observables discussed in this section demonstrate that $two - way$ coupling effects for the considered volume fractions lead to slightly quantitative changes in the preferential segregation, but reduce the near-wall concentration peak by $20 - 30\%$.

Velocity Statistics

The mean streamwise velocity, $\langle v_{x,G} \rangle$ of the different fiber aspect ratios is shown in Fig.[4.10](solid line and line with circles for the $one - way$ case and for the $two - way$ case respectively), together with the mean streamwise velocity, $\langle u_{x,G} \rangle$ of the fluid seen at the fiber's center of mass G (dashed line and line with squares, for the $one - way$ and $two - way$ coupling respectively). These profiles were obtained in the same way as those shown in Fig[3.2].

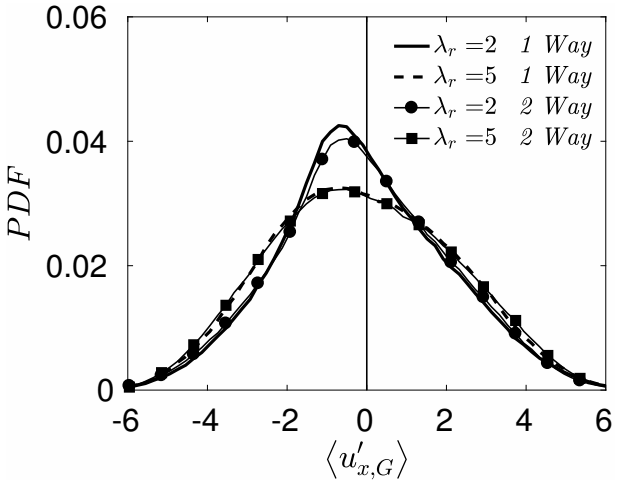

FIGURE 4.9 – PDF of the fluid velocity fluctuations sampled at the position of the fiber's center of mass G in the near-wall region (in a fluid slab $\Delta z^+ = 30$ thick). Lines represent the $one - way$ cases: solid for $\lambda_r = 2$ and dashed for $\lambda_r = 5$; Lines with symbols represent the $two - way$ cases: circles for $\lambda_r = 2$ and squares for $\lambda_r = 5$

It is apparent that, since the fluid velocity is not substantially modified by the introduction of the $two - way$ term with respect to the $one - way$ case, also the fluid velocity in the position of the center of mass of the fiber $\langle u_{x,G} \rangle$ and consequently the velocity of the fiber center of mass $\langle v_{x,G} \rangle$, are not modified.
This holds also when profiles for different aspect ratios are compared.

For a better comprehension of the $two - way$ coupling effect, we can also consider the resulting drag force exerted by the fluid on the element r, $F_r^{D,+}/m_p^+$, that is computed using eq.[2.96], and is shown in Fig.[4.11] as function of the wall-normal distance. We just recall that the values of $F_{r,x}^{D,+}/m_p^+$ are based on the Reynolds number of the single element $Re_{p,r}$, its orientation $\mathbf{o}_r$ and its relative velocity with to respect on the fluid $\mathbf{u}_r - \mathbf{v}_r$. The cross product of these last two terms, is projected along the streamwise direction.
Profiles refer to a mean value, averaged over the last 90 viscous time units. The value of the drag force has a maximum for every set at the wall, and this is due to the choice of slabs for the postprocessing.
As expected, in Fig.[4.11] we observe that the drag force is lower than zero near the wall, and it increases as we move away from the wall. Moreover since ratio $F_{r,x}^{D,+}/m_p^+$ depends on the inverse of the fiber density, it is obvious that elements with lower density ($\lambda_r = 5, \rho_p^+ = 1996.5$) experience an higher drag force than elements with higher density ($\lambda_r = 2, \rho_p^+ = 3071.8$).

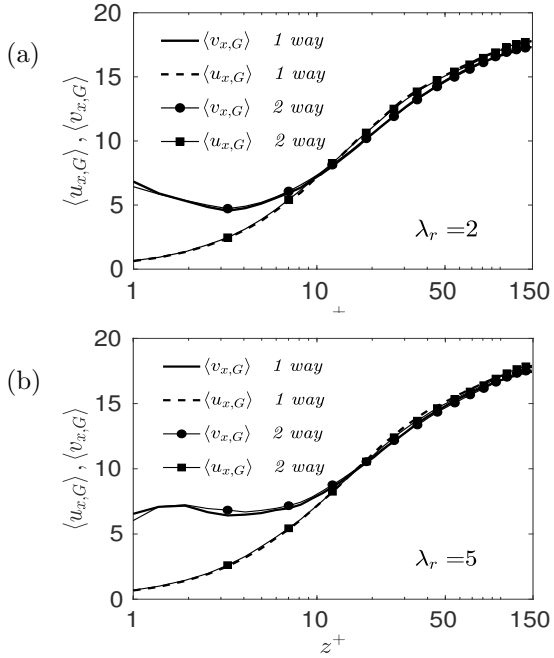

FIGURE 4.10 – Fiber mean streamwise velocity, $\langle v_{x,G}\rangle$. Subscript G indicates that the velocity at the fiber's center of mass G is considered. For comparison purposes, also the mean fluid velocity seen by the fibers is shown. Panels: (a) $\lambda_r = 2$; (b) $\lambda_r = 5$. Solid line represents the $one - way$ coupling case, line with symbols represenst $two - way$ coupling cases.

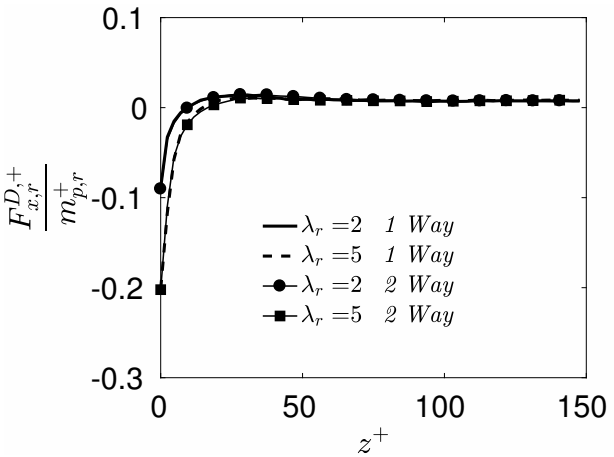

FIGURE 4.11 – Drag force exerted by the fluid on the element r. Lines represent one-way coupling results, symbols represent two-way coupling results.

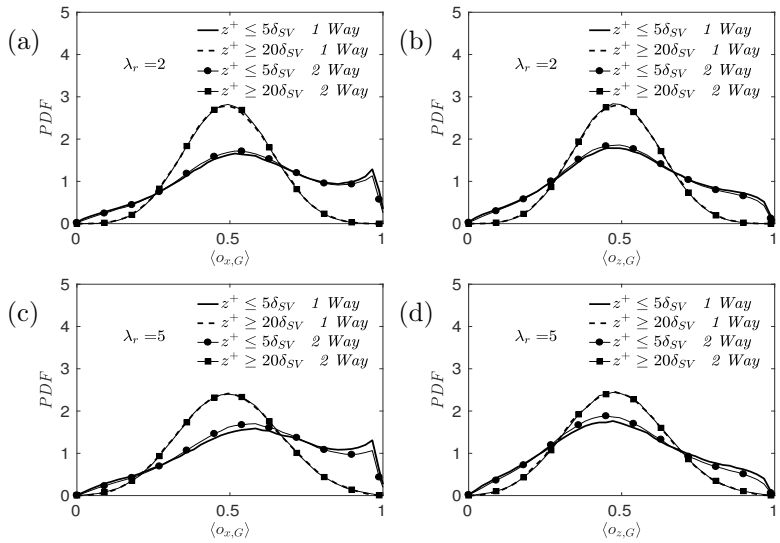

FIGURE 4.12 – Fiber mean orientation in the streamwise and wall-normal directions, $\langle o_{x,G} \rangle$ and $\langle o_{z,G} \rangle$, respectively. Subscript G indicates that the orientation of the fiber's center of mass is considered. Panels: (a), (b) $\lambda_r = 2$; (c), (d) $\lambda_r = 5$. Lines represent the $one - way$ cases: solid the orientation of fibers in a near-wall slab of thickness $0 \leq z^+ < 5\delta_{VS}$ with δ_{VS} the thickness of the viscous sublayer, dashed the orientation of fibers in in a core-flow slab of thickness $5\delta_{VS} \leq z^+ \leq h$. Lines with symbols represent the $two - way$ cases: circles the orientation of fibers in a near-wall slab of thickness $0 \leq z^+ < 5\delta_{VS}$, squares the orientation of fibers in in a core-flow slab of thickness $5\delta_{VS} \leq z^+ \leq h$.

Orientation and Bending Statistics

So far we have observed that the behavior of the fluid is weakly influenced by the presence of the particles in a semi-dilute regime; while the fibers themselves are influenced at least in terms of the preferential concentration in the near-wall region. Now we focus on the orientation and the bending of the fibers.
In Fig.[4.12], we shown the PDF of the fiber mean orientation in the streamwise and wall-normal directions, indicated as $\langle o_{x,G} \rangle$ and $\langle o_{x,G} \rangle$ respectively.

As before, lines refer to $one - way$ coupling, symbols refer to $two - way$ coupling. It is apparent that no effect is produced on the mean angular velocity of the fiber. We observe an almost perfect superimposition between the $one - way$ and the $two - way$ coupling, for both the aspect ratios and the orientations considered (o_x and o_z for $\lambda_r = 2$ in Fig.[4.12](a) and Fig.[4.12](a) resp.) and (o_x and o_z for $\lambda_r = 5$ in Fig.[4.12](c) and Fig.[4.12](d) resp.). So we can recall the observations made in sec.[3.3].
From this, we can argue that, regardless of the coupling regime, even the

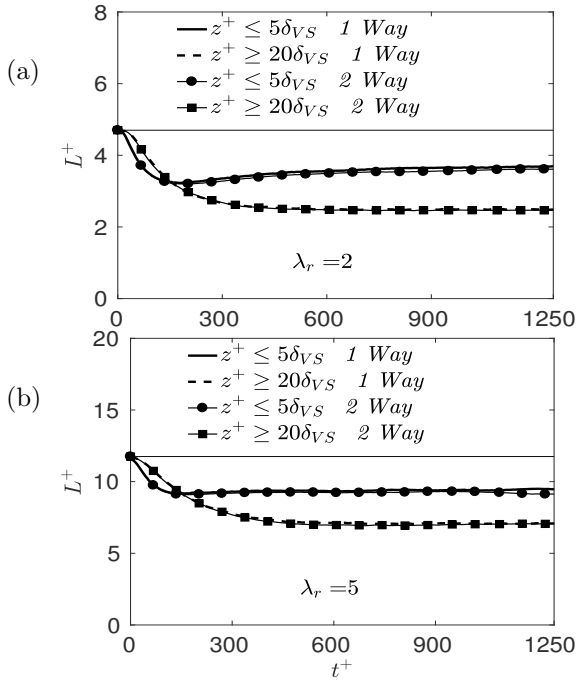

FIGURE 4.13 – Dimensionless time behaviour of fiber end-to-end distance, L^+. Panels: (a) $\lambda_r = 2$; (b) $\lambda_r = 5$. Lines represent the $one - way$ coupling cases: solid the orientation of fibers in a near-wall slab of thickness $0 \leq z^+ < 5\delta_{VS}$ with δ_{VS} the thickness of the viscous sublayer, dashed the orientation of fibers in in a core-flow slab of thickness $5\delta_{VS} \leq z^+ \leq h$. Lines with symbols represent the $two-way$ cases: circles the orientation of fibers in a near-wall slab of thickness $0 \leq z^+ < 5\delta_{VS}$ with δ_{VS} the thickness of the viscous sublayer, squares the orientation of fibers in in a core-flow slab of thickness $5\delta_{VS} \leq z^+ \leq h$.

mean angular velocity of the fiber is the same (not shown here).

We consider fiber deformation induced by fluid velocity gradients acting along the fiber, and we quantify deformation in terms of the fiber end-to-end distance. In Fig.[4.13] we show the time behaviour of the end-to-end distance for two different fibers sub-sets: fibers in the near-wall region and fibers in the center of the channel, as in Fig.[4.12]:
As in $one - way$ we observe a decrease of L^+ for the cases and negligible modifications due to the introduction of fiber feedback on the fluid.
Regardless of the aspect ratio (Fig.[4.13](a) for $\lambda_r = 2$ fibers and Fig.[4.13](b) for $\lambda_r = 5$ fibers), the trend for $one - way$ and $two - way$ coupled fibers is similar and we can recall the consideration made in the description of the Fig.[3.10]. In the near wall-region and in the center of the channel curves are basically overlapping.

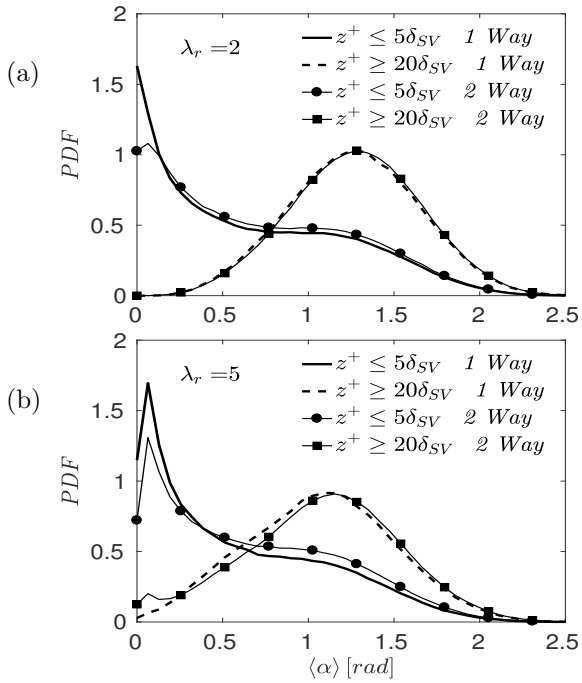

FIGURE 4.14 – PDF for the solid angle α in the near wall region and in the center of the chanel. Panels: (a) $\lambda_r = 2$; (b) $\lambda_r = 5$. Lines represent the $one - way$ cases: solid the orientation of fibers in a near-wall slab of thickness $0 \leq z^+ < 5\delta_{VS}$, dashed the orientation of fibers in a core-flow slab of thickness $5\delta_{VS} \leq z^+ \leq h$. Lines with symbols represent the $two - way$ cases: circles the orientation of fibers in a near-wall slab of thickness $0 \leq z^+ < 5\delta_{VS}$, squares the orientation of fibers in in a core-flow slab of thickness $5\delta_{VS} \leq z^+ \leq h$.

Interestingly, the almost negligible modifications induced by the term of $two - way$ on the end to end distance become more evident (even if still not striking) on the deformation angle. These are shown in Fig.[4.14], where we consider the PDF of the solid angle for the fibers near the wall and in the center of the channel and we compare the $one - way$ and $two - way$ coupling cases:

We observe that fibers in the near-wall region for both the aspect ratios ($\lambda_r = 2$ in Fig.[4.14](a) and $\lambda_r = 5$ in Fig.[4.14](b)), are more deformed in the $one - way$ case (thick solid line), than in the $two - way$ case (line with circles). The deformation of the fibers in the center of the channel, regardless of the aspect ratio, is the same for the $one - way$ and the $two - way$ cases.

We can argue that the higher deformation for the $one - way$ coupling with respect to the $two - way$ coupling is induced by the mean shear layer sampled in this region by the inertial fibers.

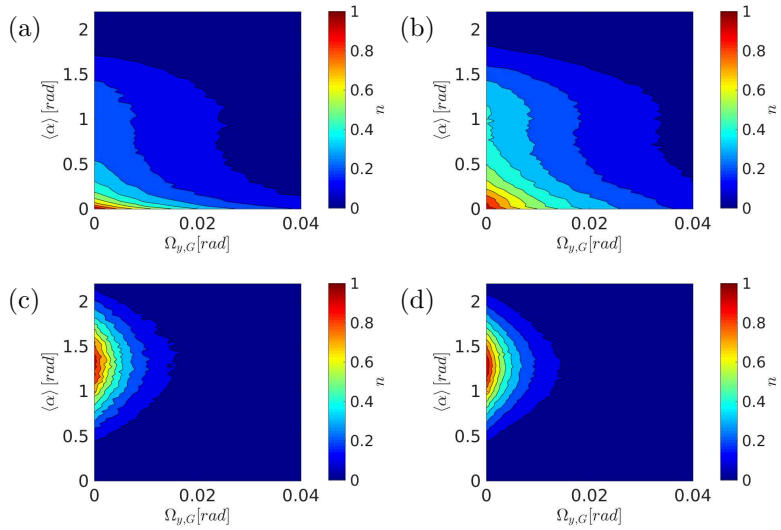

FIGURE 4.15 – Correlation between $\langle\alpha\rangle$ and $\langle\Omega_{G,y}\rangle$ for fibers with $St_r = 30$ and $\lambda_r = 2$. Panels: (a) and (b) respectively $one - way$ and $two - way$ coupling in the near-wall region ($z^+ \leq 5\delta_{VS}$); (c) (d) respectively $one - way$ and $two - way$ coupling in the near-wall region ($z^+ \geq 20\delta_{VS}$)

For flexible fibers in a dilute regime we already discussed the close relation between the mean vorticity sampled by the fibers in spanwise direction and the bending angle (see Figs.[3.16]-[3.18]). In Figs.[4.15] and [4.16], we examine the persistence of this relation is valid also for flexible fibers in a semi-dilute regime.

We recall here that the colormap shows regions of high correlation in red and regions of low correlation in blue.

For all the considered aspect ratio, we compare again $one - way$ and $two - way$ results for two fiber sub-sets: Fibers in the near-wall region (Fig.[4.15](a) for $one - way$ Fig.[4.15](b) for $two - way$ coupled fibers resp.) and those in the center of the channel (Fig.[4.15](c) for $one - way$ Fig.[4.15](d) for $two - way$ coupled fibers resp.)

As aspected, in the center of the channel the correlation is basically the same, regardless of the aspect ratio: $\langle\Omega_{G,y}\rangle$ seems to not affect the fibers deformation in this region.

Instead, in the near-wall region, the behaviour of the $one - way$ coupled fibers differs from that of the $two - way$ coupled fibers: in particular these latter seem to be more deformed. This might be due to the fact that the fibers in dilute suspension sample preferentially higher values of $\langle\Omega_{G,y}\rangle$ than fibers in the semi-dilute suspension.

In other words the $two - way$ coupling term increases the deformation fo fibers in the near-wall region. In the center of the channel the modifications

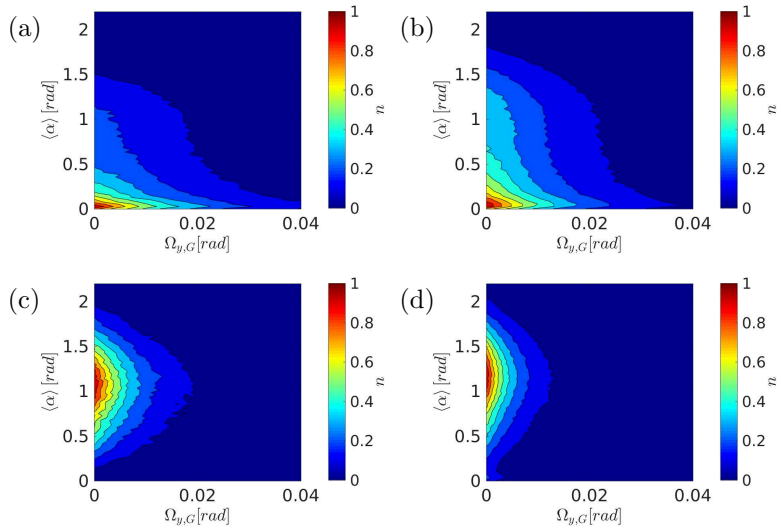

FIGURE 4.16 – Correlation between $\langle\alpha\rangle$ and $\langle\Omega_{G,y}\rangle$ for fibers with $St_r = 30$ and $\lambda_r = 5$. Panels: (a) and (b) respectively $one-way$ and $two-way$ coupling in the near-wall region ($z^+ \leq 5\delta_{VS}$); (c) (d) respectively $one-way$ and $two-way$ coupling in the near-wall region ($z^+ \geq 20\delta_{VS}$)

induced by the $two-way$ coupling term are negligible and we can retrieve the dynamics already discussed with reference to Fig.[3.10].

5

Conclusions

In the first part of the thesis, the dynamics of flexible fibers in a dilute suspension disperse in a turbulent channel flow was examined using DNS and Lagrangian fiber tracking. The rod-chain model of Lindström and Uesaka (2007) was chosen because it reproduces quite reasonably the behaviour of elongated flexible fibers in unsteady flow. Results obtained for several combination of values sampling the (λ_r, St_r) space indicate clearly that the coupling between fiber translation and fiber rotation changes significantly their wall-ward flux with respect to rigid fibers with the same geometrical and physical parameters.

This effect of flexibility adds to those of elongation and inertia, leading to a quantitative different build-up of fibers at the wall. In turn, this leads to stronger accumulation in the very-near-wall region, where flexible fibers appear to be trapped, segregated and preferentially-oriented by the same physical mechanism (turbophoresis) that govern preferential concentration of spherical particles and rigid fibers in bounded flows. In other words the macroscopic turbulent phenomena that govern the motion of spheres and rigid fibers, play an even more important role in the motion of flexible fibers. In the buffer layer and in the viscous sublayer, bending of flexible fibers with large (resp. small) inertia is reduced (resp. enhanced) by mean shear and turbulent Reynolds stresses. This suggest that the bending stiffness would not (resp. would) play an important role in the dynamics of near-wall flexible fibers.

Future developments to be investigated regarding the dynamics of a dilute suspension of flexible fibers are the effect of bending stiffness on fiber deformation, the dependence of fiber deformation on the flow Reynolds number and the impact of spatial filtering on fiber motion. In particular, the inclusion of an internal resistance torque in the rod-chain model equations will allow a more realistic representation of fiber bending dynamics and hopefully provide information about the formation of fiber flocs or hang-ups in regions of fiber preferential concentration. Fiber bending is ultimately determined by the hydrodynamic fluid-fiber interaction, and therefore a dependency on the flow Reynolds number should be expected. In partic-

ular at Reynolds numbers significantly higher than $Re_\tau = 300$ (based on the channel height), for which turbulence intensity increases and local gradients become more intermittent. To simulate high-Re_τ flows, the DNS-based approach adopted in this study might become computationally unfeasible, and calculations based on Large-Eddy simulation of turbulence could be preferred. In this case, however, fibers would evolve in a spatially-filtered flow field (especially on coarse grids) and would not be exposed to the action of the sub-grid fluid velocity fluctuations, which are known to affect the tendency of inertial particles to concentrate preferentially (Marchioli, 2017). Investigations are under way to examine the effect of filtering on the motion of the flexible fibers, and to assess the conditions (e.g. grid coarseness) under which a closure model is needed in the equation of fiber motion.

In the second part of the thesis, the dynamics of a semi-dilute suspension of flexible fibers dispersed in a turbulent channel flow was examined. The $two-way$ coupling model of Gualtieri et al. (2014) was chosen because it reproduces quite reasonably the effect due to the transfer of momentum from the particles to the fluid in a turbulent flow. Results obtained for a semi-dilute suspension of inertial flexible fibers with $St_r = 30$ and $\lambda_r = 2$ (resp. $\lambda_r = 5$) with a volume fraction $\Phi_v \simeq 1.6 \cdot 10^{-4}$ (resp. $\Phi_v \simeq 6.2 \cdot 10^{-4}$) indicate that the feedback force exerted from the particles to the surrounding fluid does not affect significantly the fluid motion with to respect to the $one-way$ coupling case : This is due mainly to the fact that the values of force exerted by the fibers onto the fluid are rather small, and associated to rather small peaks of concentration near the wall.
The fiber motion is influenced from a macroscopical point of view, only in the wall-normal concentration: the fibers in dilute regime seem to concentrate more than the fibers in semi-dilute regime, regardless of their aspect ratio. In this way there is no zone in the flow field that is particularly affected by the feedback force from the fibers.
Finally we observe a slight change in the deformation angle $\langle\alpha\rangle$ in the near-wall region between the $one-way$ and the $two-way$ cases. In particular higher deformation is observed for the $two-way$ coupled fibers, regardless of the aspect ratio. In the center of the channel, instead, no modifications in the statistics of $\langle\alpha\rangle$ is observed.
Future developments to be investigated in the semi-dilute regime are related to the introduction of turbulence modulation by flexible fibers at higher volume fractions and a complete coupling between the phases that includes also the angular angular momentum exchange by the fiber on the surrounding fluid and the effect of bending stiffness on the fiber deformation dynamics and the dependence of fiber deformation. In particular, these modifications will allow a more realistic representation of fiber bending dynamics and hopefully provide information about the drag reduction in pipeline.

6

Appendix

Wall Rebound

The fibers' rebound on the wall is totally elastic: in other words, the linear momentum in the wall-normal direction changes in sign when the fiber touches the wall, while the other linear and the angular momenta are maintained. We use the same approach developed by [5] and Benvenuto [6]: the collision with the lower wall, for example, occurs when it is overlapped by the fibers' lowest point as shown in Fig.[6.1]:

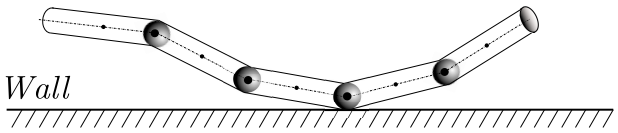

FIGURE 6.1 – Elastic rebound on the wall.

Poisson Equation for a Versor

Considering a versor $\mathbf{o}$ in an absolute frame of reference, and defined by director cosine angles. Those versors can be write as:

$$\mathbf{o} = \cos\alpha_1 \mathbf{e}_x + \cos\alpha_2 \mathbf{e}_y + \cos\alpha_3 \mathbf{e}_z. \tag{6.1}$$

Those versor rotate with an angular velocity $\boldsymbol{\omega}$ respect to the center of the absolute frame of reference:

$$\boldsymbol{\omega} = \dot{\alpha}_1 \mathbf{e}_x + \dot{\alpha}_2 \mathbf{e}_y + \dot{\alpha}_3 \mathbf{e}_z. \tag{6.2}$$

The time derivative of the versor $\mathbf{o}$ is:

$$\frac{d\mathbf{o}}{dt} = \boldsymbol{\omega} \times \mathbf{o}. \tag{6.3}$$

Proof. In the absolute frame the time derivative of the versor is:

$$\frac{d\mathbf{o}}{dt} = o_x \frac{d\mathbf{e}_x}{dt} + o_y \frac{d\mathbf{e}_y}{dt} + o_z \frac{d\mathbf{e}_z}{dt}. \tag{6.4}$$

For a simpler demonstration it is easier to consider a sigle rotation and to compose them at the end.

Rotation along $\mathbf{e}_x$ direction. Considering a local frame of reference that rotates of α_1, the change of coordinates is:

$$\begin{aligned} &\begin{Bmatrix} \mathbf{e}_{x_{\alpha_1}} \\ \mathbf{e}_{y_{\alpha_1}} \\ \mathbf{e}_{z_{\alpha_1}} \end{Bmatrix} \iff \begin{Bmatrix} \mathbf{e}_x \\ \mathbf{e}_y \\ \mathbf{e}_z \end{Bmatrix} \implies \\ \implies &\begin{Bmatrix} \mathbf{e}_{x_{\alpha_1}} \\ \mathbf{e}_{y_{\alpha_1}} \\ \mathbf{e}_{z_{\alpha_1}} \end{Bmatrix} = \begin{bmatrix} 1 & 0 & 0 \\ 0 & \cos\alpha_1 & \sin\alpha_1 \\ 0 & -\sin\alpha_1 & \cos\alpha_1 \end{bmatrix} \begin{Bmatrix} \mathbf{e}_x \\ \mathbf{e}_y \\ \mathbf{e}_z \end{Bmatrix}. \end{aligned} \tag{6.5}$$

So:

$$\begin{aligned} \frac{d\mathbf{o}_x}{dt} =& o_{x,\alpha_1} \frac{d\mathbf{e}_{x_{\alpha_1}}}{dt} + o_{y,\alpha_1} \frac{d\mathbf{e}_{y_{\alpha_1}}}{dt} + o_{z,\alpha_1} \frac{d\mathbf{e}_{z_{\alpha_1}}}{dt} = \\ =& o_{y,\alpha_1} \frac{d\mathbf{e}_{y_{\alpha_1}}}{dt} + o_{z,\alpha_1} \frac{d\mathbf{e}_{z_{\alpha_1}}}{dt} = \\ =& \begin{vmatrix} \mathbf{e}_x & \mathbf{e}_y & \mathbf{e}_z \\ \dot{\alpha}_1 & 0 & 0 \\ o_x & o_y & o_z \end{vmatrix} = \boldsymbol{\omega} \times \mathbf{o}|_{\alpha_1 \ Rotation}, \end{aligned} \tag{6.6}$$

where:

$$\dot{\alpha}_1 = \frac{d\alpha_1}{dt}.$$

Rotation along $\mathbf{e}_y$ direction. Considering a local frame of reference that rotates of α_2, the change of coordinates is:

$$\begin{aligned} &\begin{Bmatrix} \mathbf{e}_{x_{\alpha_2}} \\ \mathbf{e}_{y_{\alpha_2}} \\ \mathbf{e}_{z_{\alpha_2}} \end{Bmatrix} \iff \begin{Bmatrix} \mathbf{e}_x \\ \mathbf{e}_y \\ \mathbf{e}_z \end{Bmatrix} \implies \\ \implies &\begin{Bmatrix} \mathbf{e}_{x_{\alpha_2}} \\ \mathbf{e}_{y_{\alpha_2}} \\ \mathbf{e}_{z_{\alpha_2}} \end{Bmatrix} = \begin{bmatrix} \cos\alpha_2 & 0 & -\sin\alpha_2 \\ 0 & 1 & 0 \\ \sin\alpha_2 & 0 & \cos\alpha_2 \end{bmatrix} \begin{Bmatrix} \mathbf{e}_x \\ \mathbf{e}_y \\ \mathbf{e}_z \end{Bmatrix}. \end{aligned} \tag{6.7}$$

So:

$$\begin{aligned} \frac{d\mathbf{o}_y}{dt} =& o_{x,\alpha_2} \frac{d\mathbf{e}_{x_{\alpha_2}}}{dt} + o_{y,\alpha_2} \frac{d\mathbf{e}_{y_{\alpha_2}}}{dt} + o_{z,\alpha_2} \frac{d\mathbf{e}_{z_{\alpha_2}}}{dt} = \\ =& o_{x,\alpha_2} \frac{d\mathbf{e}_{x_{\alpha_2}}}{dt} + o_{z,\alpha_2} \frac{d\mathbf{e}_{z_{\alpha_2}}}{dt} = \\ =& \begin{vmatrix} \mathbf{e}_x & \mathbf{e}_y & \mathbf{e}_z \\ 0 & \dot{\alpha}_2 & 0 \\ o_x & o_y & o_z \end{vmatrix} = \boldsymbol{\omega} \times \mathbf{o}|_{\alpha_2 \ Rotation}, \end{aligned} \tag{6.8}$$

where:

$$\dot{\alpha}_2 = \frac{d\alpha_2}{dt}.$$

Rotation along $\mathbf{e}_z$ direction. Considering a local frame of reference that rotates of α_3, the change of coordinates is:

$$\begin{Bmatrix} \mathbf{e}_{x_{\alpha_3}} \\ \mathbf{e}_{y_{\alpha_3}} \\ \mathbf{e}_{z_{\alpha_3}} \end{Bmatrix} \iff \begin{Bmatrix} \mathbf{e}_x \\ \mathbf{e}_y \\ \mathbf{e}_z \end{Bmatrix} \implies$$

$$\implies \begin{Bmatrix} \mathbf{e}_{x_{\alpha_3}} \\ \mathbf{e}_{y_{\alpha_3}} \\ \mathbf{e}_{z_{\alpha_3}} \end{Bmatrix} = \begin{bmatrix} \cos\alpha_3 & \sin\alpha_3 & 0 \\ -\sin\alpha_3 & \cos\alpha_3 & 0 \\ 0 & 0 & 1 \end{bmatrix} \begin{Bmatrix} \mathbf{e}_x \\ \mathbf{e}_y \\ \mathbf{e}_z \end{Bmatrix}. \tag{6.9}$$

So:

$$\begin{aligned} \frac{d\mathbf{o}_z}{dt} =& o_{x,\alpha_3} \frac{d\mathbf{e}_{x_{\alpha_3}}}{dt} + o_{y,\alpha_3} \frac{d\mathbf{e}_{y_{\alpha_3}}}{dt} + o_{z,\alpha_3} \frac{d\mathbf{e}_{x_{\alpha_3}}}{dt} = \\ =& o_{x,\alpha_3} \frac{d\mathbf{e}_{x_{\alpha_3}}}{dt} + o_{y,\alpha_3} \frac{d\mathbf{e}_{y_{\alpha_3}}}{dt} = \\ =& \begin{vmatrix} \mathbf{e}_x & \mathbf{e}_y & \mathbf{e}_z \\ 0 & 0 & \dot{\alpha}_3 \\ o_x & o_y & o_z \end{vmatrix} = \boldsymbol{\omega} \times \mathbf{o}|_{\alpha_3 \ Rotation}, \end{aligned} \tag{6.10}$$

where:

$$\dot{\alpha}_3 = \frac{d\alpha_3}{dt}.$$

So the total equation for the time derivative of $\mathbf{o}$ considering the rotation in every direction is:

$$\frac{d\mathbf{o}}{dt} = \boldsymbol{\omega} \times \mathbf{o}. \tag{6.11}$$

Inertia Tensor

The angular momentum $\mathbf{L}$ for a system of point particles $r \in [1, N]$, with mass m_r, position $\mathbf{p}_r$ and angular velocity $\boldsymbol{\omega}_r$ is:

$$\mathbf{L} = \sum_{r=1}^{N} \mathbf{p}_r \times m_r \left(\boldsymbol{\omega}_r \times \mathbf{p}_r \right). \tag{6.12}$$

If, instead of a system of point particles, we have a rigid continue body, the sum become an integral over the mass of the body:

$$\mathbf{L} = \int_m \mathbf{p} \times (\boldsymbol{\omega} \times \mathbf{p}) \, dm = \int_m \left[(\mathbf{p} \cdot \mathbf{p}) \, \boldsymbol{\omega} - (\mathbf{p} \cdot \boldsymbol{\omega}) \, \mathbf{p} \right] dm. \tag{6.13}$$

If we decompose the position and the orientation in every component:

$$\begin{cases} \mathbf{p} = p_x \mathbf{e}_x + p_y \mathbf{e}_y + p_z \mathbf{e}_z, \\ \boldsymbol{\omega} = \omega_x \mathbf{e}_x + \omega_y \mathbf{e}_y + \omega_z \mathbf{e}_y. \end{cases}$$

It is possible to re-write the equation of the angular momentum component by component:

$$\begin{aligned} \mathbf{L} = & \left[\omega_x \int_m \left(p_y^2 + p_z^2 \right) dm - \omega_y \int_m p_x p_y dm - \omega_z \int_m p_x p_z dm \right] \mathbf{e}_x + \\ & + \left[\omega_y \int_m \left(p_x^2 + p_z^2 \right) dm - \omega_x \int_m p_x p_y dm - \omega_z \int_m p_y p_z dm \right] \mathbf{e}_y + \\ & + \left[\omega_z \int_m \left(p_x^2 + p_y^2 \right) dm - \omega_x \int_m p_x p_z dm - \omega_y \int_m p_y p_z dm \right] \mathbf{e}_z = \\ & = \left(J_{xx} \omega_x + J_{xy} \omega_y + J_{xz} \omega_z \right) \mathbf{e}_x + \\ & + \left(J_{yx} \omega_x + J_{yy} \omega_y + J_{yz} \omega_z \right) \mathbf{e}_y + \\ & + \left(J_{zx} \omega_x + J_{zy} \omega_y + J_{zz} \omega_z \right) \mathbf{e}_z = \\ & = \begin{Bmatrix} L_x \\ L_y \\ L_z \end{Bmatrix} = \underbrace{\begin{bmatrix} J_{xx} & J_{xy} & J_{xz} \\ J_{yx} & J_{yy} & J_{yz} \\ J_{zx} & J_{zy} & J_{zz} \end{bmatrix}}_{Inertia\ tensor\ \bar{\bar{\mathbf{J}}}} \begin{Bmatrix} \omega_x \\ \omega_y \\ \omega_z \end{Bmatrix}, \end{aligned} \tag{6.14}$$

where the components of the inertia tensor are:

$$\begin{aligned} J_{ii} &= \int_m \left(p_j^2 + p_k^2 \right) dm \quad if \quad i \neq j,\ j \neq k,\ i \neq k \\ J_{ij} &= \int_m p_i p_j dm \quad if \quad i \neq j \end{aligned}$$

Inertia of a Rotating Cylinder

Considering a cylinder with radius a, semi-length l, density ρ_p, oriented like $\mathbf{o}$ and chosing the center of the frame of reference at the center of the cylinder $z \parallel \mathbf{o}$ Fig.[6.2]:
In cylindrical coordinates:

$$\begin{cases} p_x = r \cos\theta, \\ p_y = r \sin\theta, \\ p_z = z. \end{cases} \tag{6.15}$$

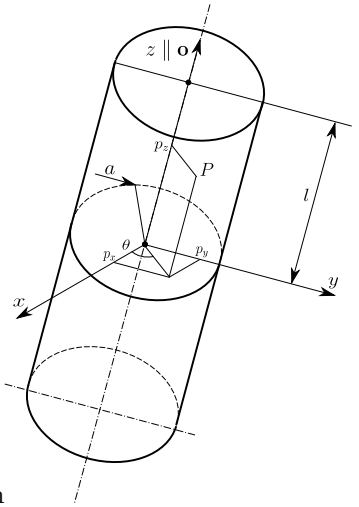

cmcm

FIGURE 6.2 – Inertia tensor of a rotating cylinder.

The components of the ineria tensor are:

$$
\begin{aligned}
J_{xx} &= \int_m \left(p_y^2 + p_z^2\right) dm = \rho_p \int_V \left(p_y^2 + p_z^2\right) dV = \\
&= \rho_p \int_{-l}^{l} \int_0^{2\pi} \int_0^a \left(r^2 \sin^2\theta + z^2\right) (r dr)\, d\theta dz = \\
&= \rho_p 2l \frac{a^4}{4} \frac{2\pi}{2} + \rho_p \frac{2l^3 \pi a^2}{12} = \frac{1}{4} \underbrace{\left(\pi 2 l a^2\right)}_{m} \left(a^2 + \frac{l^2}{3}\right) = \\
&= \frac{m}{4} \left(a^2 + \frac{l^2}{3}\right), \\
J_{yy} &= \int_m \left(p_x^2 + p_z^2\right) dm = \rho_p \int_V \left(p_x^2 + p_z^2\right) dV = \\
&= \rho_p \int_{-l}^{l} \int_0^{2\pi} \int_0^a \left(r^2 \cos^2\theta + z^2\right) (r dr)\, d\theta dz = \\
&= \rho_p 2l \frac{a^4}{4} \frac{2\pi}{2} + \rho_p \frac{2l^3 \pi a^2}{12} = \frac{1}{4} \underbrace{\left(\pi 2 l a^2\right)}_{m} \left(a^2 + \frac{l^2}{3}\right) = \\
&= \frac{m}{4} \left(a^2 + \frac{l^2}{3}\right), \\
J_{zz} &= \int_m \left(p_x^2 + p_y^2\right) dm = \rho_p \int_V \left(p_x^2 + p_y^2\right) dV = \\
&= \rho_p \int_{-l}^{l} \int_0^{2\pi} \int_0^a \left(r^2 \sin^2\theta + r^2 \cos^2\theta\right) (r dr)\, d\theta dz = \\
&= \rho_p \int_{-l}^{l} dz \int_0^{2\pi} d\theta \int_0^a r^3 dr = \rho_p 2l \frac{a^4}{4} 2\pi = \frac{1}{4} \underbrace{\left(\pi 2 l a^2\right)}_{m} a^2,
\end{aligned}
\tag{6.16}
$$

$$
\begin{aligned}
J_{xy} = J_{yx} = \int_m p_x p_y dm = \rho_p \int_V p_x p_y dV = \\
= \rho_p \int_{-l}^{l} \int_0^{2\pi} \int_0^a r^2 \sin\theta \cos\theta \, (r dr) \, d\theta dz = \\
= \rho_p \int_{-l}^{l} dz \int_0^{2\pi} \sin\theta \cos\theta d\theta \underbrace{\int_0^a r^3 r dr}_{=0} = 0, \\
J_{xz} = J_{zx} = \int_m p_x p_z dm = \rho_p \int_V p_x p_z dV = \\
= \rho_p \int_{-l}^{l} \int_0^{2\pi} \int_0^a r^2 \sin\theta z \, (r dr) \, d\theta dz = \\
= \rho_p \int_{-l}^{l} z dz \int_0^{2\pi} \sin\theta d\theta \underbrace{\int_0^a r^3 r dr}_{=0} = 0, \\
J_{yz} = J_{zy} = \int_m p_y p_z dm = \rho_p \int_V p_y p_z dV \\
= \rho_p \int_{-l}^{l} \int_0^{2\pi} \int_0^a r^2 \cos\theta z \, (r dr) \, d\theta dz = \\
= \rho_p \int_{-l}^{l} z dz \int_0^{2\pi} \cos\theta d\theta \underbrace{\int_0^a r^3 r dr}_{=0} = 0,
\end{aligned}
\tag{6.17}
$$

where, of course:

$$dm = \rho_p dV.$$

So the inertia tensor for a cylindr in the local frame of reference is:

$$
\bar{\bar{\mathbf{J}}} = \begin{bmatrix} \frac{m}{12}\left(3a^2 + l^2\right) & 0 & 0 \\ 0 & \frac{m}{12}\left(3a^2 + l^2\right) & 0 \\ 0 & 0 & \frac{m}{2}a^2. \end{bmatrix}
\tag{6.18}
$$

Block-Tridiagonal Matrices Resolution

A form which is encountered frequently, especially in the numerical solution of partial differential equations and integral equations, is the so-called block-

tridiagonal matrix:

$$\bar{\bar{\mathbf{G}}} = \begin{bmatrix} \bar{\bar{\mathcal{A}}}_i & \bar{\bar{\mathcal{C}}}_1 & & & & & & \\ \bar{\bar{\mathbf{B}}}_2 & \bar{\bar{\mathcal{A}}}_2 & \bar{\bar{\mathcal{C}}}_2 & & & & & \\ & \cdots & \cdots & \cdots & & & & \\ & & \cdots & \cdots & \cdots & & & \\ & & & \bar{\bar{\mathbf{B}}}_i & \bar{\bar{\mathcal{A}}}_i & \bar{\bar{\mathbf{C}}}_i & & \\ & & & & \cdots & \cdots & \cdots & \\ & & & & & \cdots & \cdots & \cdots \\ & & & & & & \bar{\bar{\mathbf{B}}}_n & \bar{\bar{\mathcal{A}}}_n. \end{bmatrix} \tag{6.19}$$

Here, each of the $\bar{\bar{\mathcal{A}}}_i$, $\bar{\bar{\mathbf{B}}}_i$ and $\bar{\bar{\mathcal{C}}}_i$ represents a square matrix, of order s_i.

A system with coefficient matrix of the form above may be solved by a procedure formally analogous to the previous factorization of a Jacobi matrix. Thus, let the system be:

$$\bar{\bar{\mathbf{G}}}\mathbf{x} = \mathbf{f}, \tag{6.20}$$

where now:

$$\mathbf{x} = \begin{Bmatrix} \mathbf{x}^{(1)} \\ \mathbf{x}^{(2)} \\ \cdots \\ \mathbf{x}^{(n)} \end{Bmatrix}, \qquad \mathbf{f} = \begin{Bmatrix} \mathbf{f}^{(1)} \\ \mathbf{f}^{(2)} \\ \cdots \\ \mathbf{f}^{(n)} \end{Bmatrix},$$

and each $\mathbf{x}^{(i)}$ and $\mathbf{f}^{(i)}$ are s_i-component column vectors. That is, the components of the vector $\mathbf{x}$ are grouped into subsets, $\mathbf{x}^{(i)}$, and these subsets are to be "eliminated", as in the Gaussian procedure, a group at a time. Thus, the method to be described is a special case of more general methods known as group- or block-elimination.

We seek a factorization of the form:

$$\bar{\bar{\mathbf{G}}} = \bar{\bar{\mathbf{L}}}\bar{\bar{\mathbf{U}}} = \begin{bmatrix} \bar{\bar{\mathbf{G}}}_1 & & & & \\ \bar{\bar{\mathbf{B}}}_2 & \bar{\bar{\mathbf{G}}}_2 & & & \\ & \cdots & \cdots & & \\ & & \cdots & \cdots & \\ & & & \bar{\bar{\mathbf{B}}}_n & \bar{\bar{\mathbf{G}}}_n \end{bmatrix} \begin{bmatrix} \bar{\bar{\boldsymbol{\delta}}} & \bar{\bar{\boldsymbol{\Gamma}}}_1 & & & \\ & \bar{\bar{\boldsymbol{\delta}}} & \bar{\bar{\boldsymbol{\Gamma}}}_2 & & \\ & & \cdots & \cdots & \\ & & & \cdots & \cdots \\ & & & & \bar{\bar{\boldsymbol{\delta}}} \end{bmatrix}, \tag{6.21}$$

where:
$\bar{\bar{\boldsymbol{\delta}}}$ is Identity matrices of order m_i;
$\bar{\bar{\mathbf{G}}}_i$ and $\bar{\bar{\boldsymbol{\Gamma}}}_i$ are square matrices of order m_i. Proceeding formally, we find

that:

$$\begin{aligned}
&\bar{\bar{\mathbf{G}}}_1 = \bar{\bar{\boldsymbol{\mathcal{A}}}}_1, \\
&\bar{\bar{\boldsymbol{\Gamma}}}_1 = \bar{\bar{\boldsymbol{\mathcal{A}}}}_1^{-1} \bar{\bar{\mathcal{C}}}_1, \\
&\bar{\bar{\mathbf{G}}}_i = \bar{\bar{\boldsymbol{\mathcal{A}}}}_i - \bar{\bar{\mathbf{B}}}_i \bar{\bar{\boldsymbol{\Gamma}}}_{i-1} \qquad if \quad i \in [2, n]\,, \\
&\bar{\bar{\boldsymbol{\Gamma}}}_i = \bar{\bar{\mathbf{A}}}_i^{-1} \bar{\bar{\mathcal{C}}}_i \qquad if \quad i \in [2, n-1]\,.
\end{aligned} \tag{6.22}$$

From the definitions of the matrices involved, it is clear that each $\bar{\bar{\boldsymbol{\Gamma}}}_i$ is rectangular of the indicated order and that the product $\bar{\bar{\mathbf{B}}}_i \bar{\bar{\boldsymbol{\Gamma}}}_{i-1}$ and hence $\bar{\bar{\mathbf{G}}}_i$ is square of order s_i The system above is now equivalent to:

$$\begin{aligned}
&\bar{\bar{\mathbf{L}}}\mathbf{y} = \mathbf{f}, \\
&\bar{\bar{\mathbf{U}}}\mathbf{x} = \mathbf{y}.
\end{aligned} \tag{6.23}$$

We thus obtain:

$$\begin{aligned}
&\mathbf{y}^{(1)} = \bar{\bar{\mathbf{G}}}_1^{-1} \mathbf{f}^{(1)}, \\
&\mathbf{y}^{(i)} = \bar{\bar{\mathbf{G}}}_i^{-1} \left[\mathbf{f}^{(1)} - \bar{\bar{\mathbf{B}}}_i \mathbf{y}^{(i-1)} \right] \qquad if \quad i \in [2, n]\,, \\
&\mathbf{x}^{(n)} = \mathbf{y}^{(n)}, \\
&\mathbf{x}^{(i)} = \mathbf{y}^{(i)} - \bar{\bar{\boldsymbol{\Gamma}}}_i \mathbf{x}^{(i+1)} \qquad if \quad i \in [n-1, 1]\,.
\end{aligned} \tag{6.24}$$

Reynolds number analysis

The Reynolds number for the segment is defined as in eq.[2.54], so the term $v_{\perp;r}$ can be analyzed starting from:

$$\left(\bar{\bar{\boldsymbol{\delta}}} - \mathbf{o}_r \mathbf{o}_r^T\right) \underbrace{(\mathbf{u}_r - \mathbf{v}_r)}_{\Delta \mathbf{V}_r} = \begin{Bmatrix} \Delta V_{x;r} - o_{x;r} \mathcal{X} \\ \Delta V_{y;r} - o_{y;r} \mathcal{X} \\ \Delta V_{z;r} - o_{z;r} \mathcal{X} \end{Bmatrix}; \qquad \mathcal{X} = \sum_{i=1}^{3} o_{i;r} \Delta V_{i;r}. \tag{6.25}$$

So, the modulus is:

$$\left| \left(\bar{\bar{\boldsymbol{\delta}}} - \mathbf{o}_r \mathbf{o}_i^T\right) \Delta \mathbf{V}_r \right| = \sqrt{\Delta V_{x,r}^2 + \Delta V_{y,r}^2 + \Delta V_{z,r}^2 - \mathcal{X}^2}. \tag{6.26}$$

Now the modulus of the cross product between $\mathbf{o}_r$ and $\Delta \mathbf{V}_r$ is:

$$|\mathbf{o}_r \times \Delta \mathbf{V}_r| = \sqrt{\Delta V_{x,r}^2 + \Delta V_{y,r}^2 + \Delta V_{z,r}^2 - \mathcal{X}^2}. \tag{6.27}$$

So it means:

$$\left| \left(\bar{\bar{\boldsymbol{\delta}}} - \mathbf{o}_r \mathbf{o}_r^T\right) (\mathbf{u}_r - \mathbf{v}_r) \right| = |\mathbf{o}_r \times (\mathbf{u}_r - \mathbf{v}_r)|\,.$$

In other words:

$$\begin{cases}
if \quad \mathbf{o}_r \perp (\mathbf{u}_r - \mathbf{v}_r) \quad \Longrightarrow \quad Re_{p;r} = \dfrac{2\rho a}{\mu} |\mathbf{u}_r - \mathbf{v}_r|\,, \\
if \quad \mathbf{o}_r \parallel (\mathbf{u}_r - \mathbf{v}_r) \quad \Longrightarrow \quad Re_{p;r} = 0.
\end{cases}$$

Drag Torques for Finite $Re_{p;r}$

The expression for the drag torques acting on the segment r, $\mathbf{Tor}_r$, can be derived from Lindström and Uesaka (2008)

$$\mathbf{Tor}_r = \int_{-l}^{l} d\mathbf{T}_r = \int_{-l}^{l} z\mathbf{o}_r \times d\mathbf{F}_r^D, \tag{6.28}$$

where: z in this case is the coordinate along the axial direction of the segment.
The infinitesimal force $d\mathbf{F}_r$ is:

$$\mathbf{F}_r^D = C_D \rho a \left(2\lambda_r a_r\right) \left[\left(\overline{\overline{\boldsymbol{\delta}}} - \mathbf{o}_r\mathbf{o}_r^T\right)\left(\mathbf{u}_r - \mathbf{v}_r\right)\right] \implies$$
$$\implies d\mathbf{F}_r^D = C_D \rho a \left[\left(\overline{\overline{\boldsymbol{\delta}}} - \mathbf{o}_r\mathbf{o}_r^T\right)\left(\mathbf{u}_r - \mathbf{v}_r\right)\right] dz,$$

where, since the length of the fiber is small,

$$\mathbf{u}_r - \mathbf{v}_r = \underbrace{\mathbf{u}_{z,r} - \mathbf{v}_{z,r}}_{\simeq 0} + z\left(\boldsymbol{\Omega}_r - \boldsymbol{\omega}_r\right) \times \mathbf{o}_r + z\dot{\overline{\overline{\gamma}}}_r \cdot \mathbf{o}_r.$$

So:

$$d\mathbf{F}_r^D = C_D \rho a \left(\overline{\overline{\boldsymbol{\delta}}} - \mathbf{o}_r\mathbf{o}_r^T\right) \left[z\left(\boldsymbol{\Omega}_r - \boldsymbol{\omega}_r\right) \times \mathbf{o}_r + z\dot{\overline{\overline{\gamma}}}_r \cdot \mathbf{o}_r\right] dz. \tag{6.29}$$

The drag torques are:

$$\begin{aligned}
\mathbf{Tor}_r = &\int_{-l}^{l} z\mathbf{o}_r \times C_D \rho a \left(\overline{\overline{\boldsymbol{\delta}}} - \mathbf{o}_r\mathbf{o}_r^T\right) \\
&\left[z\left(\boldsymbol{\Omega}_r - \boldsymbol{\omega}_r\right) \times \mathbf{o}_r + z\dot{\overline{\overline{\gamma}}}_r \cdot \mathbf{o}_r\right] dz = \\
=&C_D \rho a \int_{-l}^{l} z^2 \mathbf{o}_r \times \left(\overline{\overline{\boldsymbol{\delta}}} - \mathbf{o}_r\mathbf{o}_r^T\right) \\
&\left[\left(\boldsymbol{\Omega}_r - \boldsymbol{\omega}_r\right) \times \mathbf{o}_r + \dot{\overline{\overline{\gamma}}}_r \cdot \mathbf{o}_r\right] dz = \\
=&\frac{2}{3} C_D \rho \lambda_r^3 a^4 \mathbf{o}_r \times \left(\overline{\overline{\boldsymbol{\delta}}} - \mathbf{o}_r\mathbf{o}_r^T\right) \left[\left(\boldsymbol{\Omega}_r - \boldsymbol{\omega}_r\right) \times \mathbf{o}_r + \dot{\overline{\overline{\gamma}}}_r \cdot \mathbf{o}_r\right] = \\
=&\frac{2}{3} C_D \rho \lambda_r^3 a^4 \left[\underbrace{\mathbf{o}_r \times \left(\overline{\overline{\boldsymbol{\delta}}} - \mathbf{o}_r\mathbf{o}_r^T\right)\left(\boldsymbol{\Omega}_r - \boldsymbol{\omega}_r\right) \times \mathbf{o}_r}_{1)}\right. \\
&\left. + \underbrace{\mathbf{o}_r \times \left(\overline{\overline{\boldsymbol{\delta}}} - \mathbf{o}_r\mathbf{o}_r^T\right) \dot{\overline{\overline{\gamma}}}_r \cdot \mathbf{o}_r}_{2)}\right]
\end{aligned} \tag{6.30}$$

1.

$$\begin{aligned}
&\mathbf{o}_r \times \left(\overline{\overline{\boldsymbol{\delta}}} - \mathbf{o}_r\mathbf{o}_r^T\right)(\boldsymbol{\Omega}_r - \boldsymbol{\omega}_r) \times \mathbf{o}_r = \\
&= -\mathbf{o}_r \times \left(\overline{\overline{\boldsymbol{\delta}}} - \mathbf{o}_r\mathbf{o}_r^T\right)[\mathbf{o}_r \times (\boldsymbol{\Omega}_r - \boldsymbol{\omega}_r)] = \\
&= \underbrace{-\mathbf{o}_r \times \overline{\overline{\boldsymbol{\delta}}}\,[\mathbf{o}_r \times (\boldsymbol{\Omega}_r - \boldsymbol{\omega}_r)]}_{a)} \underbrace{-\mathbf{o}_r \times \left(\mathbf{o}_r\mathbf{o}_r^T\right)[\mathbf{o}_r \times (\boldsymbol{\Omega}_r - \boldsymbol{\omega}_r)]}_{b)}
\end{aligned} \tag{6.31}$$

(a)

$$\begin{aligned}
&-\mathbf{o}_r \times \overline{\overline{\boldsymbol{\delta}}}\,[\mathbf{o}_r \times (\boldsymbol{\Omega}_r - \boldsymbol{\omega}_r)] = \\
&= -\mathbf{o}_r \times [\mathbf{o}_r \times (\boldsymbol{\Omega}_r - \boldsymbol{\omega}_r)] = \\
&= -\mathbf{o}_r\,[(\boldsymbol{\Omega}_r - \boldsymbol{\omega}_r) \cdot \mathbf{o}_r] + (\boldsymbol{\Omega}_r - \boldsymbol{\omega}_r)(\mathbf{o}_r \cdot \mathbf{o}_r) = \\
&= -\mathbf{o}_r\,[\mathbf{o}_r \cdot (\boldsymbol{\Omega}_r - \boldsymbol{\omega}_r)] + \overline{\overline{\boldsymbol{\delta}}}\,(\boldsymbol{\Omega}_r - \boldsymbol{\omega}_r) = \\
&= \left(\overline{\overline{\boldsymbol{\delta}}} - \mathbf{o}_r\mathbf{o}_r^T\right)(\boldsymbol{\Omega}_r - \boldsymbol{\omega}_r)
\end{aligned} \tag{6.32}$$

(b)

$$\begin{aligned}
&-\mathbf{o}_r \times \left(\mathbf{o}_r\mathbf{o}_r^T\right)[\mathbf{o}_r \times (\boldsymbol{\Omega}_r - \boldsymbol{\omega}_r)]\,|_i = \\
&= -\mathbf{o}_r \times [o_{k,r}o_{l,r}\varepsilon_{lmn}o_{m,r}\,(\Omega_{n,r} - \omega_{n,r})] = 0.
\end{aligned} \tag{6.33}$$

2.

$$\begin{aligned}
&\mathbf{o}_r \times \left(\overline{\overline{\boldsymbol{\delta}}} - \mathbf{o}_r\mathbf{o}_r^T\right)\dot{\overline{\overline{\boldsymbol{\gamma}}}}_r \cdot \mathbf{o}_r = \\
&= \underbrace{\mathbf{o}_r \times \left[\overline{\overline{\boldsymbol{\delta}}}\left(\dot{\overline{\overline{\boldsymbol{\gamma}}}}_r \cdot \mathbf{o}_r\right)\right]}_{a)} \underbrace{-\mathbf{o}_r \times \left[\left(\mathbf{o}_r\mathbf{o}_r^T\right)\left(\dot{\overline{\overline{\boldsymbol{\gamma}}}}_r \cdot \mathbf{o}_r\right)\right]}_{b)}.
\end{aligned} \tag{6.34}$$

(a)

$$\mathbf{o}_r \times \left[\overline{\overline{\boldsymbol{\delta}}}\left(\dot{\overline{\overline{\boldsymbol{\gamma}}}}_r \cdot \mathbf{o}_r\right)\right] = \mathbf{o}_r \times \left(\dot{\overline{\overline{\boldsymbol{\gamma}}}}_r \cdot \mathbf{o}_r\right) = -\left(\dot{\overline{\overline{\boldsymbol{\gamma}}}}_r \cdot \mathbf{o}_r\right) \times \mathbf{o}_r. \tag{6.35}$$

(b)

$$\begin{aligned}
&-\mathbf{o}_r \times \left[\left(\mathbf{o}_r\mathbf{o}_r^T\right)\left(\dot{\overline{\overline{\boldsymbol{\gamma}}}}_r \cdot \mathbf{o}_r\right)\right]\,|_i = \\
&= -\mathbf{o}_r \times (o_{k,r}o_{l,r}\dot{\gamma}_{lm,r}o_{m,r}) = 0.
\end{aligned} \tag{6.36}$$

So the total drag torques due to the vorticity rate and to the strain rate is:

$$\begin{aligned}
\mathbf{Tor}_r =& \frac{2}{3}C_D\rho\lambda_r^3 a^4\left[\left(\overline{\overline{\boldsymbol{\delta}}} - \mathbf{o}_r\mathbf{o}_r^T\right)(\boldsymbol{\Omega}_r - \boldsymbol{\omega}_r) - \left(\dot{\overline{\overline{\boldsymbol{\gamma}}}}_r \cdot \mathbf{o}_r\right) \times \mathbf{o}_r\right] = \\
=& \mathbf{T}_r^D + \mathbf{H}_r^D.
\end{aligned} \tag{6.37}$$

Fiber Equations in Non-Dimensional Form

The eq.[2.69]-[6.42] above are non-dimensionalized throught these terms:

$$u_\tau \left[\frac{m}{s}\right], \qquad \rho \left[\frac{kg}{m^3}\right], \qquad \nu \left[\frac{m^2}{s}\right]$$

So the terms involved in the system of eqs.[2.69]-[6.42], are re-written in non-dimensional form using the apex $^+$ (differently from the flow field with the apex $^-$), in this way:

$$\mathbf{u}_r^+ = \frac{\mathbf{u}_r}{u_\tau} \quad \mathbf{v}_r^+ = \frac{\mathbf{v}_r}{u_\tau} \quad \boldsymbol{\omega}_r^+ = \frac{\boldsymbol{\omega}_r \mu}{\rho u_\tau^2} \quad t^+ = \frac{t u_\tau^2 \rho}{\mu}$$
$$a^+ = \frac{a \rho u_\tau}{\mu} \quad \rho_p^+ = \frac{\rho_p}{\rho} \quad v_{\perp;r}^+ = \frac{v_{\perp;r}}{u_\tau} \quad \boldsymbol{\Omega}_r^+ = \frac{\boldsymbol{\Omega}_r \mu}{\rho u_\tau^2}$$
$$E_Y = E_Y^+ u_\tau^2 \rho \quad \mathbf{X}_r^+ = \frac{\mathbf{X}_r \rho}{\mu^2}.$$

So the system of equations [2.69]-[2.73] in non-dimensional form is:

$$\frac{d\mathbf{v}_r^+}{dt^+} = \bar{\bar{\mathbf{A}}}_r^{+'} \left(\mathbf{u}_r^+ - \mathbf{v}_r^+\right) + \frac{1}{2\pi\lambda_r \left(a^+\right)^3 \rho_p^+} \left(\mathbf{X}_{r+1}^+ - \mathbf{X}_r^+\right), \tag{6.38}$$

$$\bar{\bar{\mathbf{J}}}_r^+ \frac{\partial \boldsymbol{\omega}_r^+}{\partial t^+} + \dot{\bar{\bar{\mathbf{J}}}}_r^+ \boldsymbol{\omega}_r^+ = \bar{\bar{\mathbf{C}}}_r^{+'} \left(\boldsymbol{\Omega}_r^+ - \boldsymbol{\omega}_r^+\right) + H_{i,r}^{+'} + \\ + \frac{E_Y^+}{8\lambda_r^2 \left(a^+\right)^2 \rho_p^+} \left(\alpha_{r+1}^b \mathbf{e}_r^b - \alpha_r^b \mathbf{e}_{r+1}^b\right) + \\ + \frac{1}{\pi \left(a^+\right)^4 \rho_r^+} \mathbf{o}_r \times \left(\mathbf{X}_{r+1}^+ + \mathbf{X}_r^+\right), \tag{6.39}$$

$$\mathbf{v}_r^+ - \mathbf{v}_{r+1}^+ + \lambda_r a^+ \left(\boldsymbol{\omega}_r^+ \times \mathbf{o}_r + \boldsymbol{\omega}_{r+1}^+ \times \mathbf{o}_{r+1}\right) = 0, \tag{6.40}$$

$$\frac{d\mathbf{p}_r^+}{dt^+} = \mathbf{v}_r^+, \tag{6.41}$$

$$\frac{d\mathbf{o}_r}{dt^+} = \boldsymbol{\omega}_r^+ \times \mathbf{o}_r, \tag{6.42}$$

where:

$$\bar{\bar{\mathbf{A}}}_r^{+'} = \frac{1}{2\pi \left(a^+\right)^2 \rho_p^+} \bar{\bar{\mathbf{A}}}_r^+ = \\ = \begin{cases} \frac{3}{\left(a^+\right)^2 \rho_p^+} \left[Y^A \bar{\bar{\boldsymbol{\delta}}} + \left(X^A - Y^A\right) \mathbf{o}_r \mathbf{o}_r^T\right] & if \quad Re_{p;r} \simeq 0, \\ \frac{C_{D;r} v_{\perp;r}^+}{\pi a^+ \rho_p^+} \left(\bar{\bar{\boldsymbol{\delta}}} - \mathbf{o}_r \mathbf{o}_r^T\right) & if \quad Re_{p;r} > 0, \end{cases}$$

$$\bar{\bar{\mathbf{J}}}_r^+ = \frac{4\lambda_r^2 + 3}{6} \left(\bar{\bar{\boldsymbol{\delta}}} - \mathbf{o}_r \mathbf{o}_r^T\right) + \mathbf{o}_r \mathbf{o}_r^T,$$

$$\dot{\bar{\bar{\mathbf{J}}}}_r^+ = \frac{4\lambda_r^2 - 3}{6} \left\{\left(\mathbf{o}_r \times \boldsymbol{\omega}_r^+\right) \mathbf{o}_r^T + \left[\left(\mathbf{o}_r \times \boldsymbol{\omega}_r^+\right) \mathbf{o}_r^T\right]^T\right\},$$

$$\bar{\bar{\mathbf{C}}}_r^{+'} = \frac{\lambda_r^2}{\pi\rho_p^+ \left(a^+\right)^2}\bar{\bar{\mathbf{C}}}_r^+ =$$
$$= \begin{cases} \frac{8\lambda_r^2}{\rho_p^+(a^+)^2}\left[Y^C\bar{\bar{\boldsymbol{\delta}}} - \left(X^C - Y^C\right)\mathbf{o}_r\mathbf{o}_r^T\right] & if \quad Re_{p;r} \simeq 0, \\ \frac{C_{D;r}v_{\perp;r}^+\lambda_r^2}{3\pi\rho_p^+ a^+}\left(\bar{\bar{\boldsymbol{\delta}}} - \mathbf{o}_r\mathbf{o}_r^T\right) & if \quad Re_{p;r} > 0, \end{cases}$$
$$\mathbf{H}_r^{+'} = \frac{\lambda_r^2}{\pi\rho_p^+ \left(a^+\right)^2}\mathbf{H}_r^+ = \begin{cases} \frac{-8\lambda_r^2}{\rho_p^+(a^+)^2}Y^H\left(\bar{\bar{\boldsymbol{\varepsilon}}}\mathbf{o}_r\right) : \left(\dot{\bar{\bar{\boldsymbol{\gamma}}}}_r\mathbf{o}_r\right) & if \quad Re_p \simeq 0, \\ \frac{\lambda_r^2 C_{D;r}v_{\perp;r}^+}{3\pi\rho_p^+ a^+}\left(\bar{\bar{\boldsymbol{\varepsilon}}}\mathbf{o}_r\right) : \left(\dot{\bar{\bar{\boldsymbol{\gamma}}}}_r\mathbf{o}_r\right) & if \quad Re_p > 0. \end{cases}$$

Temporal Discretization of Fiber Equations in Non-Dimensional Form

The final system of eqs.[2.69]-[6.42], in non-dimensional form is

$$\begin{aligned} &\mathbf{v}_r^{+,n+1} = \mathbf{K}_r^{+,n} + \bar{\bar{\mathbf{Q}}}_r^{+,n}\left(\mathbf{X}_{r+1}^{+,n} - \mathbf{X}_r^{+,n}\right), \\ &\boldsymbol{\omega}_r^{+,n+1} = \mathbf{R}_r^{+,n} + \bar{\bar{\mathbf{S}}}_r^{+,n}\bar{\bar{\mathbf{O}}}_r^{\,n}\left(\mathbf{X}_{r+1}^{+,n} + \mathbf{X}_r^{+,n}\right), \\ &\mathbf{o}_r^{n+1} = \mathbf{o}_r^n + \frac{1}{6}\left[\mathbf{k}_{rk1;r}^n + 2\left(\mathbf{k}_{rk2;r}^n + \mathbf{k}_{rk3;r}^n\right) + \mathbf{k}_{rk4;r}^n\right], \\ &\bar{\bar{\mathbf{M}}}_{r+1}^{\,n}\mathbf{X}_{r+2}^{+,n} + \left(\bar{\bar{\mathbf{N}}}_{r+1}^{\,n} + \bar{\bar{\mathbf{N}}}_r^{\,n}\right)\mathbf{X}_{r+1}^{+,n} + \bar{\bar{\mathbf{M}}}_r^{\,n}\mathbf{X}_r^{+,n} = \mathbf{K}_r^{tot,n}, \\ &\mathbf{p}_r^{+,n+1} = \mathbf{p}_r^{+,n} + \Delta t^+\mathbf{v}_r^{+,n+1}, \end{aligned} \tag{6.43}$$

where:

$$
\begin{aligned}
\bar{\bar{\tilde{\mathbf{O}}}}_r^{\,n} &= \begin{bmatrix} 0 & -o_{z;r}^n & o_{y;r}^n \\ o_{z;r}^n & 0 & -o_{x;r}^n, \\ -o_{y;r}^n & o_{x;r}^n & 0 \end{bmatrix} \quad \Longrightarrow \quad \mathbf{o}_r^n \times \mathbf{a} = \bar{\bar{\tilde{\mathbf{O}}}}_r^{\,n} \mathbf{a} \quad \forall \mathbf{a}, \\
\mathbf{K}_r^{+,n} &= \left(\bar{\bar{\boldsymbol{\delta}}} + \Delta t^+ \bar{\bar{\mathbf{A}}}_r^{+',n} \right)^{-1} \left(\mathbf{v}_r^{+,n} + \Delta t^+ \bar{\bar{\mathbf{A}}}_r^{+',n} \mathbf{u}_r^{+,n} \right), \\
\bar{\bar{\mathbf{Q}}}_r^{+,n} &= \frac{\Delta t^+}{2\pi\lambda_r \left(a^+\right)^3 \rho_{p;r}^+} \left(\bar{\bar{\boldsymbol{\delta}}} + \Delta t^+ \bar{\bar{\mathbf{A}}}_r^{+',n} \right)^{-1}, \\
\mathbf{R}_r^{+,n} &= \left(\Delta t^+ \dot{\bar{\bar{\mathbf{J}}}}_r^{+,n} + \bar{\bar{\mathbf{J}}}_r^{+,n} + \Delta t^+ \bar{\bar{\mathbf{C}}}_r^{+',n} \right)^{-1} \\
&\quad \left(\bar{\bar{\mathbf{J}}}_r^{+,n} \boldsymbol{\omega}_r^{+,n} + \Delta t^+ \bar{\bar{\mathbf{C}}}_r^{+',n} \boldsymbol{\Omega}_r^{+,n} + \Delta t^+ \mathbf{H}_r^{+',n} + \right. \\
&\quad \left. + \frac{\Delta t^+ E_Y^+}{8\lambda_r^2 \left(a_r^+\right)^2 \rho_{p;r}^+} \left(\alpha_{r+1}^{b,n} \mathbf{e}_r^{b,n} - \alpha_r^{b,n} \mathbf{e}_{r+1}^{b,n} \right) \right), \\
\bar{\bar{\mathbf{S}}}_r^{+,n} &= \frac{\Delta t^+}{\pi \left(a^+\right)^4 \rho_p^+} \left(\Delta t^+ \dot{\bar{\bar{\mathbf{J}}}}_r^{+,n} + \bar{\bar{\mathbf{J}}}_r^{+,n} + \Delta t^+ \bar{\bar{\mathbf{C}}}_r^{+',n} \right)^{-1}, \\
\mathbf{k}_{rk1;r}^n &= -\Delta t^+ \mathbf{o}_r^n \times \boldsymbol{\omega}_r^{n+1}, \\
\mathbf{k}_{rk2;r}^n &= -\Delta t^+ \left(\mathbf{o}_r^n + \frac{1}{2} \mathbf{k}_{rk1;r}^n \right) \times \boldsymbol{\omega}_r^{n+1}, \\
\mathbf{k}_{rk3;r}^n &= -\Delta t^+ \left(\mathbf{o}_r^n + \frac{1}{2} \mathbf{k}_{rk2;r}^n \right) \times \boldsymbol{\omega}_r^{n+1}, \\
\mathbf{k}_{rk4;r}^n &= -\Delta t^+ \left(\mathbf{o}_r^n + \mathbf{k}_{rk3;r}^n \right) \times \boldsymbol{\omega}_r^{n+1}.
\end{aligned}
$$

So the final system is:

$$
\begin{aligned}
\mathbf{K}_n^{tot} &= -\mathbf{K}_{r+1}^{+,n} + \mathbf{K}_r^{+,n} - \lambda_r a^+ \bar{\bar{\tilde{\mathbf{O}}}}_r^{\,n} \mathbf{R}_r^{+,n} - \lambda_r a^+ \bar{\bar{\tilde{\mathbf{O}}}}_{r+1}^{\,n} \mathbf{R}_{r+1}^{+,n}, \\
\bar{\bar{\mathbf{M}}}_{r+1}^n &= \bar{\bar{\mathbf{Q}}}_{r+1}^{+,n} + \lambda_r a^+ \bar{\bar{\tilde{\mathbf{O}}}}_{r+1}^{\,n} \bar{\bar{\mathbf{S}}}_{r+1}^{+,n} \bar{\bar{\tilde{\mathbf{O}}}}_{r+1}^{\,n}, \\
\bar{\bar{\mathbf{M}}}_r^n &= \bar{\bar{\mathbf{Q}}}_r^{+,n} + \lambda_r a^+ \bar{\bar{\tilde{\mathbf{O}}}}_r^{\,n} \bar{\bar{\mathbf{S}}}_r^{+,n} \bar{\bar{\tilde{\mathbf{O}}}}_r^{\,n}, \\
\bar{\bar{\mathbf{N}}}_{r+1}^n &= -\bar{\bar{\mathbf{Q}}}_{r+1}^{+,n} + \lambda_r a^+ \bar{\bar{\tilde{\mathbf{O}}}}_{r+1}^{\,n} \bar{\bar{\mathbf{S}}}_{r+1}^{+,n} \bar{\bar{\tilde{\mathbf{O}}}}_{r+1}^{\,n}, \\
\bar{\bar{\mathbf{N}}}_r^n &= -\bar{\bar{\mathbf{Q}}}_r^{+,n} + \lambda_r a^+ \bar{\bar{\tilde{\mathbf{O}}}}_r^{\,n} \bar{\bar{\mathbf{S}}}_r^{+,n} \bar{\bar{\tilde{\mathbf{O}}}}_r^{\,n}.
\end{aligned}
\tag{6.44}
$$

A

Publications, courses and projects

Referred Journals

J1 **D. Dotto** and C. Marchioli (2019) Defomation dynamics of flexible fibers in turbulence *Meccanica* (Under review, selected for special issue)

J2 **D. Dotto** and C. Marchioli (2019) Orientation, distribution and deformation of inertial flexible fibers in turbulent channel flow *Acta Mechanica* (Accepted)

Referred Conferences

C6 **D.Dotto** and C. Marchioli (2019) Orientation, distribution and deformation of inertial flexible fibers in turbulent channel flow (under review) *Internaional Conference on Multiphase Flow*, Rio, (Brazil)

C5 **D.Dotto**† and C. Marchioli (2018) Dynamics of flexible fibers in turbulent channel flow *European Fluid Mechanics Conference (EFMC12)*, Wien, (Austria)

C4 **D.Dotto**† and C. Marchioli (2018) Dynamics of flexible fibers in turbulent channel flow *Euromech Colloquium*, Venice, (Italy)

C3 **D.Dotto** and C. Marchioli† (2018) Dynamics of flexible fibers in turbulent channel flow 22^{th} *session of SHF Scientific and Technical Committee on Dispersed Two-Phase Flow Workshop*, Toulouse, (France)

C2 **D.Dotto** and C. Marchioli† (2018) Dynamics of small flexible fibers in turbulent channel flow 87^{th} *Annual GAMM Conference*, Munich, (Germany)

C1 **D.Dotto**, C. Marchioli† and Soldati A., (2017) Dynamics of small inertial flexible fibers in turbulent channel flow *APS* 70^{th} *Meeting of APS, Division of Fliud Dynamics*, Denver, (CO, USA)

† Presentation speaker.

Advanced Courses

A9 6^{th} **Advanced Cours on Liquid Interfaces, Drops and Sprays (LIDESP IV)**, TU, Wien (Austria), 2018. Coordinated by: Prof. A. Soldati, TU Wien, Wien, Prof. F. Zonta, TU Wien, Wien

A8 **IUTAM Symposium on Motile cells in complex environments**, University of Udine, Udine (Italy), 2018. Coordinated by: Prof. C. Marchioli, University of Udine, Udine, Prof. E. Climent, IMFT Toulouse, Toulouse

A7 **Fluid Dynamic Effects on Particle Formation in Crystallization Processes**, International Centre for Mechanical Sciences (CISM), Udine (Italy), 2018. Coordinated by: Prof. D. Marchisio, Politecnico di Torino, Torino, Prof. C. Marchioli, University of Udine, Udine.

A6 **Complex Flows and Complex Fluids**, International Centre for Mechanical Sciences (CISM), Udine (Italy), 2017. Coordinated by: Prof. F. Toschi, Eindhoven University of technology, Eindhoven.

A5 **Flowing Matter**, International Centre for Mechanical Sciences (CISM), Udine (Italy), 2017. Coordinated by: Prof. E. Guazzelli, Ècole Marseille Polytech, Marseille.

A4 26^{th} **Summer School on Parallel Computing**, SuperComputing Applications and Innovation (SCAI) CINECA, Rome (Italy), July, 2017. Coordinated by: G. Erbacci (CINECA, Bologna).

A3 **ICMF 2016 International Conference Multiphase Flow**, Florence (Italy), 2016 Chairman by: Prof. A. Soldati, University of Udine, Udine

A2 **Wall-Bounded Turbulence**, International Centre for Mechanical Sciences (CISM), Udine (Italy), 2016. Coordinated by: Prof. S. Pirozzoli, La Sapienza, Roma

A1 **Multiscale Modeling of Soft Matter and Polymer System**, International Centre for Mechanical Sciences (CISM), Udine (Italy), 2016. Coordinated by: Prof. D. Marchisio, Politecnico di Torino, Torino, Prof. P. Carbone, University of Manchester, Manchester

Bibliography

Andrić, J., , Lindström, S., Sasic, S., and Nilsson, H. (2014). Rheological properties of dilute suspensions of rigid and flexible fibers. *J. Non-Newton. Fluid Mech.*, 212(36).

Andrić, J., Fredriksson, S., Lindström, S., Sasic, S., and Nilsson, H. (2013). A study of a flexible fiber model and its behavior in dns of turbulent channel flow. *Ac. Me.*, 224(2359).

Ardekani, M. N., Costa, P., Breugem, W.-P., Picano, F., and Brandt, L. (2017a). Drag reduction in turbulent channel flow laden with finite-size oblate spheroids. *J. Fluid Mech.*, 816(43).

Ardekani, M. N., Sardina, G., Brandt, L., Karp-Boss, L., Bearon, R. N., and Variano, E. (2017b). Sedimentation of inertia-less prolate spheroids in homogenous isotropic turbulence with application to non-motile phytoplankton. *J. Fluid Mech.*, 831(655).

Ayala, O., Rabowsky, W., and Wang, L. (2007). A hybrid approach for simulating turbulent collisions of hydrodynamically-interacting particles. *J. Comput. Phys.*, 1(225).

Balachandar, S. and Eaton, K. (2010). Turbulent dispersed multiphase flow. *Annu. Rev. Fluid Mech.*, 42(111).

Battista, F., Gualtieri, P., Molicone, J., and Casciola, C. M. (2018). Application of the exact regularized point particle method (erpp) to particle laden turbulent shear flows in the two-way coupling regime. *Int. J. Multiphase Flow*, 35(827).

Boer, L., Buist, K., Deen, N., Padding, J., and Kuipers, J. (2018). Experimental study on orientation and de-mixing phenomena of elongated particles in gas-fluidized beds. *Powd. Tech.*, 329(332).

Brenner, H. (1964). The stokes resistance of an arbitrary particle iv. arbitrary fields of flow. *Chem. Eng. Sci.*, 19(703).

Brenner, H. and Cox, R. (1963). The resistance to a particle of arbitrary shape in translational motion at small reynolds numbers. *J. Fluid Mech.*, 17(561).

Brouzet, C., Verhille, G., and Gal, P. L. (2014). Flexible fiber in a turbulent flow: A macroscopic polymer. *Phys. Rev. Lett.*, 112(074501).

Byron, M., Einarsson, J., Gustavsson, K., Mehlig, G. V. B., and Variano, E. (2015). Flexible fiber in a turbulent flow: A macroscopic polymer. *Phys. Fluids*, 27(035101).

Challabotla, N., Zhao, L., and Andersson, H. (2015). Orientation and rotation of inertial disk particles in wall turbulence. *J. Fluid Mech.*, 766(R2).

Chong, M., Perry, A., and Cantwell, B. (1990). A general classification of three-dimensional flow fields. *Phys. Fluids A*, 2(765).

Clift, R., Grace, J., and Weber, M. (1978). Bubbles, drops and particles. *Academic Press, New York*.

Cox, R. (1971). The motion of long slender bodies in a viscous fluid. part 2. shear flow. *J. Fluid Mech.*, 45(625).

Crowe, C., Sharma, M., and Stock, D. (1977). The particle-source in cell method for gas droplet flow. *J. Fluid Eng.*, 99(325).

Delmotte, B., Climent, E., and Plourabouè, F. (2015). A general formulation of bead models applied to flexible fibers and active filaments at low reynolds number. *J. Comput. Phys.*, 286(14).

Do-Quang, M., Amberg, G., Brethouwer, G., and Johansson, A. (2014). Simulation of finite-size fibers in turbulent channel flows. *Phys. Rev. E*, 89(013006).

Dong, S., Feng, X., Salcudean, M., and Gartshore, I. (2003). Concentration of pulp fibers in 3d turbulent channel flow. *Int. J. Multiphase Flow*, 29(1).

Elgobashi, S. (2006). An updated classification map of particle-laden turbulent flows. *IUTAM Symposium on Computational Approaches to Multiphase Flow*.

Eshghinejadfard, A., Hosseini, S., and Thevenin, D. (2017). Fully-resolved prolate spheroids in turbulent channel flows: A lattice boltzmann study. *AIP Advances*, 7(095007).

Forgacs, O. and Mason, G. (1959). Particle motions in sheared suspensions: Ix. spin and deformation of threadlike particles. *J. Colloid. Science*, 14(457).

Gallily, I. and Cohen, A. (1979). On the orderly nature of the motion of non-spherical aerosol particles. ii. inertial collision between a spherical large droplet and axially symmetrical elongated particle. *J. Colloid Interface Sci.*, 68(338).

Gualtieri, P., Picano, F., Sardina, G., and Casciola, C. M. (2014). Exact regularized point particle method for multiphase flows in the two-way coupling regime. *J. Fluid Mech.*, 773(520).

Gustavsson, K., Jucha, J., Naso, A., Lévêque, E., Pumir, A., and Mehlig, B. (2017). Statistical model for the orientation of non-spherical particles settling in turbulence. *Phys. Rev. Lett.*, 119(254501).

Hich, E. and Leal, L. (1979). Rotation of small non-axisymmetric particles in a simple shear flow. *J. Fluid Mech.*, 92(591).

Horwitz, J. and Mani, A. (2016). Accurate calculation of stokes drag for point–particle tracking in two-way coupled flows. *J. Comput. Phys.*, 318(85).

Huang, W., Shin, S., and Sung, H. (2007). Simulation of flexible filaments in a uniform flow by the immersed boundary method. *J. Comput. Phys.*, 226(2206).

Ireland, P. and Desjardins, O. (2017). Improving particle drag predictions in euler-lagrange simulations with two-way coupling. *J. Comput. Phys.*, 338(405).

Jeffery, G. (1922). The motion of ellipsoidal particles immersed in a viscous fluid. *Proc. R. Soc. London, Ser. A*, 102(161).

Joung, C., Phan-Thien, N., and Fan, X. (2001). Direct simulation of flexible fibers. *J. Non-Newton. Fluid Mech.*, 99(1).

Kim, J., Moin, P., and Moser, R. (1987). Turbulence statistics in fully developed channel flow at low reynolds number. *J. Fluid Mech.*, 177(113).

Kim, S. and Karrila, S. (1991). *Microhydrodynamics: Principles and Selected Applications*. Butterworth-Heinemann, Stoneham.

Kunhappan, D., Harthong, B., Chareyre, B., Balarac, G., and Dumont, P. (2017). Numerical modelling of high aspect ratio flexible fibers in inertial flows. *Phys. Fluids*, 29(093302).

Lillo, F. D., Cencini, M., Durham, W., M. Barry, R. S., Climent, E., and Boffetta, G. (2014). Turbulent fluid acceleration generates clusters of gyrotactic microorganisms. *Phys. Rev. Lett.*, 112(044502).

Lindström, S. and Uesaka, T. (2007). Simulation of the motion of flexible fibers in viscous fluid flow. *Phys. Fluids*, 19(113307).

Lindström, S. and Uesaka, T. (2008). Particle-level simulation of forming of the fiber network in papermaking. *Int. J. Eng. Sci.*, 46(858).

Lopez, D. and Guazzelli, E. (2017). Inertial effects on fibers settling in a vortical flow. *Phys. Rev. Fluids*, 2(024306).

López, H., Hulin, J.-P., Auradou, H., and D'Angelo, M. (2015). Deformation of a flexible fiber in a viscous flow past an obstacle. *Phys. Fluids*, 27(013102).

Lovecchio, S., Marchioli, C., and Soldati, A. (2013). Time persistence of floating particle clusters in free-surface turbulence. *Phys. Rev. E*, 88(033003).

Lovecchio, S., Zonta, F., Marchioli, C., and Soldati, A. (2017). Thermal stratification hinders gyrotactic micro-organism rising in free-surface turbulence. *Phys. Fluids*, 29(053302).

Lundell, F., Soderberg, L., and Alfredsson, P. (2011). Fluid mechanics of papermaking. *Annu. Rev. Fluid Mech.*, 43(195).

Marchioli, C. (2017). Large-eddy simulation of turbulent dispersed flows: a review of modelling approaches. *Acta Mech.*, 228(741).

Marchioli, C., Fantoni, M., and Soldati, A. (2010). Orientation, distribution, and deposition of elongated, inertial fibers in turbulent channel flow. *Phys. Fluids*, 22(033301).

Marchioli, C. and Soldati, A. (2013). Rotation statistics of fibers in wall shear turbulence. *Acta Mech.*, 224(2311).

Marchioli, C., Zhao, L., and Andersson, H. (2016). Fluid mechanics of papermaking. *Phys. Fluids*, 28(013301).

Martínez, M., Vernet, A., and Pallares, J. (2017). Clustering of long flexible fibers in two-dimensional flow fields for different stokes numbers. *Int. J. Heat Mass Transf.*, 111(532).

Maxey, M. (2017). Simulation methods for particulate flows and concentrated suspensions. *Annu. Rev. Fluid Mech.*, 49(171).

Moffet, R. and Prater, K. (2009). In-situ measurements of the mixing state and optical properties of soot with implications for radiative forcing estimates. *Proc. Natl. Acad. Sci.*, 106(11872).

Pan, Y. and Banerjee, S. (2001). Numerical simulation of particle interaction with wall turbulence. *Phys. Fluids*, 10(8).

Parsa, S., Calzavarini, E., Toschi, F., and Voth, G. (2012). Rotation rate of rods in turbulent fluid flow. *Phys. Rev. Lett.*, 109(134501).

Pei, Z., Zhang, Y., and Zhou, J. (2018). A model for the particle-level simulation of multiple flexible fibers moving in a wall-bounded fluid flow. *J. Fluids Struct.*, 80(37).

Picciotto, M., Marchioli, C., and Soldati, A. (2005). Characterization of near-wall accumulation regions for inertial particles in turbulent boundary layers. *Phys. Fluids*, 17(098101).

Quennouz, N., Shelley, M., Roure, O. D., and Lindner, A. (2015). Transport and buckling dynamics of an elastic fibre in a viscous cellular flow. *J. Fluid Mech.*, 769(387).

Ravnik, J., Marchioli, C., and Soldati, A. (2018). Application limits of jefferyÕs theory for elongated particle torques in turbulence: a dns assessment. *Acta Mech.*, 229(827).

Rosén, T., Do-Quang, M., Aidun, C. K., and Lundell, F. (2015). Effect of fluid and particle inertia on the rotation of an oblate spheroidal particle suspended in linear shear flow. *Phys. Rev. E*, 91(053017).

Ross, R. and Klingenberg, D. (1997). Dynamic simulation of flexible fibers composed of linked rigid bodies. *Phys. Rev. E*, 106(2949).

Sabban, L., Cohen, A., and van Hout, R. (2017). Temporally resolved measurements of heavy, rigid fibre translation and rotation in nearly homogeneous isotropic turbulence. *J. Fluid Mech.*, 814(42).

Sabban, L. and van Hout, R. (2011). Measurements of pollen grain dispersal in still air and stationary, near homogeneous, isotropic turbulence. *J. Aero. Sci.*, 42(867).

Sasayama, T. and Inagaki, M. (2017). Simplified bead-chain model for direct fiber simulation in viscous flow. *J. Non-Newton. Fluid Mech.*, 250(52).

Schmid, C., III, L. S., and Klingenberg, D. (2000). Simulations of fiber flocculation: Effects of fiber properties and inter-fiber friction. *J. Rheol.*, 44(781).

Shams, M., Ahmadi, G., and Rahimzadeh, H. (2001). Transport and deposition of flexible fibers in turbulent duct flows. *J. Aerosol Sci.*, 32(525).

Shapiro, M. and Goldenberg, M. (1993). Deposition of glass fiber particles from turbulent air flow in a pipe. *J. Aerosol Sci.*, 24(65).

Slowicka, A., Wajnryb, E., and Ekiel-Jezewska, M. (2015). Dynamics of flexible fibers in shear flow. *J. Chem. Phys.*, 143(124904).

Soldati, A. and Marchioli, C. (2009). Physics and modelling of turbulent particle deposition and entrainment: Review of a systematic study. *Int. J. Multiphase Flow*, 35(827).

Stockie, J. and Green, S. (1998). Simulating the motion of flexible pulp fibres using the immersed boundary method. *J. Comput. Phys.*, 147(398).

Subramanian, G. and Koch, D. (2005). Inertial effects on fibre motion in simple shear flow. *J. Fluid Mech.*, 535(383).

SwitzerIII, L. and Klingenberg, D. (2003). Rheology of sheared flexible fiber suspensions via fiber-level simulations. *J. Rheol.*, 47(759).

Tang, Y., Wu, T.-H., He, G.-W., and Qi, D. (2018). Multi-flexible fiber flows: A direct-forcing immersed boundary lattice-boltzamnn lattice-spring approach. *Int. J. Multiphase Flow*, 99(408).

Toschi, F. and Bodenschatz, E. (2009). Lagrangian properties of particles in turbulence. *Annu. Rev. Fluid Mech.*, 41(375).

Vakil, A. and Green, S. (2011). Flexible fiber motion in the flow field of a cylinder. *Int. J. Multiphase Flow*, 37(173).

Verhille, G. and Bartoli, A. (2016). 3d conformation of a flexible fiber in a turbulent flow. *Exp. Fluids*, 57(117).

Voth, G. and Soldati, A. (2017). Anisotropic particles in turbulence. *Annu. Rev. Fluid Mech.*, 49(249).

Wang, G., Yu, W., and Zhou, C. (2006). Optimization of the rod chain model to simulate the motions of a long flexible fiber in simple shear flows. *Eur. J. Mech. B Fluids*, 44(337).

Wu, J. and Aidun, C. (2010). A method for direct simulation of flexible fiber suspensions using lattice boltzmann equation with external boundary force. *Int. J. Multiphase Flow*, 36(202).

Xiang, P. and Kuznetsov, A. (2008). Simulation of shape dynamics of a long flexible fiber in a turbulent flow in the hydro-entanglement process. *Int. Commun. Heat Mass Transf.*, 35(529).

Yamamoto, S. and Matsuoka, T. (1993). A method for dynamic simulation of rigid and flexible fibers in a flow field. *J. Chem. Phys.*, 98(644).

Yuan, W., Andersson, H., Zhao, L., Challabotla, N., and Deng, J. (2017). Dynamics of disk-like particles in turbulent vertical channel flow. *Int. J. Multiphase Flow*, 96(86).

Zhan, C., Sardina, G., Lushi, E., and Brandt, L. (2014). Accumulation of motile elongated micro-organisms in turbulence. *J. Fluid Mech.*, 739(22).

Zhang, D. and Smith, D. (2016). Dynamic simulation of discrete fiber motion in fiber-reinforced composite materials processing. *J. Compos. Mater.*, 50(1301).

Zhao, F., George, W., and Wachem, B. V. (2013). Direct numerical simulation of ellipsoidal particles in turbulent channel flow. *Acta Mech.*, 224(2331).

Zhao, F. and Wachem, B. V. (2015). Four-way coupled simulations of small particles in turbulent channel flow: The effects of particle shape and stokes number. *Phys. Fluids*, 27(083301).

Zhao, L., Gustavsson, K., Ni, R., Kramel, S., Voth, G., Andersson, H., and Mehlig, B. (2017). Orientation patterns of non-spherical particles in turbulence. *arXiv.org physics*.

Zhu, L. and Peskin, C. (2007). Drag of a flexible fiber in a 2d moving viscous fluid. *Computers & Fluids*, 36(398).